

**SOLAR WIND INTERACTIONS WITH A  
PLANETARY OFF-CENTER  
MINI-MAGNETOSPHERE: A CASE STUDY FOR  
MARS**

*A thesis submitted in partial fulfilment of the requirements for the award  
of the degree of*

**MASTER OF SCIENCE**

*by*

**SAJAL GUPTA  
15MS084**

*under the supervision of  
Dr. Dibyendu Nandi*

*to the*

**Department of Physical Sciences  
of**

**Indian Institute of Science Education and Research Kolkata**

**Center of Excellence in Space Sciences India**



**August 27, 2022**



“See what you’re doing wrong, laugh at it, change and do better.”

—Spencer Johnson, Who Moved My Cheese?

I would like to dedicate this thesis to my loving family, trustworthy friends, my absent enemies, astrophysics community, especially the scientific community of Mars, and to whoever takes a risk to read it.



## DECLARATION

---

I, Sajal Gupta, do hereby declare that this thesis is my own work and to the best of my knowledge, it contains no materials previously published or written by any other person, or substantial proportions of material which have been accepted for the award of any other degree or diploma at IISER Kolkata or any other educational institution, except where due acknowledgement is made in the thesis. I certify that all copyrighted material incorporated into the thesis is in compliance with the Indian Copyright (Amendment) Act, 2012. I also confirm that I have acknowledged all main sources of help. Where the thesis is based on work done by myself jointly with others, I have made clear exactly what was done by others and what I have contributed myself.

This work was done under the direction of Dr. Dibyendu Nandi, at the Indian Institute of Science Education and Research Kolkata (IISER Kolkata).

August 27, 2022  
CESSI  
IISER Kolkata



---

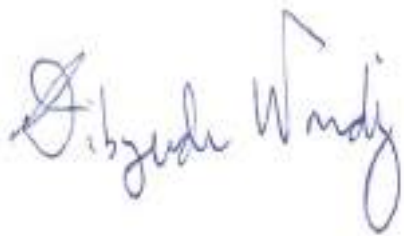
Sajal Gupta



## CERTIFICATE FROM THE SUPERVISOR

---

This is to certify that this thesis titled "**Solar wind interactions with a planetary off-center mini-magnetosphere: A case study for Mars**" - which is being submitted by Sajal Gupta (who is registered as **15MS084** at the Indian Institute of Science Education and Research Kolkata)- is based upon his own research work under my supervision and neither this thesis nor any part of it has been submitted for any degree or any other academic award anywhere else.

A handwritten signature in blue ink, appearing to read "Dibyendu Nandi".

---

Dr. Dibyendu Nandi  
Professor  
Department of Physical Sciences  
Center of Excellence in Space Sciences India (CESSI)  
Indian Institute of Science Education and Research Kolkata  
Mohanpur 741246  
India



## ACKNOWLEDGMENTS

---

First, and above all, I thank my parents and my family. During this stressful, chaotic time, this work could not have been written without their unconditional love and permanent support.

I am deeply grateful to my supervisor and mentor, Dr. Dibyendu Nandi; for entrusting me with a research agenda and offering an opportunity to work on star-planet interactions; for his constant support and much freedom in this work; for showing me not only how to do proper, quality science, but also how to be a good scientist.

I also like to express my sincere appreciation to Somu da and Dr. Arnab Basak. Their constant suggestions on how to approach challenging problems are mesmerizing. Thanks a bunch to Rana, Souvik Da, and Arghya Da, who pointed out my mistakes shamelessly and asked open-ended questions that generated interactive brainstorming sessions. A big shout-out to my treasured CESSI family who made the workplace cool, happy, and positive by gossiping about the random events to organizing last-minute parties. A special thank you note to Gopi for dealing with all my tantrums and mood swings and for being with me during this disturbing "corona-virus" time.

It goes without saying that my IISER life is incomplete without my Gawaar family. Nunnu, Sumo, Rana, Chigga, Bawa, Dheel, T- Boy, Naman, Rahul, Chandu, and Bracket, you guys are my lifesaver. I am going to miss every moment that we have spent and will cherish the times that we have passed in supporting, mocking, laughing, crying, dancing, jamming, gaming, basically everything from late-night philosophical talks to "sober" morning talks. The 1<sup>st</sup> floor of C-Wing, NSCB hostel, will always hold a special place in my heart. A big thank you to Dipankar Da, whose name is attached to a feeling called "Chai." The 7 (Saat) no. chai is an emotion that I cannot express in words.

I want to thank my long life friends, Ishaan, Abhishek, Shreya, Bhavya, and Dikshant, for relentlessly checking up on me. Cheers to the community of Stack overflow who helped countless hard-working students like me. Finally, I want to thank the developers of the PLUTO Code, the Indian Government for DST INSPIRE Fellowship, and André Miede for providing his template *classicthesis* for L<sup>A</sup>T<sub>E</sub>X which was used to typeset this thesis.

## ABSTRACT

---

The presence of an archaic, strong, dynamo-generated global magnetic field of Earth is considered one of the fundamental reasons for its habitability. However, several studies have recently cast severe doubts on it. There is a resurgence of interest in the role of planetary magnetic field on planetary habitability. The specific question(s) that drives this study are: Do habitable worlds require a magnetic field? Or, keeping all other habitable requirements equal, would a planet without intrinsic magnetic field lose more of its atmosphere rendering it inhabitable? Mars lacks a global intrinsic magnetic field, but it has the small-scale, localized regions of strong magnetic field distributed inhomogeneously in its crust. Dominance of crustal magnetic field in the southern hemisphere of Mars makes it a great natural laboratory to understand the effects of the planetary magnetic fields in star-planet interactions.

We carry out 3D compressible magnetohydrodynamic ([MHD](#)) simulations for a hypothetical Sun-Mars system with a Star-Planet Interaction Module (SPIM) created at CESSI, based on the PLUTO code. An off-centered, weak dipolar magnetic field is incorporated in the southern part of the planet to mimic the effects of the crustal field. We simulate three different cases: a) planet with no dipolar field, b) planet with the mini-magnetosphere in which the Interplanetary Magnetic Field ([IMF](#)) is oriented southward ([S-IMF](#)) and c) northward ([N-IMF](#)), relative to the direction of the planetary dipole axis. We discover a hybrid magnetic topology in the simulations when the planetary magnetic field is switched on. We also identify that magnetic reconnections lead to decreased magnetic strength and, eventually, a weak current density in the wake of the planet. Interestingly, we find that signatures of reconnection mediated changes in magnetic field extend down to the planetary surface, which can be detected by magnetometers in Martian rovers. We analyze the flow of current density and find that the mini-magnetosphere can decelerate the solar wind and channel the flow from the southern to the northern hemisphere in the early part of the Martian magneotail.

The subsolar and terminator position of the Bow Shock ([BS](#)) in the presence or absence of mini-magnetosphere is estimated to be ( $1.52 R_M$ ,  $3.8 R_M$ ). Although we notice some dissimilarities in the BS structure of above two cases, the variation was quite small. In particular, we do not observe the Magnetic Pileup Boundary ([MPB](#)) in the simulations due to the thin atmosphere. However, a region is observed starting from a subsolar distance of  $1.075 R_M$  having signatures similar to the [MPB](#). The simulations show that the mini-magnetosphere produces a localized magnetopause-like structure (i.e., mini-magnetopause) in the southern hemisphere, about a distance of  $1.09 - 1.1 R_M$  from the center of the planet. In addition, we witness the phenomenon of magnetopause erosion during periods

of Southward-Interplanetary Magnetic Field ([S-IMF](#)).

During interactions of the mini-magnetosphere with [S-IMF](#) we estimate a 0.5% higher local mass-loss rate from the Northern Hemisphere compared to the Southern Hemisphere. This happens due to the mini-magnetosphere, which deflects the solar wind ions and traps the planetary particles in the closed field lines loops. To illuminate the effects of Interplanetary Magnetic Field ([IMF](#)) we compare the local mass-loss rates for [N-IMF](#) and [S-IMF](#). We observe that magnetic reconnections lead to a higher mass-loss rate in the [S-IMF](#) case by providing escape energy and momentum to ionospheric particles. The moment of truth arises when we compare the total local mass-loss rates of No dipole ([ND](#)) case with the [S-IMF](#) and [N-IMF](#) cases. The mass-loss rates in the absence of the crustal field is estimated to be 2% and 3% higher than the [S-IMF](#) and [N-IMF](#) cases. This clearly indicates that mini-magnetospheres prevent atmospheric mass-losses from a planet.



## CONTENTS

---

<b>I</b>	<b>ROLE OF MAGNETIC FIELD IN STAR-PLANET INTERACTIONS</b>	<b>1</b>
<b>1</b>	<b>MAGNETIC FIELD: BOON OR BANE</b>	<b>3</b>
1.1	Magnetic field as a savior	3
1.2	Star-Planet Interactions	4
1.2.1	The Solar Wind	5
1.2.2	Intrinsic Magnetosphere	6
1.2.3	Induced Magnetosphere	8
1.3	Do we require Magnetic Field?	9
<b>II</b>	<b>THE SHOWCASE: MARS AND THE NUMERICAL MODEL</b>	<b>13</b>
<b>2</b>	<b>MARS</b>	<b>15</b>
2.1	General Characteristics	15
2.2	Crustal Magnetic Field	16
2.3	Impact of Crustal field: A "New" picture of Mars-Sun system	18
<b>3</b>	<b>NUMERICAL MODEL</b>	<b>21</b>
3.1	MHD Equations	21
3.2	Grid Configuration	22
3.3	Input Parameters	23
3.4	Planet's thin atmosphere	23
3.5	Mini-magnetosphere	24
3.6	Our Numerical Scheme: Star-Planet Interaction Module	26
3.6.1	Problem Setup and Initialization	26
3.6.2	Boundary Conditions	28
3.6.3	Initialization of Tracers and Shock Front	29
3.7	An outline of the interaction	30
<b>III</b>	<b>RESULTS</b>	<b>33</b>
<b>4</b>	<b>MAGNETIC RECONNECTION AND ITS CONSEQUENCES</b>	<b>35</b>
4.1	Physics of magnetic reconnection	35
4.2	Magnetic Reconnection in the Martian System	36
4.3	3D Magnetic Geometry	37
4.4	Simulation Results: Magnetic field deviation and Current Sheet	38
4.5	Polar Analysis	41
<b>5</b>	<b>PLASMA BOUNDARIES</b>	<b>43</b>
5.1	Underlying physics of Bow Shock	43
5.2	Simulation results: Bow Shock	45
5.3	Does intrinsic magnetic field affect Bow Shock?	46
5.4	Magnetic Pile-up Region	49
5.5	Mini-Magnetopause	51
<b>6</b>	<b>ATMOSPHERIC EROSION</b>	<b>55</b>
6.1	Escape Processes	55

6.2 Consequences of location of mini-magnetosphere	57
6.3 Effects of Interplanetary magnetic field direction	60
6.4 Impacts of mini-magnetosphere	61
<b>7 CONCLUSION</b>	<b>63</b>
<b>A DENSITY AND PRESSURE OF ATMOSPHERE</b>	<b>67</b>
<b>B MAGNETIC DIPOLE FIELD EQUATIONS</b>	<b>69</b>
<b>C RANKINE-HUGONIOT JUMP CONDITIONS</b>	<b>73</b>
<b>D CONSEQUENCES OF THIN ATMOSPHERE</b>	<b>77</b>
<b>E REMAINING RESULTS OF NIMF STUDY</b>	<b>79</b>
<b>BIBLIOGRAPHY</b>	<b>81</b>

## LIST OF FIGURES

---

Figure 1	A sketch of magnetic field lines projected onto the equatorial plane of solar wind.	5
Figure 2	A schematic illustration of Earth-Sun system in noon-midnight plane depicting various magnetospheric structures formed during interaction.	7
Figure 3	A sketch of Solar wind interaction with Martian induced magnetosphere.	8
Figure 4	A schematic illustration of ion outflow from planet Earth.	10
Figure 5	A cartoon sketch of bulk removal process near the strong magnetic site in the Martian atmosphere.	10
Figure 6	A pseudocolor map displaying out the geographical spread of crustal magnetic field.	17
Figure 7	A cartoon sketch of martian hybrid magnetosphere.	18
Figure 8	Atmospheric profile of Planet	24
Figure 9	A schematic illustration of modeled mini-magnetosphere	25
Figure 10	A schematic illustration of magnetic reconnection in two-dimensional geometry.	36
Figure 11	A cartoon sketch of 2D magnetic reconnection in Martian system	36
Figure 12	Three-Dimensional modeling of the magnetic streamlines	37
Figure 13	Pseudocolor plots of magnetic field deviation and current density in noon-midnight plane for S-IMF and ND cases.	39
Figure 14	Polar analysis of magnetic field deviation components at different elevation in noon-midnight plane.	41
Figure 15	A qualitative sketch of pressure gradient leading to the formation of BS	44
Figure 16	A contour line plot of BS structure for ND case	45
Figure 17	A contour line plot of BS structure for S-IMF and ND cases respectively.	47
Figure 18	a) A qualitative sketch of $\Delta r$ at point $z_0$ b) A graphical representation of variation of estimated $\Delta r/R_M$ with Z plane.	48
Figure 19	Signatures of Magnetic Pile-up Region	50
Figure 20	A pseudocolor plot of total magnetic strength in noon-midnight plane for a)S-IMF and b)N-IMF case.	52
Figure 21	Structure of mini-magnetopause for both S-IMF (red) and N-IMF (blue) studies in wind-IMF plane.	53
Figure 22	A cartoon sketch of different escape mechanisms operating on Martian atmosphere.	56

Figure 23	a) Local atmospheric mass loss rate from southern hemisphere (SH) and northern hemisphere (NH) in a)x- axis b) y- axis (left) and z- axis (right)	58
Figure 24	Temporal evolution of localized atmospheric mass loss rate from three different box size	60
Figure 25	Local atmospheric mass loss rate from a) Southern hemisphere (SH) and b) Northern hemisphere (NH) for <b>S-IMF</b> and <b>N-IMF</b> cases	61
Figure 26	Temporal evolution of total localized atmospheric mass loss rate from all three cases.( <b>S-IMF</b> , <b>N-IMF</b> and <b>ND</b> )	62
Figure 27	A qualitative sketch of magnetic dipole placed at origin.	70
Figure 28	Pressure plot normalized to ambient pressure in noon-midnight plane.	78
Figure 29	A pseudocolor plot of x-component of current density in a) equatorial plane and b) dawn dusk plane.	78
Figure 30	A pseudocolor plot of a) $(B_y/B_{sw}) - 1$ and (b) $B_z/B_{sw} - 1$ in dawn-dusk plane	78
Figure 31	Pseudocolor plots of magnetic field deviation for <b>N-IMF</b> study in noon-midnight plane	79
Figure 32	Pseudocolor plots of current density for <b>N-IMF</b> study in noon-midnight plane	79
Figure 33	A contour line plot of <b>BS</b> structure for <b>S-IMF</b> and <b>N-IMF</b> cases respectively.	80
Figure 34	A graphical representation of variation of estimated $\Delta r/R_M$ with Z plane	80

## LIST OF TABLES

---

Table 1	Bulk and atmospheric properties of present day Mars and for reference, Earth.	15
Table 2	The Grid Extent and Resolution	22
Table 3	List of physical parameters and their respective notations	23
Table 4	PLUTO definition file for our reference simulation	26
Table 5	Values used for Shock Front	30

## ACRONYMS

---

SPI Star-Planet Interactions

IMF	Interplanetary Magnetic Field
BS	Bow Shock
IMB	Induced Magnetosphere Boundary
MPB	Magnetic Pileup Boundary
NASA	National Aeronautics and Space Administration
MGS	Mars Global Surveyor
MAG/ER	Magnetometer and Electron Reflectometer
MAVEN	Mars Atmosphere and Volatile Evolution
MHD	Magnetohydrodynamics
ASPERA-3	Analyzer of Space Plasma and Energetic Atoms
SPIM	Star-Planet Interaction Module
STS	Super-Time-Stepping
S-IMF	Southward-Interplanetary Magnetic Field
N-IMF	Northward-Interplanetary Magnetic Field
ND	No dipole
ICB	Ion composition boundary
SWIA	Solar Wind Ion Analyzer
MPR	Magnetic Pile-up Region
MSO	Mars-centered Solar Orbital



## Part I

### ROLE OF MAGNETIC FIELD IN STAR-PLANET INTERACTIONS

We started off by describing how vital is the planetary magnetic field for the habitability of a planet. Then, we expand our horizon and introduce some new observations that suggest that the magnetic field might not be as essential requirement as we thought. Subsequently, we demonstrated the physics of star-planet interactions and briefly explained the cases when the magnetosphere is present or absent in the system. The previous topic was put forward to understand the underlying physics of the planetary magnetic field. At last, we delivered some physical explanations of how the magnetic field can ruin our conventional idea and closed with a little teaser about the unique properties of planet Mars.



## MAGNETIC FIELD: BOON OR BANE

---

Invisible to our naked eye, ubiquitous in its nature and existing all the time to protect our atmosphere from harmful space radiations- is the Earth's magnetic field. For most of us, it hardly catches our attention, but in reality, we all owe our existence to it. Our home planet Earth, third in its position to the Sun, is the only habitable planet in our solar system. As a matter of fact, it is currently the only planet known to be teeming with life of various forms. According to the sources <sup>1</sup>, there are almost 4000+ confirmed exoplanets, in which only a few of them has considered to be potentially habitable. However, still, no conclusive remarks have been made, which might make one wonder about what are the factors that make our Earth special?

### 1.1 MAGNETIC FIELD AS A SAVIOR

A planet's ability (or a natural satellite like our Moon) to sustain life is a result of several factors. It is believed to be a function of bulk parameters of planet, its orbital distance from its star (or the Sun for our solar system), its rotation rate and atmospheric composition, presence of magnetic field, stellar factors like stellar variability, spectral class of a star, its position with respect to the Habitable zone and, much more [Meadows and Barnes (2018); Guedel et al. (2014); Huang (1960)]. Investigating the effects of each factor is quite complicated, but one can qualitatively determine the extent to which these factors affect a planet's habitability. For example, in the solar system, leaving Pluto, the four gas giant planets named Jupiter, Saturn, Uranus, and Neptune lie too far from the Habitable zone. Their large distance from the Sun makes them unable to have proper physical conditions required to possess and maintain water for organic life. Whereas Mercury, being the closest planet to the Sun, has its atmosphere almost stripped away due to extreme solar activity. Thus, we boiled down to three remaining planets, which not only lie in the proximity of the Habitable zone [Vogel (1999)] but also holds a terrestrial atmosphere. Venus, Earth, and Mars all the three rocky planets have the potential to lead life at some point of their age, but we know that only Earth came out as a livable planet. It is because of the presence of a strong magnetic field in its interior, which the other two planets are devoid of. Though Mars has small chunks of concentrated magnetic anomalies, but it is still minuscule in comparison to geomagnetic strength [Brain (2006)]. The constantly moving molten metal in the Earth's interior generates electric currents, which in turn produces magnetic field due to dynamo effect [Parker (1955); Busse (1978)]. This large magnetic field is global, meaning it surrounds the entire planet and shields it from harmful electromagnetic radiation. This distinctive trait of Earth

---

<sup>1</sup> NASA Exoplanet Archive

led scientists to believe that the magnetic field is essential and must meet the criteria for a planet's habitability.

However, recently a new debate has ensued regarding the true nature of the magnetic field. [Strangeway et al. \(2017\)](#) reported that the global escape rate of oxygen ion at Earth ( $\sim 10^{25-26}$  ions/s) is almost one order higher than at Venus and Mars ( $\sim 10^{24}$  ions/s). The oxygen, being an important constituent of water and life, expresses the potential of the planet's habitability. Though a global atmospheric escape is a result of several mechanisms (divided into thermal and non-thermal processes [[Gronoff et al. \(2020\)](#)]), the similar order ( $10^{24}$ - $10^{26}$  ions/s) of total atmospheric ion loss from present-day Venus, Mars and Earth is credited to the ineffectiveness of Earth's magnetosphere [[Strangeway et al. \(2010\)](#); [Barabash \(2010\)](#)]. This has brought the magnetic umbrella hypothesis into question [[Egan et al. \(2019\)](#)]. It drives to the speculation that the magnetic field might not be an essential requirement for long-term habitability, and in turn, favors the atmospheric erosion from the planet.

The claim, as mentioned earlier, is also important from the perspective of exoplanetary science. As we began to discover an abundance of exoplanets, it is important to understand how the magnetic field shapes the atmospheric evolution. Our quest to discover more Earth-like planets and their potential habitability highly depend on their magnetization. It might be possible that an exoplanet has all the traits required for habitability, but the presence of an intrinsic magnetic field countermands the desired picture. Or, planets having different links of magnetic field origin, might have disparate atmospheric evolution [[Lazio et al. \(2018\)](#)]. For instance, by studying the effects of planetary magnetization, we will be able to understand why some planets like Mars evolved in a completely diametric way than the planets like Earth. Thus, the question of the magnetic field's true nature is crucial and is also the focus of the present study. To achieve our goal, we shall begin our study by qualitatively understanding how a planet interacts with its host star.

## 1.2 STAR-PLANET INTERACTIONS

Generally, we can classify stellar wind interaction with planetary body in three broad categories:

1. Wind's interacting with a magnetized body (like Earth, Jupiter, and Saturn for our solar system)
2. A non-magnetized body with an insignificant atmosphere (like our natural satellite, Moon) interacting with its host star
3. A weakly/non- magnetized planet but with a considerable atmosphere (like Mars or, Venus interaction with the Sun)

All the above cases (and one more, [[Lue \(2015\)](#)]) signifies that Star-Planet Interactions ([SPI](#)) which is highly dependent on planetary characteristics. The over-

all scenario remains similar, but there are significant differences that can reveal some diametric observations. To physically understand the involved processes, join me on a voyage to our Solar system. We shall begin our journey by positioning ourselves near to the Sun.

### 1.2.1 The Solar Wind

Our closest star, Sun, is an extremely violent place where nuclear fusions are happening continuously. It is a natural particle accelerator, constantly blowing away electrically charged electrons and protons in all directions with an average speed of a few hundred kilometers per second <sup>2</sup>. Made up of hydrogen and helium ions with a sprinkling of heavier elements, this particle radiations is historically defined as "Solar Wind" by Eugene Parker in 1957 [Russell (1974); Obridko and Vaisberg (2017)]. The solar wind is a result of outspreading of plasma from the Sun's corona (outer atmosphere), where the gravitational energy is overpowered by thermal energy [Choudhuri (1998, Ch. 6); Meyer-Vernet (1999)]. Interestingly, this outward-streaming gas extracts the magnetic lines of force originating from the Sun due to the radial extension of solar magnetic field lines and the highly ionized state of plasma [Parker (1958)]. The topology of the wind's magnetic field finds its roots in the detailed calculation of [Parker (1958)] paper, where the author sketched the field lines in the form of spiral popularly known as "Parker spirals."

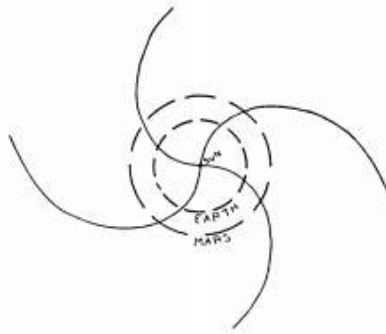


**Figure 1:** A sketch of magnetic field lines projected onto the equatorial plane of solar wind. This image is taken from Parker (1958)

These magnetic field lines, as shown in Figure 1 has one end connected to the Sun and the other end; being subjected to the plasma motion interacts with the atmosphere and magnetosphere of planetary bodies. This magnetic field coming from the Sun's plasma is commonly known as *IMF*. The supersonic wind traveling in space treats the planet as an obstacle. It continues on its unstoppable journey until it gets hit by a boundary, known as *BS*. A three-dimensional shock front forms as marked in Figure 2 and Figure 3 due to compression and accumulation of plasma. Properties of magnetized gas get modified, and we found denser, hotter, and slower-moving plasma accompanied with a higher magnetic

---

<sup>2</sup> The Solar Wind- NASA/Marshall Solar Physics

strength[Petrinec and Russell (1997)]. Owing to the presence of a planet's atmosphere or magnetosphere, **BS** defines our primary shield against the supersonic wind. Since astronomical objects like Comets, or to some extent, Moon does not have a substantial atmosphere, they could not utilize the **BS** protection and hence, interact directly with the vicious wind [Lue (2015)]. The underlying physics and properties behind BS formation are explained in Chapter 5. For the sake of completeness, we will describe its formation in straightforward terms. From our basic physics, we know that when any information travels faster than the local sound speed, the system's entropy increases, which results in an irreversible process. This decreases the time scale for balancing pressure gradient and hence, adiabatic compression occurs [*Introduction to Space Physics* (1995, Ch. 5)]. A boundary forms where the thermodynamic properties of the system like entropy, density, etc. changed, accompanied by a decrease in particle's momentum. This discontinuity is known as shock front, and the wave carrying this disturbance is called a shock wave. **BS** is very much similar, with the only difference is that it has a bow-like shape. The nonlinear bow wave deflects the plasma around the obstacle [Russell (2000 A)], which continues its expedition in post-shock regime with a subsonic velocity. Now, as we are close to a planet, the dynamics are going to depend on the presence/absence of the magnetosphere majorly. Here, we will divide our journey into two parts: one, where we will travel to Earth and others, where our red planet Mars is waiting for our arrival.

### 1.2.2 *Intrinsic Magnetosphere*

Initially coined by T. Gold in 1959 in the paper [Gold (1959)], the term "magnetosphere" refers to a region around a planet where the planetary or plasma induced magnetic field governs most of the plasma dynamics. A planet, like Earth, which has an intrinsic magnetic field interacts with the magnetized plasma, as expressed in Figure 2.

Let us start with something we already know. In the above figure, **BS** is shown as a blue color plane, where **IMF** (sketched as white arrows at an oblique angle) begins draping around the planet. In the upstream front region, wind particles (not shown) are almost perpendicular to the shock plane until they encounter the **BS**. After passing through the shock plane, the wind's plasma starts getting deflected, which results in the draping of **IMF**. The draping occurs because a planet's ionosphere is a highly conductive medium and, therefore, momentum conservation provokes **IMF**, which is frozen in wind's plasma to wrap around the planet [*Introduction to Space Physics* (1995, Ch. 6)]. As a result of flux-freezing theorem (initially coined by H. Alfvén in the paper [ALFVÉN (1942)]) **IMF** get stretches outwards in the downstream of planet. These draped field lines, being oblique to the intrinsic magnetic field, reconnects and forms open field lines. This phenomenon is called magnetic reconnection, and it serves a great purpose in plasma astrophysics. The open field lines have one end connected to the planet and the other end to the wind. One can easily find this magnetic topology in Figure 2, where the undisturbed planet's magnetic field lines (closed loops) are

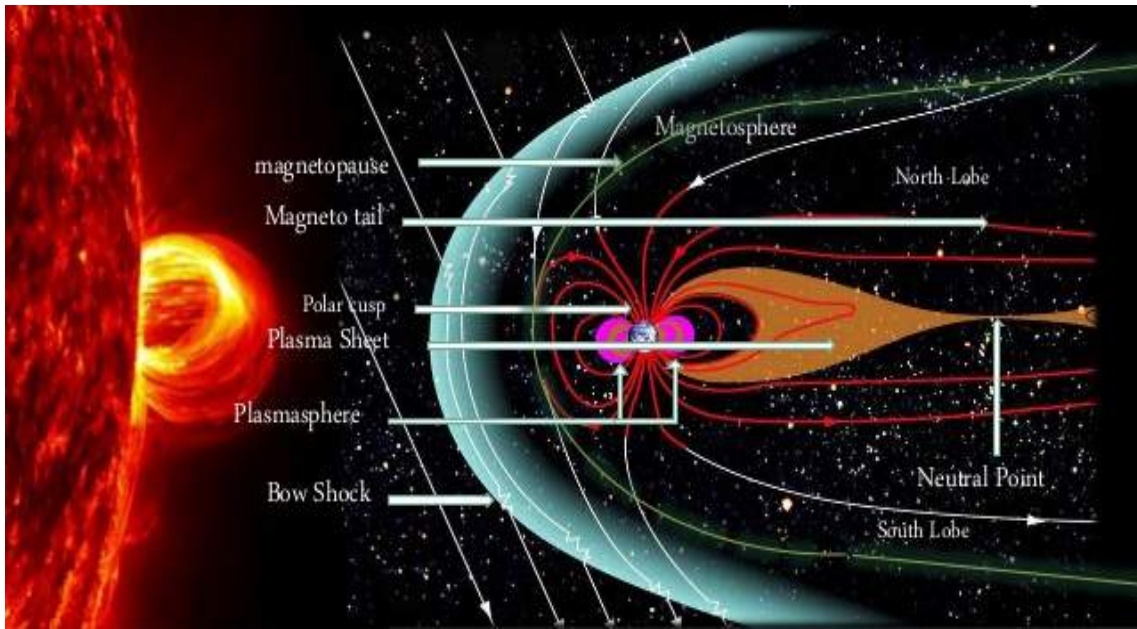


**Figure 2:** A schematic illustration of Earth-Sun system in noon-midnight plane depicting various magnetospheric structures formed during interaction. Source: National Aeronautics and Space Administration ([NASA](#))

coded in red color.

A brief description of remaining magnetospheric structures are:

1. **Magnetopause:** An outer green color boundary, which is tracing the magnetosphere in the above figure, is known as Magnetopause. This distinctive boundary determines the scale size of the magnetosphere and forms due to the balance of solar wind's dynamic pressure and the planet's magnetic pressure [[Russell \(2000 A\)](#)]. The magnetopause of a magnetized planet acts as a Faraday cage, which palliates the stripping of planetary ions, by trapping and diverting the flow of solar wind to polar cusps.
2. **Magnetosphere:** As described above, it can be easily identified as an enclosed area by the green color line. The reason for the above specific geometry can be found in [[Russell \(2000 A\)](#)]. The region between the BS and magnetosphere, is called Magnetosheath.
3. **Magnetotail:** It defines as a region of open field lines, or "lobes" in the night-side of Earth. The two lobes, called the North lobe and south lobe form because one l connects the magnetic field going into the planet, and the other is containing a magnetic field downstream away from the planet.
4. **Plasma Sheet:** Separating the "two-lobes" region of oppositely directed field lines is a sheet of the current directed-cross tail. This area of interaction is called the plasma sheet, a region of increased planetary ions and a lower magnetic field. For the Earth-like planet, both ends of these magnetic field lines are attached to the planet, and, therefore, a  $J \times B$  force

acts on the trapped ions towards the planet. Another region called "neutral sheet" forms at the center of the magnetotail, where magnetic strength approximately reaches to null [Russell (2000 A)].

5. **Neutral point:** A "X" point or a reconnection point is a specific location where magnetic reconnection happens. In 3D geometry, it takes the form of a plane. It is found in both day-side and night-side of Earth. [Russell (2000 A)]
6. **Polar Cusps:** The two arbitrary regions in the north and south of the magnetic equator, where magnetosheath plasma has direct access to Earth's ionosphere, are called polar cusps [Russell (2000 B)]. Their location highly depends on the magnetic equator and IMF topology. Because of the precipitation of charged ions in polar cusps, we observe a natural dance of lights, commonly known as "aurora."

The remaining pink color part in the neighborhood of Earth is called Van Allen Radiation Belts. It is a region where undisturbed Earth's magnetic field captures solar wind particles. A form of "ring current" set up due to the drifting motion of charged particles, which results in the kinetic energy of electrons in the range of a few MeVs [Russell (2000 A)].

### 1.2.3 Induced Magnetosphere

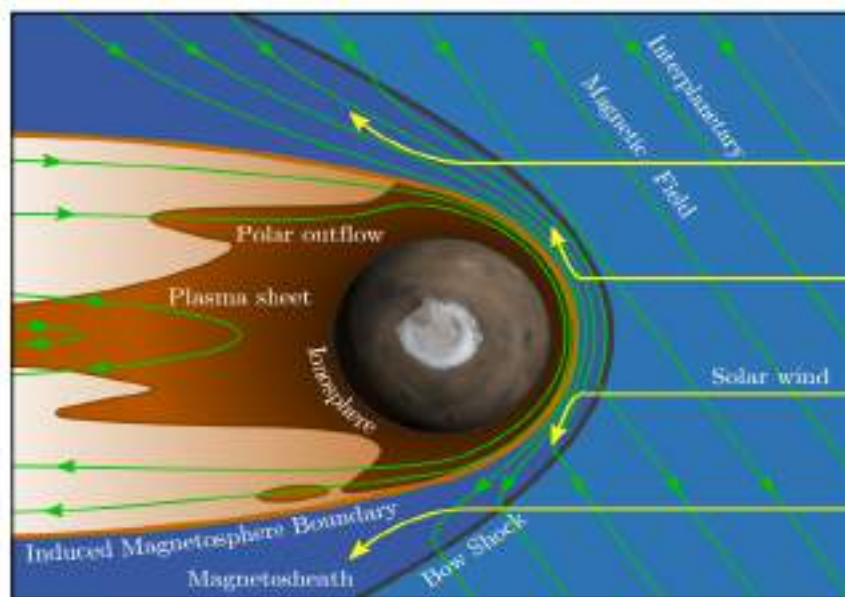


**Figure 3:** A sketch of Solar wind interaction with Martian induced magnetosphere. This image was taken from [Robin Ramstad's Doctoral Thesis](#)

As introduced above, planets like Mars and Venus do not have any significant magnetic field. However these non-magnetized planets still holds an atmosphere where ionosphere and exosphere of Mars extends up to few orders of

$R_M$  (Martian radius) [Halekas et al. (2015)]. The outcome of this atmosphere is the draping of IMF because the ionosphere of the planet is a highly conductive medium. The wind's magnetic field wraps around the planet, which results in an evolution of a magnetic shield that behaves as an intrinsic magnetosphere. This "pseudo-magnetic barrier" is commonly called as induced magnetosphere (Figure 3)). We only observe draped filed lines in this type of interaction because there is no possibility of magnetic reconnection. In the presence of said topology, planetary ions can make their way to the magnetized solar wind, where they can possibly interact through the production of electric currents. Unlike magnetopause, Induced Magnetosphere Boundary (IMB) forms due to the accumulation of IMF. IMB, or in other words, MPB though located closer to the Mars than the magnetopause is to Earth; it still inhibits the atmospheric escape.

Section 1.2.2 and Section 1.2.3 outlines the general characteristics of a stellar wind interaction with a magnetosphere/atmosphere of a planet. The major differences arise because of the presence/absence of an intrinsic magnetic field. Now, these dissimilarities will assist us in deciphering the part of the magnetic field in our survival.

### 1.3 DO WE REQUIRE MAGNETIC FIELD?

In the context of atmospheric erosion, intrinsic magnetosphere possesses some drawbacks as compared to an induced magnetosphere:

1. As discussed above, the presence of a planetary magnetic field fosters the reconnection process, which leads to the creation of open field lines. They create a channel for stellar wind particles to access the planetary atmosphere, which otherwise is isolated by intrinsic magnetic fields [Brain et al. (2007)]. In consequence, at high latitude and polar regions, topside ionospheric plasma is energized and leaves the atmosphere by trailing over the open field lines (Figure 4). Such an effect would primarily eject heavy ions that would otherwise be gravitationally bound to the planet's atmosphere. Also, near the subsolar region, the electric field of solar wind can accelerate planetary ions, which may give rise to plume outflow.
2. The topical volume of a planet's magnetic field and stellar wind pressure determines the scale size of a planetary magnetosphere [Russell (2000 A)]. An intrinsic magnetosphere, being higher in dimensions, has a larger cross-sectional area for the interaction than an induced one. It implies that near the reconnection regions, stellar wind plasma has greater access to exchange energy and momentum with planetary ions. Blackman and Tar-duno (2018) showed that however, the rate of energy transfer is less than the induced magnetosphere case, still, a larger interaction area in a magnetized planet might contribute to increased solar wind capture.
3. Bulk ion escape refers to removing a large quantity of ionospheric particles in a single brief burst. It happens because a plasma shear instabil-

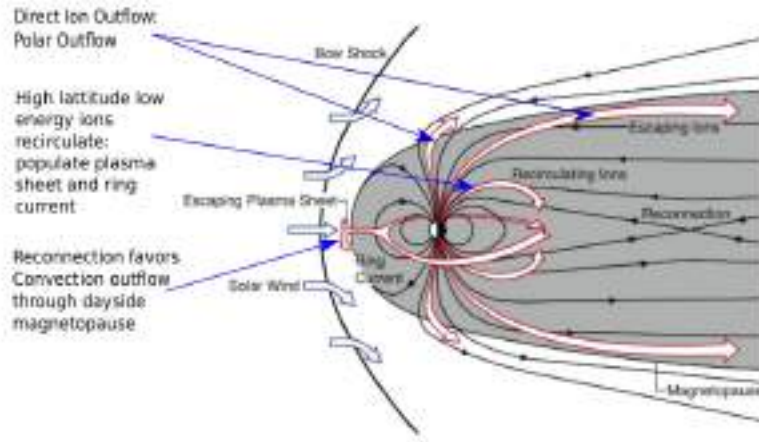


**Figure 4:** A schematic illustration of ion outflow from planet Earth. The black colour lines are representing magnetic field and the red peripheral arrows are showing the atmosphere erosion. The image was taken from [R. Strangeway's oral presentation at 52nd eslab symposium](#), and later edited for our study purposes

ity is introduced near the reconnection site due to highly variable plasma velocity. These fluctuations in wind velocity produce spatially changing pressure, which results in the formation of magnetic flux ropes ([Figure 5](#)). These ionospheric particles filled flux ropes got detached from their parent crustal site and got advected away due to  $J \times B$  lines of force. As a result, a planet loses a bulk amount of its atmosphere in a single fragment. This mechanism is highly essential for studying the atmospheric evolution of weakly magnetized planets.

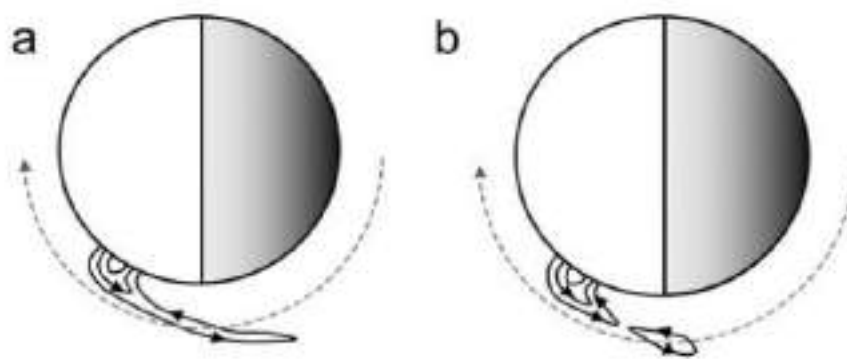


**Figure 5:** A cartoon sketch of bulk removal process near the strong magnetic site in the Martian atmosphere. a) Crustal field lines are elongated in the wind downstream region. b) Plasmoids of ionospheric plasma form which are carried away from Mars due to advection. The image was taken from [[Brain et al. \(2010\)](#)]

The points mentioned above clearly illustrate how a magnetic field presence in planetary volume can increase the atmospheric escape. It is not true that the magnetic field does not show any inhibition effects, for instance, by extending

the magnetosphere to a much farther environment where the stellar wind does not have any access to planetary ions. However, we will always observe some demerits of a planetary magnetic field because planetary ions are magnetically coupled to field lines. For example, [Gunell et al. \(2018\)](#) developed empirical models to quantify the effect of planetary magnetic moment on ion escape rates. The author expressed different escape mechanisms by different equations and did a comparative study for three hypothetical planets with an atmospheric environment similar to Venus, Earth, and Mars but with a variable magnetic moment. They found out that mass escape rate for both hydrogen and oxygen is similar for each of those planets in the unmagnetized range and also for the high magnetic moments. In-between those two extremes, mass loss rate from Earth-like planet was discovered one unit more than the other two hypothetical planets.

[Sakata et al. \(2020\)](#) also tried to understand the effects of an intrinsic magnetic field. The author took a Mars-like planet and ran some numerical simulations for a dipolar magnetic magnitude ranging from 0 nT to 5000 nT in five steps increment. Interestingly they observed that a critical value of the magnetic field (= 3000 nT) arises below (or above) which higher (or lower) atmospheric erosion happens. The physical reason they gave is the minimum magnetic strength required to balance the stellar wind pressure. The consequences of an intrinsic magnetosphere can also be witnessed at the cold, windy and gaseous planet of our solar system. Uranus, like our Earth, has an intrinsic magnetic field. Although the field strength is of similar order ( $\sim 0.3$  G), the Uranus magnetosphere is off-centered and is tilted  $53^\circ$  from the rotation axis. Furthermore, the rotation axis is almost parallel to the orbital motion, which makes it story special. Because of these characteristics, Uranus magnetosphere wobbles, resulting in the formation of plasmoids. [DiBraccio and Gershman \(2019\)](#), based on the 1986 Voyager-2 spacecraft data, reveals the presence of those plasmoids in its magnetotail. The author concluded that these bundles of magnetic flux are charged up with planetary plasma, which they observed to be traveling away from Uranus (similar to [Figure 5](#)). Thus, in respect of the above studies, it is possible that an intrinsic magnetic field might exacerbate atmospheric erosion rather than abate it.

The question we ask is, Do habitable worlds require a magnetic field? Or, if we keep all other habitable requirements for two planets equal, does the planet with a magnetic field will lose less atmosphere than the other? Or, the similar escape rate measured at Venus, Earth and Mars [[Strangeway et al. \(2010\)](#); [Barabash \(2010\)](#)] indicates the incapability of magnetic field shielding? We must remember that what we learn about the planetary magnetic field role in our solar system will form our foundation for understanding atmospheric evolution in magnetized and unmagnetized planets of other solar systems.

The problem is, how should we reveal the true nature of the planetary magnetic field? We cannot set up the magnetic field of sufficient size experimentally.

Also, varying solar wind makes the problem harder by continually changing dynamics. Mars, having a localized crustal field, weaker gravitational field, large plasma scale combined with an extended exosphere, and nominal solar wind conditions, provides us a unique natural laboratory to observe the ion loss due to the magnetic field alone [ [Dong et al. \(2015\)](#) ]. The presence of an inhomogeneous crustal field in Mars whose strength is varying hugely at the planetary surface and in surrounding makes our red planet a perfect "weakly magnetized" planet [ [Acuña et al. \(1999\)](#) ]. Furthermore, Mars interaction with the solar wind has characteristics of Venus-like, Earth-like, and comet-like, which fosters a complex interaction region where all-suite of escape processes occur [ [Brain \(2006\)](#) ]. Thus, with the above motivation, we will move on to chapter two, where we will briefly discuss our red planet properties.

## Part II

### THE SHOWCASE: MARS AND THE NUMERICAL MODEL

We continued by describing the general characteristics of the red planet. The lost dynamo of Mars, who ceases to exist around  $\sim 4$  byr ago, is still showing its effects in the form of the strong inhomogeneous crustal magnetic field. We demonstrated the current knowledge of this martian crustal field and proceeded on to a new picture of Sun-Mars interaction where the strong magnetic anomalies are present in the system. Afterward, we discussed some background studies related to Sun-Mars interaction and announced a set of questions that we have investigated in this dissertation.

The third chapter presents the framework of the numerical model. We wrote down the mathematical expression of the [MHD](#) equations and provided a brief interpretation of the initial set of parameters that we took for our study. The most important in this list is the modeling of the mini-magnetosphere, which we defined using ideal-dipole like equations to mimic the effects of the martian crustal field. In our next stage, we announced the name of the code that we have used, PLUTO, and continued writing about how we cast our system into the software. Finally, we take our departure after putting forward the outline of the interactions.



# 2

## MARS

The red planet, Mars, is named for the Roman god of war. The Romans thought that red color is an omen of destruction, and thus, they named their "god of avenger," the Mars.<sup>1</sup>. Though the actual reason for the red color atmosphere is because of the blowing away of oxidized iron dust (present at the surface) by the wind. Nevertheless, it seems quite interesting that Mars discovery dated back to 2<sup>nd</sup> millennium BCE. However, astronomically, it was first observed by Galileo Galilei in 1609<sup>2</sup>. In today's world, we all know Mars as a cold, barren desert planet positioned at a distance of  $\sim 1.5$  AU from Sun.

### 2.1 GENERAL CHARACTERISTICS

Mars is a small terrestrial or a rocky planet in the inner solar system. It is located at fourth position from Sun and it lies just outside the habitable zone [Vogel (1999)]. Its diameter is about half of the diameter of Earth, with barely  $1/10$  its mass. With a fraction of  $\sim 2/5$  earth's gravitational strength, Mars is holding on its thin atmosphere. The CO<sub>2</sub> rich atmosphere with a minuscule concentration of N<sub>2</sub>, O<sub>2</sub> and other gases, produces an average surface pressure of about 6.4 mbar at the atmospheric temperature of  $\sim 210$  K (-63 °C). Table 1 tabularize the general characteristics of Mars, and for reference, values of some physical parameters are compared with present-day Earth. The relatively large orbital eccentricity of Martian heliocentric orbit regulates the global solar input by up to  $\sim 50\%$  thus, charging up the red planet with variable solar input<sup>3</sup>.

Physical Parameters	Mars	Earth
Average distance from Sun	1.52 AU	1 AU
Orbital Eccentricity	0.093	0.0167
Mean Radius	3389.5 km ( $\sim 0.53 R_E$ )	6378 km
Mass	$6.39 \times 10^{23}$ kg ( $\sim 0.1 M_E$ )	$5.97 \times 10^{24}$ kg
Surface gravity	$3.7 \text{ m/s}^2$ ( $\sim 0.37 g_E$ )	$9.81 \text{ m/s}^2$
Mean surface atmospheric pressure	6.4 mbar	1014 mbar
Mean surface temperature	210 K (-63 °C)	288 K (15 °C)

**Table 1:** Bulk and atmospheric properties of present day Mars and for reference, Earth. The specific values are taken from [Mars Fact Sheet by NASA](#) and [Earth Fact Sheet by NASA](#)

<sup>1</sup> [How did mars and its moon get their names?](#)

<sup>2</sup> [ALL ABOUT MARS](#)

<sup>3</sup> [Robin Ramstad's Doctoral Thesis](#)

We, humans, have sent more missions to Mars than to any other planet. Though the distance is one of the reasons, the real motivation behind our scientific objectives is much different. Scientists had long ago suspected that there could be some leftover traces of biosignatures that might have originated in the early days of Mars [Westall et al. (2015)]. They have a good reason to believe in the possibility of extraterrestrial life. Before turning into a cold desolate world that we see today, Mars was once home to a large ocean, mountains bigger than the Mt. Everest, a multitude of active volcanoes carving out the beautiful geographical feature called valleys [Ojha et al. (2015)]. Even the liquid ice is still existing just a few inches below the martian soil [Piqueux et al. (2019)]. A curious question to ask here is, what happened to the Earth's twin? How does it lose its beautiful features? One of the speculated answers of these questions is hiding in the ancient magnetic dynamo of Mars, which ceased to operate around 3.7-4.0 billion years ago [Lillis et al. (2013); Johnson et al. (2020)]. The original cause(/s) of the disappearance of Martian dynamo is still puzzling scientists, but there might exist a clue in the minerals of Martian crust. It has been discovered recently that feeble remnant of that field is emanating from the planet's weakly magnetized crust [Acuña et al. (1999)].

## 2.2 CRUSTAL MAGNETIC FIELD

In the year 1965, NASA has its first successful attempt to Mars by launching its spacecraft called Mariner 4<sup>4</sup>. During its closest approach, Mariner 4 registered some significant magnetic field fluctuations. Assuming that these fluctuations were related to the Martian BS, Smith et al. (1965) concluded that martian magnetic dipole moment cannot exceed  $3 \times 10^{-4}$  the Earth dipole moment. However, other authors [Dryer and Heckman (1967)] have analyzed the same data and reported somewhat lower fraction  $\sim 2.1 \times 10^{-4}$ . Besides these calculations, a new debate arises concerning the origin of these fluctuations. Russell (1978) suggested that the fluctuations observed by Mariner 4 and future Soviets missions, Mars 3 and 5<sup>5</sup> were because of the interaction of solar wind with the Martian ionosphere. This was later favored by Riedler et al. (1989, 1991), who based on the Phobos 2 data concluded that magnetic field variation is not because of Mars intrinsic magnetic field.

The dispute about whether Mars possesses an intrinsic magnetic field was not resolved until 1997 when Mars Global Surveyor (MGS) took its first flight one year back and observed some magnetic oscillations through its Magnetometer and Electron Reflectometer (MAG/ER) in the near-Mars environment. Acuña et al. (1998) reported the first magnetic field and plasma observations of MGS and discovered that instead of a global magnetic field, Mars has strong, small-scale crustal magnetic sources associated with its ancient dynamo. As a matter of interest, they put up an upper bound on global dipole moment  $\sim 2 \times 10^{21}$  G-

---

<sup>4</sup> Mariner 4

<sup>5</sup> Robotic Missions to Mars

$\text{cm}^3$ , which corresponds to an equatorial field strength of 5 nT. The solar wind interaction was majorly found out to be Venus-like, representing an ionospheric-atmospheric interaction. In 1999, both [Acuña et al. \(1999\)](#) and [Connerney et al. \(1999\)](#) mapped out the geographical distribution of the crustal magnetic field. The magnetic field is dispersed more in southern hemisphere, particularly in the Terra Sirenum region ( $120^\circ \text{ W}$  to  $210^\circ \text{ W}$  and  $30^\circ \text{ S}$  to  $85^\circ \text{ S}$ , [Figure 6](#)). At an elevation of at least 100 km and spread over the spatial scale of  $\sim 200 \text{ km}$ , the magnetometer on [MGS](#) measured the maximum radial strength of  $\sim 1500 \text{ nT}$ , with an upper limit of  $\sim 1.3 \times 10^{17} \text{ A}\cdot\text{m}^2$  magnetic moment. The same magnetic field at 400 km above the surface drops to a magnitude of  $\pm 200 \text{ nT}$ . For reference, at the similar elevation, Earth's dipolar field and anomalies are 26000 nT and 10 nT respectively [[Brain \(2006\)](#)].

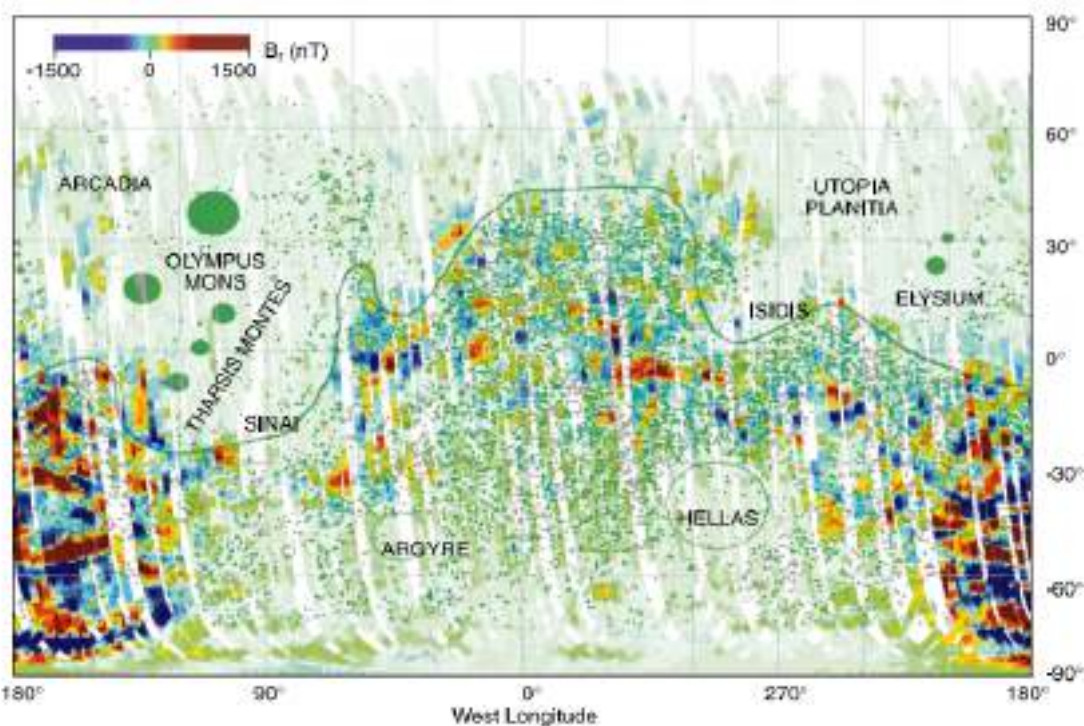


**Figure 6:** A pseudocolor map displaying out the geographical spread of crustal magnetic field. The strong colours represent the high magnetic field intensity as denoted by the colorbar. The plot is taken from [Acuña et al. \(1999\)](#) and in that reference, we request our readers to read it for the complete information.

The reduction in magnetic strength with increasing height motivated [Connerney et al. \(1999\)](#) (and other authors, [Hood and Zakharian \(2001\)](#)) to extrapolate [MAG/ER](#) measurements down to the surface. The author explained the above observations by assuming the crustal sources would be 20 uniform magnetized strips of width  $\sim 200 \text{ km}$  and in-depth of  $\sim 30 \text{ km}$ . This was explored in more detail by [Brain et al. \(2003\)](#), who did a combined morphology of solar wind and magnetic sources and concluded that infinitely long magnetic strips of surface magnitude  $\sim 16\text{-}20 \mu\text{T}$  in a depth of 40-100 km could fit the strong southern magnetic anomalies. Recently, [Morschhauser, Lesur, and Grott \(2014\)](#) and [Langlais et al. \(2019\)](#), based on their different spherical harmonic models reached to a

similar order ( $\sim 12000$  nT (or,  $12 \mu\text{T}$ )) of total surface field.

Typically, over  $\sim 70\%$  of the surface, the crustal field is observed to extend up to 120 km [Brain et al. (2003)]. This implies that the Martian magnetosphere is very thin. However, in the southern hemisphere where intense magnetic anomalies are present, the crustal lines can continue up to 1300 km [Mitchell et al. (2001); [Brain et al. (2003)]. Furthermore, magnetic topology observed in the Martian surrounding is a mixture of open, closed and draped field lines, similar to our Earth [Brain et al. (2007); Xu et al. (2020)]. Besides this, the draped IMF at Mars reaches up to a strength of 30-60 nT [Brain (2006)]. It means that the crustal field plays a significant part in the interaction of Mars ionosphere with the solar wind.

### 2.3 IMPACT OF CRUSTAL FIELD: A "NEW" PICTURE OF MARS-SUN SYSTEM

With the presence of an inhomogeneous magnetic field that can reach to different heights at different places, the Sun-Mars interaction becomes quite complex. The Martian crustal field not only affects the plasma boundaries but also dramatically influences the atmospheric erosion. Figure 7 shows an update from "induced" magnetosphere to "hybrid" magnetosphere.

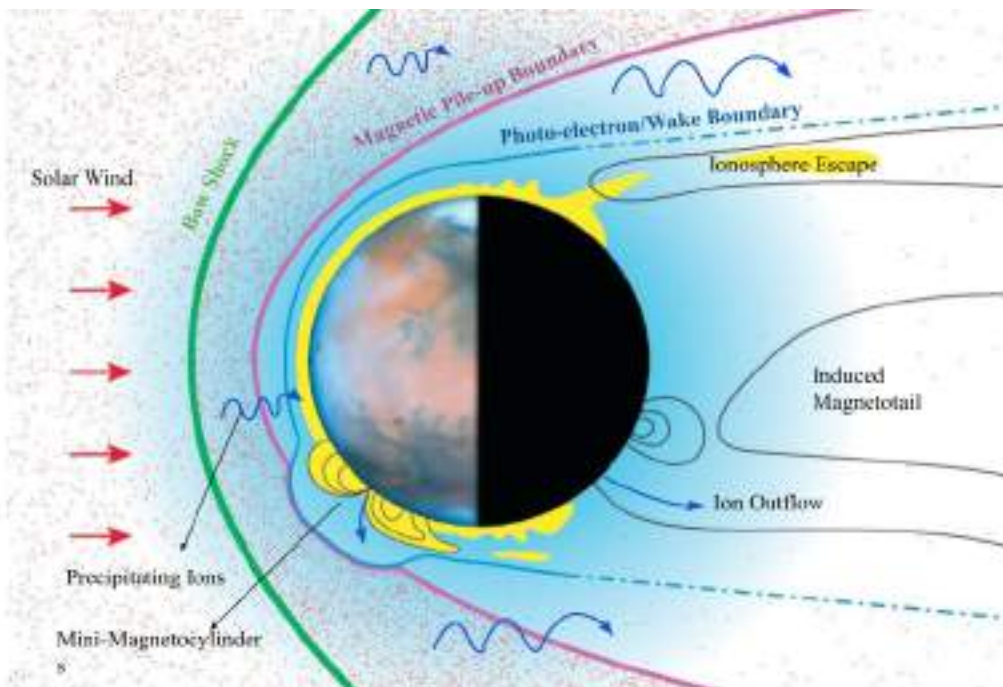


**Figure 7:** A cartoon sketch of martian hybrid magnetosphere. The above diagram is representing impact of crustal magnetic field by illustrating mini-magnetocylinders and ion escape through it. The image is taken from [Mars Atmosphere and Volatile Evolution \(MAVEN\) official twitter account](#) and later edited for our study purposes.

In the "new" picture of Sun-Mars interaction, similar features of the induced magnetosphere are present, but some noteworthy differences appear due to the crustal magnetic field. First, a small-scale spatial extension of magnetic field lines

called mini-magnetocylinders. These closed lines bubbles extending from the Martian surface signify the undisturbed magnetic field lines, similar to what we observed in Earth's magnetosphere. Their signatures are witnessed in [MGS](#) data [Ma et al. (2002)], and also the hybrid magnetic topology of Mars supports their attendance. Secondly, we observe the displacement of [MPB](#) to higher altitude at the strong crustal field locations [Vignes et al. (2000); Edberg et al. (2008)]. The physics behind this characteristic is the increase in the planet's magnetic pressure at the said environment, which provides an additional force against the incoming solar wind. Sometimes, a mini-magnetopause is formed positioned further out than [MPB](#) [Harnett and Winglee (2003)]. An important point to learn here is that the asymmetry in [MPB](#) and the formation of mini-magnetopause are the same things. The yellow color fluid in [Figure 7](#) shows that atmospheric particles are magnetically connected to the Martian crustal field. It means that the wind's magnetic field has direct access to planetary ions, and therefore, like the case of the intrinsic magnetosphere, magnetic reconnection will take place and shows its effects on the Mars atmosphere. For example, Episodic detachment of magnetic field (like the Uranus case [Section 1.3](#), or [Figure 5](#)) which leads to the bulk atmospheric escape is frequently observed at Mars [Brain et al. (2010)].

To physically understand the dynamics of charged particles and how the presence of the magnetic field affects their motion and leads to the atmospheric evolution, one needs to solve the complete set of Magnetohydrodynamics ([MHD](#)) equations (discussed in detail in [Chapter 3](#)). Solving these non-linear equations analytically is quite hard; thus, scientists make use of technology to make some sense out of them. Ma et al. (2002), based on a 3-D multispecies, single-fluid MHD model, studied the effects of the crustal field on an ionospheric atmosphere (composed of  $O^+$  and  $O_2^+$ ) of a Mars-like planet. The author integrated the equations for two cases: one with no intrinsic magnetic field and the other, where they used a 60-degree spherical harmonic model by Arkani-Hamed (2001) to mimic the crustal field. Based on their simulations, they concluded that overall ion escape is higher in the no magnetic field case due to the presence of obstacles to flows inside the [MPB](#). Conversely, Sakai et al. (2018) modeled heavy-ion loss ( $O_2^+$  and  $CO_2^+$ ) under two hypothetical conditions of no intrinsic field and weak intrinsic dipolar field (= 100 nT) and summarised that total ion escape rate increased by ~ 25% in the dipole case. Egan et al. (2019) pushed it to one step forward and simulated the interactions by varying the modeled intrinsic dipolar field value in a hybrid model. They reached to a similar result that the planetary magnetic field will favor ions loss until the magnetopause standoff distance reaches the [IMB](#). Hara et al. (2018) used the data from the latest [MAVEN](#) mission and inferred that global escape flux of planetary ions reduced by ~ 50% under the strong crustal fields. This was in agreement with previous studies, where, Lundin et al. (2011) based on the data from Analyzer of Space Plasma and Energetic Atomss ([ASPERA-3s](#))/acpIMA in Mars Express mission, deduced that the escape rate of planetary ions is statistically significantly higher (by about 35%) from the northern quadrant than from the southern quadrant, where the strong crustal field is located. The physical reason they gave is the formation of dayside

"mini-magnetospheres," which act as cellular structures and reduce the ionosphere's tailward escape by recycling the planetary plasma. However, Lundin et al. (2011) utilized the similar data and concluded that the overall effect of the crustal fields, if any, is small under nominal upstream solar wind conditions. The above set of the literature shows us that despite diverse research in the field, it is still poorly known how (and even whether) the crustal field influences the Martian atmosphere. However, it is also true that numerical models of various authors differ significantly in stellar wind input, boundary conditions, magnetic field distribution, and the process of analyzing satellite data (and interpreting too) is very different among the scientific community. Nevertheless, the question of crustal field impact, or in general, the planetary magnetic field influence, is still not evident.

Thus, with a curiosity to understand the role of an intrinsic magnetic field in SPI, we developed a three-dimensional MHD model for a Mars-like planet, which is interacting with a Sun-like star. Our code perfectly captures the shock physics, and the orientation of IMF is considered southward or northward, depending on the direction of the planetary dipole axis. To mimic the strong crustal field's effects, an off-centered, weak dipolar magnetic field is incorporated in the planetary crust. The primary reason to go for a mini-magnetosphere instead of the crustal field model is the freedom predetermined by the dipolar magnetic field. The "localized" dipolar arrangement produces a minimal but finite volume of the strong magnetization. Because of this, different physical phenomena can be isolated, revealing more easily the physics due to each element.

This dissertation addresses each of the following questions:

1. How does a planet having a small-scale spatially located magnetic field interacts with the magnetized stellar wind?
2. What differences arise in the magnetic topology due to the presence of a strong magnetic anomaly?
3. Does the presence of this intrinsic magnetic field affects the plasma boundaries like BS and MPB? And if yes, then how?
4. What is the impact of a mini-magnetosphere on the "local" atmospheric escape?

# 3

## NUMERICAL MODEL

---

James Clerk Maxwell set up the mathematical foundation of electromagnetic theory by formalizing the four fundamental laws which governs the behavior of the charges, currents, magnetic fields, and electron fields in plasma (or in general, everywhere <sup>1</sup>). They, together with the conservation of mass, momentum, and energy, governs the time evolution of physical variables, which describes the macroscopic behavior of conducting fluids. These sets of partial differential equations are collectively called **MHD** equations.

### 3.1 MHD EQUATIONS

**MHD** describes the large scale, slow dynamics of plasma where the single fluid approximation is valid. We can treat the collective motion of charged particles as fluid because the charge separation is negligible. The typical length scale (and time scale) of the system is much larger than the Debye length (and plasma frequency). To capture the shock physics, we took an adiabatic equation of state with a polytropic index of value  $5/3$ . Besides, the following set of resistive **MHD** equations are simulated for our plasma system:

$$\frac{\partial \rho}{\partial t} + \nabla \cdot (\rho \mathbf{v}) = 0 \quad (1)$$

$$\frac{\partial \mathbf{v}}{\partial t} + (\mathbf{v} \cdot \nabla) \mathbf{v} + \frac{1}{4\pi\rho} \mathbf{B} \times (\nabla \times \mathbf{B}) + \frac{1}{\rho} (\nabla P) = \mathbf{g} \quad (2)$$

$$\frac{\partial E}{\partial t} + \nabla \cdot [(E + P)\mathbf{v} - \mathbf{B}(\mathbf{v} \cdot \mathbf{B}) + (\eta \mathbf{J}) \times \mathbf{B}] = \rho \mathbf{v} \cdot \mathbf{g} \quad (3)$$

$$\frac{\partial \mathbf{B}}{\partial t} + \nabla \times (\mathbf{B} \times \mathbf{v}) + \nabla \times (\eta \mathbf{J}) = 0 \quad (4)$$

The [Equation 1](#), [Equation 2](#), [Equation 3](#), and [Equation 4](#) are called equations of mass-continuity, momentum transfer, energy and magnetic induction. They are derived from basic conservative laws along with the Maxwell laws of electromagnetism. The variables  $\rho$ ,  $P$ ,  $E$ ,  $\eta$  denote the density, total pressure, total energy density, magnetic diffusivity and the parameters in bold font  $\mathbf{v}$ ,  $\mathbf{B}$ ,  $\mathbf{g}$  and  $\mathbf{J}$  represents the stellar wind velocity vector, total magnetic field vector, gravitational acceleration and total current density. The notation  $E$  represents the sum

---

<sup>1</sup> This paper pretty much sums up Maxwell's revolutionary work, which at some point of my life inspired me immensely

of magnetic energy density, kinetic energy density, and thermal energy density. The variable  $P$  defines the sum of total magnetic pressure ( $p_B = \frac{B^2}{8\pi}$ ) and thermal pressure ( $p_t = nK_B T$ ), where for stellar wind (sw) or for planetary ions (pl) is  $n_{sw/pl} = \frac{\rho_{sw/pl}}{m_p}$ , where  $T$  and  $m_p$  is the temperature and rest mass of proton. It is true that in a single-species model, planetary ions and stellar plasma cannot be separated. However, with the help of scalar tracers, we can distinguish them approximately. For example, stellar wind dynamic pressure is calculated using  $P_{sw} = \rho_{sw} v^2$ .

### 3.2 GRID CONFIGURATION

We ran our code in Planet-fixed cartesian coordinate system, such that our hypothetical planet is at the origin (0,0,0), the x-direction points from the planet against the pristine upstream stellar wind velocity vectors, the z-direction points from North (N) to South (S) magnetic poles having zero-tilt with dipole axis and the y-direction is completing the right-handed coordinate system. Our computation domain varies from  $x \in [-25 R_M : 100 R_M]$ ,  $y \in [-25 R_M : 25 R_M]$ ,  $z \in [-100 R_M : 100 R_M]$ , where  $1 R_M = 3389.5$  km. In all the three directions, the uniform mesh refinement is implemented with the rectangular grid cells of the number,  $[N_x, N_y, N_z] = [317, 234, 400]$ . However, the degree of refinement does not remain uniform throughout the simulation box. In the planet's vicinity ( $[-3 R_M : 3 R_M]$ ), we used 120 square grids to have the finest grid resolution of  $0.05 R_M$  ( $\sim 169.5$  km) in all three directions. Then, we decreased our resolution to  $0.1 R_M$  till  $\pm 5 R_M$ , and to  $0.25 R_M$  for areas covered by the regions  $[5 R_M : 10 R_M]$  or,  $[-10 R_M : -5 R_M]$ . [Table 2](#) describes the picture. The aforementioned non-uniform grid structure is chosen to resolve the dynamics above the planetary surface fairly and to complete the simulations in a reasonable real time.

$x \in [-25 R_M : 100 R_M]$ , $y \in [-25 R_M : 25 R_M]$ , $z \in [-100 R_M : 100 R_M]$ $[N_x, N_y, N_z] = [317, 234, 400]$			
Region	All three directions?	No. of cells	Resolution
$[-3 R_M : 3 R_M]$	YES	120	$0.05 R_M \sim 169.5$ km
$[-5 R_M : -3 R_M]$ , $[3 R_M : 5 R_M]$	YES	20	$0.1 R_M \sim 339$ km
$[-10 R_M : -5 R_M]$ , $[5 R_M : 10 R_M]$	YES	20	$0.25 R_M \sim 847$ km
Remaining domain	YES	Variable for each direction	$0.9 R_M \sim 3050$ km

**Table 2:** The Grid Extent and Resolution

### 3.3 INPUT PARAMETERS

We introduced the stellar wind through the left boundary ( $yz$  plane) with a velocity vector of  $[270,0,0]$  km/s concerning our coordinate system. The wind's temperature and density is taken to be  $4 \times 10^4$  K ( $\sim 4$  eV) and  $4 \rho_{\text{amb}}$ , where  $\rho_{\text{amb}} = 9 \text{ cm}^{-3}$ . Though the mean solar wind speed is reported to be in order  $\sim 400$  km/s [Halekas et al. (2017); Marquette et al. (2018)], we chose the above specific value to describe a quiet solar environment. Also, the density can be considered  $4 \text{ cm}^{-3}$  as the whole system is immersed in an ambient medium. The IMF of strength 4 nT is taken only in the  $B_z$  direction, where its orientation is considered northward or southward with respect to the unit vector in the  $z$ -direction. The planetary properties and other physical parameters are tabularized in [Table 1](#) and [Table 3](#). The stellar wind proton population is assumed to follow adiabatic behavior ( $\gamma = 5/3$ ), and the value of magnetic diffusivity is motivated from [Das et al. (2019)]. One point to note here that the above parameters produce stellar wind of dynamic pressure  $\sim 0.5$  nPa (in respect to ambient medium), which corresponds to magnetic pressure with a strength of approximately 35 nT.

Physical Quantities	Notation	Value Used
Density of ambient medium	$\rho_{\text{amb}}$	$1.5 \times 10^{-23} \text{ g/cm}^3 (= 9m_p)$
Stellar wind density	$\rho_{\text{sw}}$	$6 \times 10^{-23} \text{ g/cm}^3 (= 4\rho_{\text{amb}})$
Stellar wind velocity	$v_{\text{sw}}$	270 km/s ( $\sim 0.77 \times 350$ km/s)
Ambient medium velocity	$v_{\text{amb}}$	0.0
Temperature	$T_0$	$4 \times 10^4 \text{ K}$
Polytropic Index	$\gamma$	$5/3$
Planetary magnetic strength	$B_0^*$	312.5 nT (= 0.003125 Gauss)
Dipole tilt angle	$\theta_{\text{pl}}$	$53^\circ$
Dipole position	$O' \in (x_0, y_0, z_0)$	(1800 km, 0, 2387.5 km)
Dipole distance from origin	$r_0$	2989.5 km
IMF strength	$B_{\text{sw}}$	4 nT
Magnetic diffusivity	$\eta$	$10^{13} \text{ cm}^2 \text{s}^{-1}$

**Table 3:** List of physical parameters and their respective notations. (\*) signifies the magnetic intensity at surface dipole location, instead of conventional equatorial dipole field. For more information, please refer to [Section 3.5](#)

### 3.4 PLANET'S THIN ATMOSPHERE

To model our planet's plasma environment, we defined a one-dimensional radial density profile of  $H^+$ , as shown in [Figure 8](#). We used a similar methodology devised by [Das et al. (2019)] to initialized our atmosphere with a single change of  $\rho_{\text{pl}} = 20 \rho_{\text{amb}}$  (for  $r \leq r_{\text{pl}}$ ), characterizing our Martian environment. For the sake of completion, we have mentioned the methodology in [Appendix A](#). Rahmati et

al. (2017), based on MAVEN data, reported much higher neutral H density at an altitude of  $10^3$ - $10^4$  km. However, we took such low density to reduce the impact of the planet's atmosphere on interactions. The above choice of density enables us to have a gravitationally stratified atmosphere where we can investigate the effects of the magnetic field distinctly. Thus, on the above grounds, we called it a thin atmosphere, having a mass of about  $\sim 400$  kg only. However, it is required to keep in memory that we are simulating interactions for a Mars-like planet. Hence, in no-manner, we are calling our density profile to be of actual Mars. But, we also emphasized to consider it from the perspective of a hypothetical planet having a thin atmosphere of ionized hydrogen atoms.

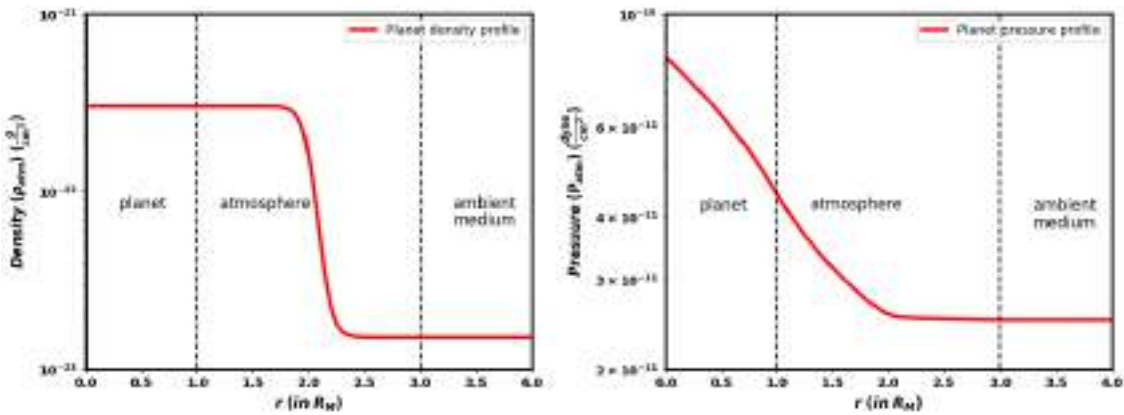


**Figure 8:** (Left) Density and (Right) Pressure profiles of planetary atmosphere which are considered as initial conditions for the simulations.

### 3.5 MINI-MAGNETOSPHERE

Brain et al. (2003) suggested that a dipolar field like structure can be implemented to mimic strong magnetic anomalies if the source depth is taken a few hundred kms below the surface. So, we defined an off-centered, weak dipolar magnetic field of finite spherically magnetized volume [ $V \sim (400 \text{ km})^3$ ] having the magnetic moment of  $1.17 \times 10^{17} \text{ A}\cdot\text{m}^2$ . The dipole buried 400 km below the surface at the location of  $53^\circ \text{ S}$ ,  $270^\circ \text{ W}$  produces magnetic strength of 160 nT at 100 km altitude, roughly one-tenth of the maximum observed anomaly. We conveniently chose the XZ plane to have direct interactions of stellar wind with the mini-magnetosphere. The following set of equations governing the magnetic field intensity due to a point dipole at an arbitrary location are exploited here to initialize the planet's magnetic field:

$$B_x = -\frac{B_0 V}{f} \left( \left[ \frac{3(x - x_0)(z - z_0)}{(r - r_0)^5} \right] \cos \theta_{pl} + \left[ \frac{3(z - z_0)^2 - (r - r_0)^2}{(r - r_0)^5} \right] \sin \theta_{pl} \right) \quad (5)$$

$$B_y = -\frac{B_0 V}{f} \left( \left[ \frac{3(y - y_0)(z - z_0)}{(r - r_0)^5} \right] \right) \quad (6)$$

$$B_z = -\frac{B_0 V}{f} \left( \left[ \frac{3(z-z_0)^2 - (r-r_0)^2}{(r-r_0)^5} \right] \cos \theta_{pl} - \left[ \frac{3(x-x_0)(z-z_0)}{(r-r_0)^5} \right] \sin \theta_{pl} \right) \quad (7)$$

where the values of the above physical notations are given tab:physicalparameters. Figure 9 describes the magnetic field configuration ,and for a complete picture, please refer to its caption. Because, here,  $B_0$  denotes the magnetic field strength at dipole location instead of traditional equatorial magnetic intensity, a factor of angular conversion is taken into account. We called this dimensionless factor 'f', which is equal to 1.7069 for our case. The final result from the underlying theory of the factor mentioned above (illustrated in Appendix B) is  $f = [4\cos^2(90^\circ - |\theta_L|) + \sin^2(90^\circ - |\theta_L|)]^{1/2}$ , where  $\theta_L$  stands for the angle between the equatorial line (OE) and a dipole's position vector (OO'). For our study,  $\theta_L$  is equal to  $53^\circ$  as marked in Figure 9. To have a rough idea of the position of mini-magnetopause, we plotted a contour line of magnetic strength 35 nT. This magnetic strength corresponds to an altitude of  $1.1 R_M$  from the origin (as  $B \propto 1/r^3$ ) and hence, provides us the theoretical bound on magnetopause.

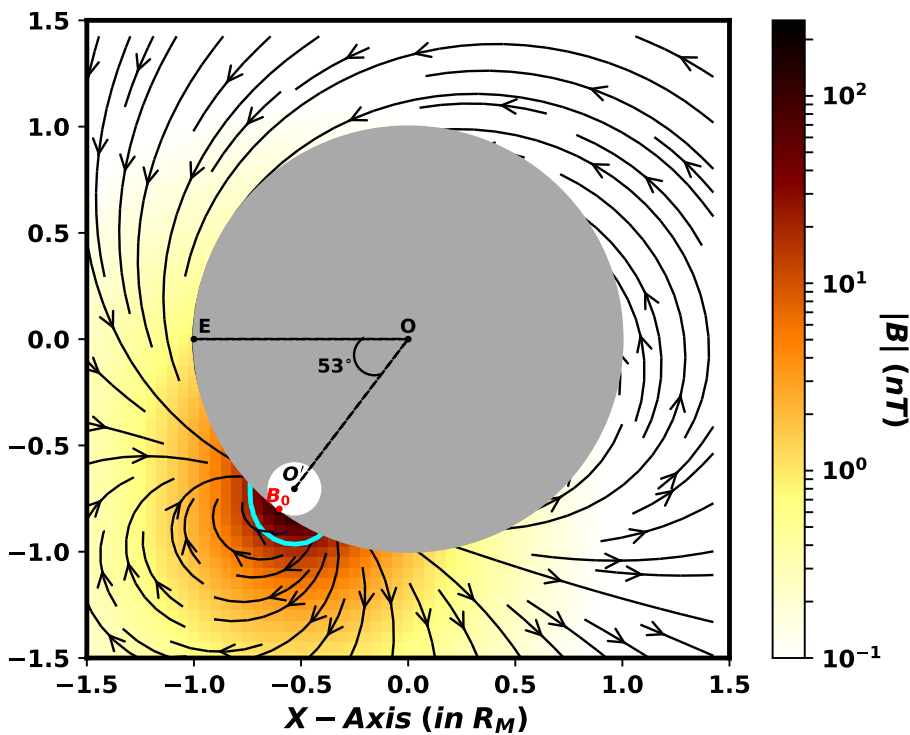


**Figure 9:** XZ sliced pseudocolor plot of modeled intrinsic magnetic field. Black colour arrows describes the magnetic streamlines, whereas gray shade, white circular patch, point O and O' represents the planet, magnetized volume, planet's center and the dipole location. The acute angle of  $53^\circ$  describes the orientation of position vector of dipole. A red colour point  $B_0$  marks the surface magnetic strength at dipole location and in addition,  $|B| = 35$  nT contour line (in cyan colour) is plotted for a rough idea of mini-magnetopause.

### 3.6 OUR NUMERICAL SCHEME: STAR-PLANET INTERACTION MODULE

For our study, we use the Star-Planet Interaction Module (**SPIM**) of [Das et al. \(2019\)](#). The numerical script is devised for a 3D compressible MHD code software called **The PLUTO Code**, where we employed the newest version (ver. 4.3; [Mignone et al. \(2007\)](#)) for our system. It is a finite difference code designed to integrate a system of conservation laws, that is governed by their partial-differential equations (like [Equation 1 - Equation 4](#)), Ordinary differential equations and other non-linear equations.

#### 3.6.1 Problem Setup and Initialization

The PLUTO header file *definitions.h* has numerous options that demand to be specified. The options that we have used along with user defined constants are enlisted in [Table 4a](#) and [Table 4b](#)

Model Options	Parameters Used
Physics Module	MHD
No. of Dimensions	3
No. of Components	3
Geometry	CARTESIAN
Body Force	VECTOR
Reconstruction	LINEAR
Time Stepping	RK2
Equation of State	IDEAL GAS
Divergence Control	DIV_CLEANING
Background Field	YES
Resistivity Scheme	Super-Time-Stepping
Internal Boundary	YES
Limiter	MINMOD_LIM
Vector Potential	Not used

(a) List of essential options specific to this sample simulation

User Defined Parameters/ Constants	Values used (CGS units)
THETA	53 °
ALPHA <sup>(*)</sup>	20.
UNIT_DENSITY ( $\rho_{amb}$ )	9.*m <sub>p</sub>
UNIT_LENGTH (R <sub>M</sub> )	3.38 × 10 <sup>8</sup>
M <sub>pl</sub>	6.39 × 10 <sup>26</sup>
UNIT_VELOCITY (v <sub>0</sub> )	3.5 × 10 <sup>7</sup>

(b) User defined variables

**Table 4:** PLUTO (incomplete) definition file for our reference simulation

The complete information of what above labels mean is provided in **PLUTO User's Guide**. The PLUTO Source file *init.c* provides a set of functions that can be utilized to set up the initial conditions, background field (like the dipolar field in our case), body forces, run-time data analysis and user-defined (*userdef*) boundary conditions. The primitive physical variables are located by means of

an index like,  $\rho = v[RHO]$ ,  $v_x = v[VX1]$ ,  $B_y = v[BX2]$ , etc. For instance, in *Init()* function, we defined our atmospheric density as:

$$v[RHO] = \rho_{pl}/Ud + (1./Ud) * (Ud - \rho_{pl}) * 0.5 * (\tanh(9(|r| - 2.0)) + 1);$$

where  $|r| = (x^2 + y^2 + z^2)^{1/2}$ , Ud is Unit\_Density and  $\rho_{pl} = ALPHA * Ud$ , whose values are called from *definitions.h* file (shown in [Table 4](#)([Table 4b](#))).

For some "necessary to go through" options, please look at below description:

1. **Body Force:** Depending upon a planet's location, a star can interact with a planetary atmosphere via gravitational, tidal, frictional, or some other "close-interaction" forces. When a planet is far away i.e., at a distance of at least 0.1 AU, all these forces become negligible compared to a planet's gravitational field. Thus, we have considered only the newton's gravity as a body force for our study. In PLUTO environment, we defined the planet's gravity in *BodyForceVector()* function using g[DIR], g[JDIR] and g[KDIR], where IDIR,JDIR and KDIR represents x, y and z-direction.
2. **Background Field:** We defined our dipolar magnetic field in the *BackgroundField()* function because they are the force-free magnetic field. The corresponding equations are given in [Section 3.5](#), where we defined their x,y, and z components using Bo[DIR], Bo[JDIR], and Bo[KDIR]. As advised in the [PLUTO User's Guide](#), we used a Background Field Splitting method to avoid negative pressure problem.
3. **DIV\_CLEANING:** Maintaining Gauss's law of magnetism ( $\nabla \cdot B = 0$ ) at each step of computation is a big problem in computational [MHD](#). Extraneous errors with no physical meaning start coming up when we do not take care of it. The magnetic field assumes wrong topologies and, therefore, results in unscientific plasma flows perpendicular to the magnetic fields. Such effects can accumulate and ultimately give completely different results than what is expected from the simulations. Thus, to avoid us from trapping into that situation, we enforced the divergence constraint by setting YES to divergence cleaning. The particular method we used is known as Hyperbolic Divergence Cleaning. Please look at up [PLUTO User's Guide](#) for more information.
4. **Equation of State:** For our simulations, we used the IDEAL Equation of state to keep the ratio of specific heat capacity at constant pressure and volume constant.
5. **Tracers:** According to PLUTO guidelines, tracers are passive scalars that act like some water painting. These scalar functions do not participate actively in the electrodynamics of the system but simply follow the advection or mass-continuity equation controlled by the actual density, pressure, flow, and the magnetic fields in the system.

$$\frac{\partial \rho_k}{\partial t} + (\mathbf{v} \cdot \nabla) \rho_k = Q_k \quad (8)$$

where  $\rho_k$  denotes density of the  $k$ -th tracer,  $\mathbf{v}$  denotes the velocity vector and  $Q_k$  stands for source or sink term for the  $k$ -th tracer. For our algorithm, we use the tracers in two cases:

- (a) To separate the stellar wind from planetary ions.
- (b) To represent a part of the atmosphere. As a result, any outflow of these tracer elements from inside the internal boundary denotes the loss of atmosphere of the planet, effected by the stellar wind flow.

The tracers are implemented using the notation TRC in the file *init.c*.  $v[TRC]$ ,  $v[TRC+1]$ ,  $v[TRC+2]$  denotes the variables which are used in assigning the above three tracer values respectively. The detailed informed about their employment are provided in [Section 3.6.2](#).

We used 2<sup>nd</sup> Runge Kutta numerical scheme to integrate ([Equation 1](#)-[Equation 4](#)) and Super-Time-Stepping ([STS](#)) for fast thermal conduction. Though, various time-stepping algorithms are allowed in PLUTO code, we specifically used [STS](#) to accelerate the process. However, due to above scheme, we had to shut down the HALL\_MHD term, as it is not compatible with [STS](#).

### 3.6.2 Boundary Conditions

We employed three different types of boundaries in *UserDefBoundary()* function for our simulations: Inflow Boundary, Lorentz free -flow boundaries, and Internal Boundary.

1. **Inflow Boundary:** This is the boundary from where stellar wind enters the computation domain. We fixed the wind's parameters at this boundary and determined the shock parameters using Rankine-Hugoniot jump conditions. Please refer to the [Appendix C](#) for the physics behind the shock generation. Now, because we are using the "Background Field Splitting" in our simulation, the input boundary would have a magnetic field:  $B_{\text{boundary}} = B_{\text{actual}} - B_{\text{dipole}}$ , where  $B_{\text{boundary}}$  is the applied field at a boundary,  $B_{\text{actual}}$  is the field that is present in the real system (0 at t=0) at that boundary and  $B_{\text{dipole}}$  is the background planetary dipolar field.
2. **Lorentz force-free boundaries:** We defined the Lorentz free-force condition at the other five boundaries (surfaces of our computational box). We enforced the normal component of the Lorentz force to vanish at these boundaries. By doing this, we ensured that the magnetic tension force did not produce an inflow into or an outflow from the simulation domain due to any boundary effect.

For no normal component of Lorentz force, we must satisfy the relation:

$$(\nabla \times \mathbf{B})_n = 0 \quad (9)$$

Now take the example of a y-boundary. To vanish the normal component of the Lorentz force at this boundary, we would have to set the y-component to zero. From [Equation 9](#), this would mean that:

$$j_z B_x - j_x B_z = 0 \quad (10)$$

An easy way to satisfy this would be to set  $j_z$  and  $j_x$  at the y boundaries to zero is:

$$\frac{\partial B_x}{\partial y} = \frac{\partial B_y}{\partial x} \quad (11)$$

$$\frac{\partial B_z}{\partial y} = \frac{\partial B_y}{\partial z} \quad (12)$$

3. **Internal Boundary:** We kept planetary volume as an internal boundary, and flagged it to avoid any physical quantities to evolve over time. The stellar wind velocity vectors are enforced to hold "zero" value, thus, setting up a absorbed boundary condition for them. The planetary density and pressure are called using the pointer d, like,

$$d \rightarrow Vc[RHO][k][j][i] = \frac{\rho_{pl}}{Ud} + \frac{1}{Ud} * (Ud - \rho_{pl}) * 0.5 * (\tanh(9(|r| - 2.0)) + 1);$$

### 3.6.3 Initialization of Tracers and Shock Front

Tracers played a crucial part in our "atmospheric escape" study. We defined three tracer functions, in which one of them is used to color stellar plasma and the other two to represent a different part of the planetary atmosphere. First, we put all of them as o in *init()* function of file *init.c*. Then, we defined their functions in the user-defined boundaries, as described in the previous section.

1. **Stellar Wind Tracer:** This tracer is initialized to be zero everywhere in the domain and held at a constant value of 1.0 at the inflow boundary. This is representative of the density of the stellar wind normalized to the incoming density of stellar wind.
2. **Atmospheric Tracers:** To compare the atmospheric escape from the northern and southern hemispheres, we defined two tracers in each part of the planet representing a small equal portion of dayside atmosphere. This is achieved by using an exponential 1-D radial function, which we displaced by a distance depending upon the tracer location. For instance, for the southern hemisphere, our scalar function goes from dipole's surface location to 0.5  $R_M$  above the surface:

$$f(r_{dip}) = \exp^{-(r_{dip}-0.1)^2} \text{ for} \quad (13)$$

where  $r_{dip}$  denotes the position vector of the dipole. The offset of  $0.1 \sim 400$  km is included to begin the function from the planetary surface. Elsewhere

in the domain, this tracer is equal to 0. A similar procedure is done for the northern hemisphere tracer but with a single change. Instead of taking dipole's position vector, we took its mirror image in xy plane, i.e., a vector having its tail at  $53^\circ$  N,  $270^\circ$  W location.

As mentioned in the previous section, we want the stellar wind to strike the planet as a shock front. To do so, we need to satisfy the Rankine-Hugoniot condition (please refer to [Appendix C](#) for detailed explanation).

Region	Velocity (in $v_0$ )	Density (in $\rho_{\text{amb}}$ )	Magnetic Field (in $B_0$ )
In Ambient	0.0	1.0	$2.4 \times 10^{-7}$
In Shock ( $x_{\text{left}}$ boundary)	0.7724708	3.999546	$7.999987 \times 10^{-7}$

**Table 5:** Table showing choice of parameters to get  $v_{sw} = 270$  km/s

We have approximated the value of the magnetic field at the left boundary as  $B_0/(25^3)$  because we are finding the value of field at  $x_{\text{left}} = 25$ . This works well with our simulations because the shock parameter values are very weakly sensitive to the precise value of the magnetic field. Referring to [tab:shockfront](#) we can initialize the parameters in the inflow boundary ( $X1_{\text{BEG}}$ ). Please note that these are the values that we need to provide in the  $x_{\text{left}}$  boundary only, throughout the simulation:

- Velocity (in terms of  $v_0$ ):  $v_x = 0.7724708$ ;  $v_y = 0.0$ ;  $v_z = 0.0$
- Density (in terms of  $\rho_{\text{amb}}$ ):  $\rho_x = 3.999546$ ;  $\rho_y = 0.0$ ;  $\rho_z = 0.0$
- Magnetic field (in terms of  $B_0$ ):  $B_x = 7.999987 \times 10^{-7}$ ;  $B_y = 0.0$ ;  $B_z = 0.0$

Once again, it should be noted that the magnetic field values here are the total field  $B_{\text{total}}$  at the  $x_{\text{left}}$  boundary. To initialize the variables  $BX1$ ,  $BX2$ , and  $BX3$ , we need to determine the residuals ( $B_{\text{res}}$ ) by deducting the background field ( $B_0$ ).

### 3.7 AN OUTLINE OF THE INTERACTION

A qualitative summary of the interaction between stellar-wind and planetary ionosphere embedded (or not embedded) with a mini-magnetosphere (in this case, we take the Sun-Mars system for simplicity) is itemized below:

- The solar wind fires off at the Sun. From [Parker \(1965\)](#) model on solar wind, we know that the wind begins with a subsonic speed and accelerates at the transonic point to supersonic speeds. This wind carries plasma, which is “frozen-in” with the magnetic fields that it drives away from the star. Therefore, this supersonic, magnetized plasma gas moves through the interplanetary medium towards Mars.

- As the wind reaches close to 1.5 AU, the exosphere-ionosphere of Mars starts to feel the presence of the magnetized solar wind. This supersonic plasma starts heating and compressing up due to the presence of the planetary ions, along with the trailing supersonic wind, which leads to the formation of [BS](#). High fluctuations in density, speed, and magnetic field magnitude are found in this transition area, whose geometry and location depends on the [IMF](#) plane, presence/absence of intrinsic magnetic field (maybe), etc. as described more in [Section 5.1](#)
- After its passage through the [BS](#), the subsonic solar wind reaches in the vicinity of Mars, where its frozen magnetic field lines begin stacking up due to highly conductive ionospheric medium. As a result, the magnetic pile-up region forms in the Sun-facing side of the planet, whose location can be determined by tracing the distinctive signatures in the magnetic field components ([Section 5.4](#)). Whereas in the case of an intrinsic magnetic field, mini-magnetopause forms whose curvature and location depends on the pressure balance condition. Further illustrations can be found in [Section 5.5](#)).
- In both cases, the [IMF](#) got draped around the planet and built the magnetotail region. However, if the planet's magnetic field is On, magnetic reconnection may take place in the dayside and nightside of the planet, which leads to the magnetic topology dissimilar to the no dipolar case. This contrasting nature in the magnetic topology can be understood in terms of physical variables like a magnetic field, current, plasma pressure, etc., which we have described in detail in [Chapter 4](#).
- These dissimilarities also affect the atmospheric escape mechanism. The solar wind ions moving in the interplanetary medium may get direct access to channelize their energy through the reconnected lines of the dayside and nightside region. However, they could also get deflected and scattered away to the locations far off from the planetary surroundings. This competing nature of the magnetic field in the context of "local" atmospheric escape is illustrated more in [Chapter 6](#).



## Part III

### RESULTS

The following three chapters present the results of this work. Chapter 4 deals with the consequences of magnetic reconnections, such as forming the hybrid magnetic topology in the simulations. Further analysis shows that magnetic connectivity decreases the strength of magnetic deviation and current density in the magnetotail. Besides this, we observed that mini-magnetosphere deflects and decelerates the solar wind particles. In the next chapter, we investigated the effects of the dipolar field on the structure and location of plasma boundaries. BS displayed asymmetry; however, the value was not much significant. No MPB formed in our simulations, but the sub-solar location of a similar region is estimated by identifying the respective signatures. The simulations exhibit the formation of a mini-magnetopause in the southern hemisphere. Besides, we observed the marsward displacement of this boundary during the periods of S-IMF. Chapter 6 holds the most critical aspect of this study. We estimated the atmospheric escape from an equal part of the north- and south-hemisphere for the case when IMF is oriented southward. The results distinctly favor the role of mini-magnetosphere in the protection of the atmosphere. Then, we investigated the effects of IMF and found out that efficient magnetic connectivity in S-IMF leads to higher local mass-loss in it. At the close, we compared the mass-loss rate in the absence and presence of an intrinsic magnetic field. We discovered that higher atmosphere is getting escaped in the absence of mini-magnetosphere.

In Chapter 7, we conclude our results.



# 4

## MAGNETIC RECONNECTION AND ITS CONSEQUENCES

---

The breathtaking foundation of magnetic reconnection goes back to the early 50<sub>s</sub> of the 20<sup>th</sup> Century. In the 1950<sub>s</sub>, the cosmic ray detector witnessed the high energy ions of an order of 10 GeV connected with the solar activity <sup>1</sup>. The cause of such energetic particles perplexed the scientific community as no such events were recognized earlier. Giovanelli (1946) suggested the mechanism of an induced electric field generated by the large change in magnetic flux in sunspots, which appears to accelerate the charged particles. Parker (1957) (and Sweet) continuing on this idea, developed a first quantitative model of magnetic reconnection. They proposed that when two magnetic field lines of opposite polarity are pushed against each other in a highly conductive medium, an interdiffusion of field lines takes place due to the vanishing of the field in the reconnection plane. This conveys the conversion of magnetic energy of fluid into the plasma's kinetic and thermal energy. The overall magnetic topology gets altered, and we find a system with new characteristics. In 1961, Dungey (1961) used this mechanism to explain the acceleration of charged particles in Earth's auroral zone. The author proposes a qualitative model, demonstrating how the IMF and Earth's magnetic field comes close, breaks up, reconnect, and finally produces the topology that we all see today.

### 4.1 PHYSICS OF MAGNETIC RECONNECTION

In the magnetofluid of zero electrical resistivity, plasma particles on two different lines always lie on the same field line due to the conservation of magnetic flux [Choudhuri (1998, Ch. 15)]. It implies that two fluid elements far from each other, but on the same magnetic field line, always remain connected to each other, no matter what happens to the magnetofluid. As a result, some constraints are introduced to the dynamics. The science of breaking off those constraints refers to the magnetic reconnection. When a small but finite electrical resistivity ( $\eta$ ) is introduced in the system, the last term in Equation 3 and Equation 4 has some finite value, which prohibits the conservation of magnetic flux. As a result, a magnetic structure is formed that demagnetizes the charged particles. Therefore, ions and electrons are no longer tied to one magnetic field line and can drift across the plane of reconnection. As charged particles in motion draw out the magnetic lines of force, we visualize this process in terms of breaking and recombination of the reversely directed magnetic field lines. Figure 10 describes the reconnection process in two-dimensional geometry. The two oppositely oriented magnetic field lines (in red and blue color) are approaching close to each other. Then in the plane of finite electrical resistivity, they diffuse and reconnect to the opposite ends of each other and finally showing us the new magnetic

---

<sup>1</sup> A brief history of magnetic reconnection

configuration. The diffusion of the magnetic field is directly proportional to its gradient, which is associated with the large current densities. Thus, a current sheet is formed in the reconnection plane. Electrons and ions move with high speed in this region due to the availability of kinetic and thermal energy from the lost magnetic energy. This process goes on forever until some viscosity is injected into the system.

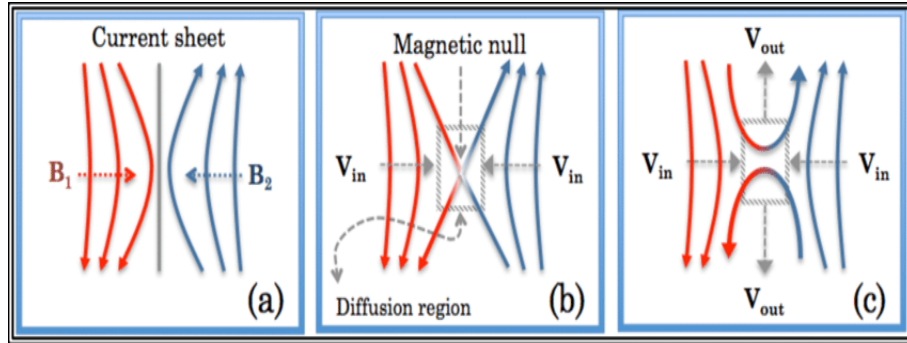


**Figure 10:** A schematic illustration of magnetic reconnection in two-dimensional geometry. a) Two oppositely direct field lines (in red and blue colour) approaching close to each other. b) Opposites end of a red colour and blue colour line connects with each other in the reconnection plane. c) Formation of new magnetic topology and a current sheet. The black arrows are depicting the velocity of reconnected and non-reconnected lines. This image is taken from [Genestreti, Kistler, and Mouikis \(2012\)](#)

#### 4.2 MAGNETIC RECONNECTION IN THE MARTIAN SYSTEM

The key to reconnection lies in the finite magnitude of electrical resistivity and oppositely directed field lines. In the interplanetary medium, the stellar wind's magnetic field line can be oriented in any direction to the planet's magnetic field. These different inclinations produce different magnetic topology and each new magnetic structure that forms affects the wind and planetary ions adversely. A summary of the two different orientations that we took for our study is presented in [Russell \(2000 A\)](#) for the Earth's magnetosphere.

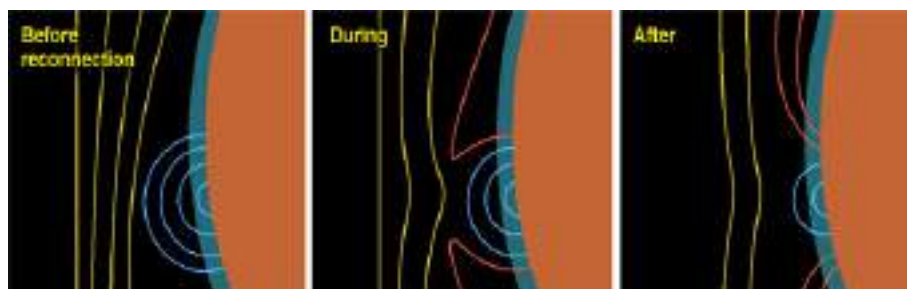


**Figure 11:** A cartoon sketch of 2D magnetic reconnection in Martian system. Here, the blue colour loops represents crustal field lines and yellow and red colour line are showing the IMF and open field lines (reconnected lines). This image is taken from [An article on NASA's MAVEN observations](#)

Here, we have modeled the Martian system, which is having a strong magnetic anomaly in its crust, unlike Earth's magnetic geometry. Due to the different scale sizes, the picture changes a little bit. [Figure 11](#) describes the journey of IMF in the vicinity of the planet and how their presence affects the martian crustal field. The magnetic field lines extending outward from the Sun by the solar wind (yellow color) are coming up against the field lines associated with pockets of magnetized Martian crust (blue). These two oppositely oriented field lines are reconnecting, so open field lines (red) are forming, which (may) easily allow the atmospheric escape. Another feature to notice here is the squeezing and subsid-ing of the crustal field lines due to this process.

### 4.3 3D MAGNETIC GEOMETRY

All the above diagrams are representing the reconnection process in two-dimensional geometry. However, when we make a transition from 2D to 3D, diverse modifications occur. The diffusion region does not remain bound to the 2D surface. The neutral points, which are basically the position where reconnection occurs, remain no more the single points. A plane of neutral points form in which the

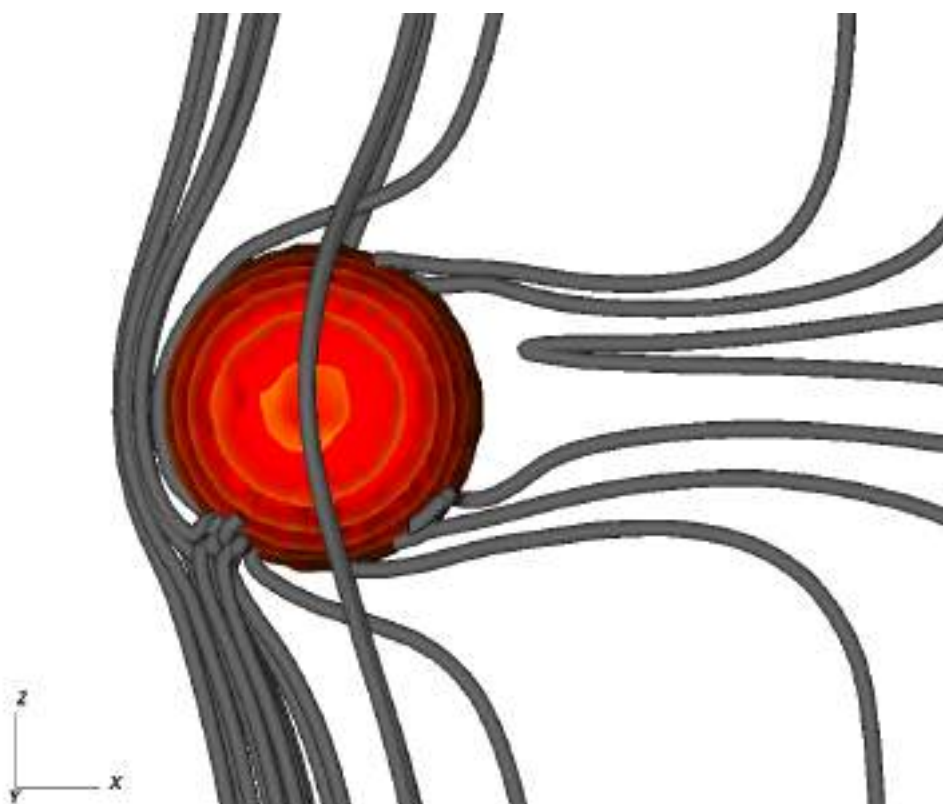


**Figure 12:** The above plot represent the magnetic streamlines for our [S-IMF](#) case. Red colour sphere stands for our modeled hypothetical planet, Mars and the grey colour bundles denotes the magnetic streamlines. The dayside magnetic reconnection can be easily noticed as a form of intertwined bundles. Open and draped field lines are also present in the system. The "U" shaped field line in the right side signifies the magnetotail region.

charged particles with high speed are moving in a particular direction. [Figure 12](#) has managed roughly to show this plane for our [S-IMF](#) case. It can be perceived as a 3D plane having its normal parallel to the dipole's position vector and passing through a common intersection of intertwined magnetic bundles in the dayside of Mars. [Figure 12](#) explains the hybrid magnetic topology of the Martain system. All three types of magnetic field topologies (grey color) exist in our model: open field lines, draped field lines, and close field lines. The closed field lines are present on the Sun-facing side of the planet. One draped field line, which is having its journey from negative to positive and again back to the negative y-axis, is shown above the surface of Mars (red color). Reconnected open field lines in the nightside of the planet is forming a magnetotail, where some field lines which do not have access to the planetary magnetic fields can be easily distinguished as a type of draped field line. A similar magnetic topology has been obtained by [Xu et al. \(2020\)](#), who mapped the magnetotail topology of Mars using a [MHD](#) model and [MAVEN](#) data.

Apart from the complex magnetic topology, in the 3D magnetofluid system, the dot product of the electric and magnetic field is not zero, i.e.,  $E \cdot B \neq 0$ . As a consequence, the current introduced in the system due to the gradient of the magnetic field is no more perpendicular to the magnetic field lines, unlike the case in 2D geometry. Here, the current can lie in any direction with respect to the magnetic field, where the major dynamics of the current sheet are governed by [Equation 3](#) and [Equation 4](#).

#### 4.4 SIMULATION RESULTS: MAGNETIC FIELD DEVIATION AND CURRENT SHEET

We have modeled three particular cases: one with no dipole case and the others in which mini-magnetosphere is present, but the direction of [IMF](#) is either oriented southward or northward, i.e.  $(0,0,-1)$  or  $(0,0,1)$ . In all the models, plasma distribution and magnetic field configuration evolve self-consistently. The steady-state configuration is identified by observing the global changes in magnetic field geometry and by analyzing a temporal evolution of kinetic, magnetic, and thermal energy. All the types of energy reached to their steady value in about 30 minutes. During this time interval, solar wind crosses the whole domain approximately only one time ( $\frac{125R_M}{270\text{km/s}} \sim 1570$  seconds  $\sim 26$  minutes). [Figure 13](#) shows the steady-state configuration of magnetic field geometry along with the pseudo-color plots of magnetic field deviation and current sheet for [S-IMF](#) and [ND](#) cases in the noon-midnight plane (sliced at  $y=0$ ). The modeled planet is the gray shaded area, and the small point of magenta color represents the location of the dipole in the [S-IMF](#) case. The analysis for the [N-IMF](#) case is presented in [Appendix E](#) as it has features similar to the [S-IMF](#) case. [Figure 13](#) should be read from the top down covering all the panels one by one i.e. from (a) to (b), (c) to (d) and (e) to (f).

[Figure 13a](#) and [Figure 13b](#) shows the magnitude distribution of magnetic field deviation for [S-IMF](#) and [ND](#) cases from the view of dawn/dusk side. The background splitting scheme allows us to separate the dipole magnetic field compo-

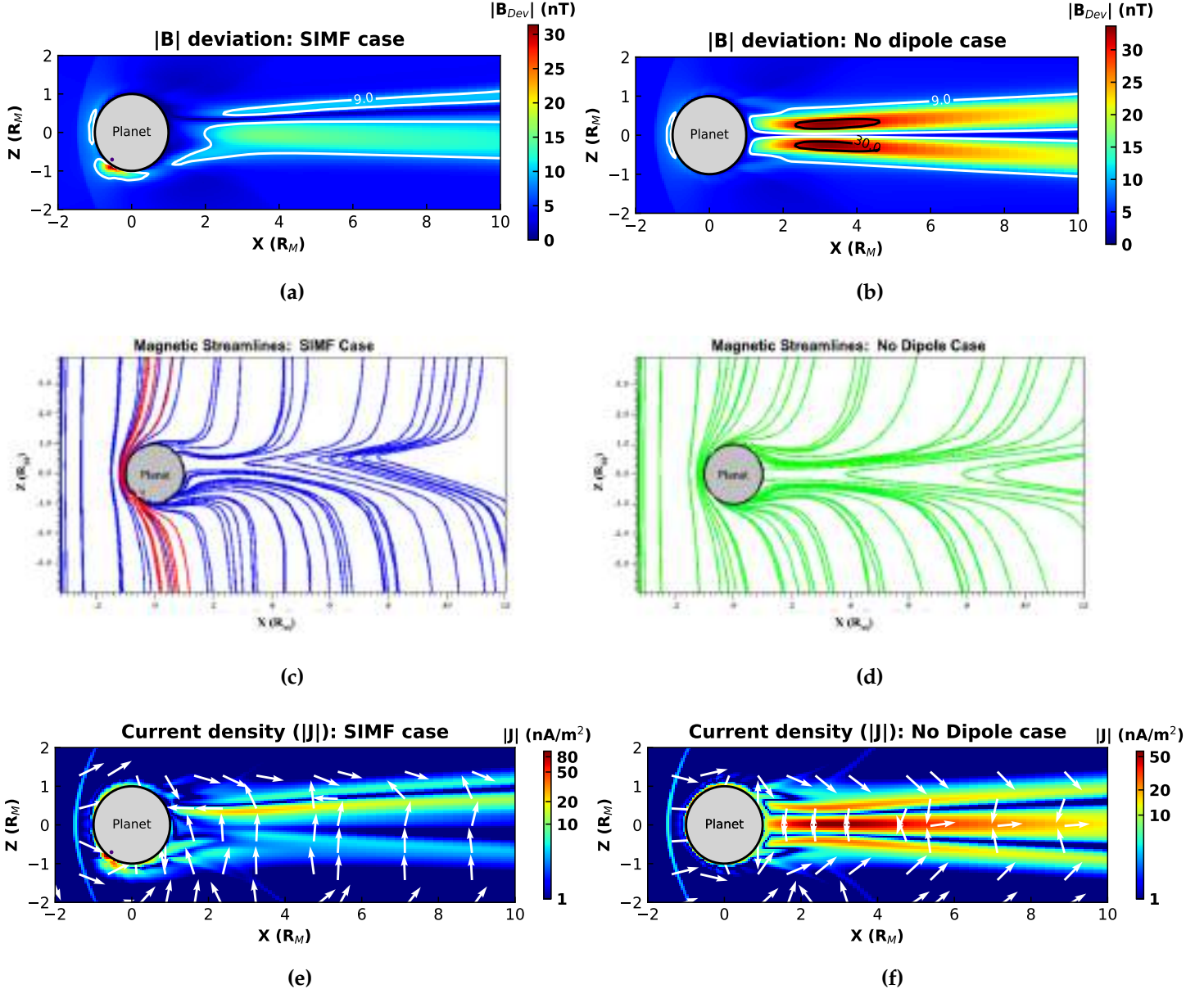


**Figure 13:** Pseudocolor plots of magnetic field deviation ((a),(b)) and current density ((e),(f)) in noon-midnight plane for both **S-IMF** and **ND** cases. Columns (c) and (d) represents magnetic streamlines plot for the above discussed cases.

ment in **S-IMF** (and **N-IMF**) cases, through which we are able to compare the effects of the intrinsic magnetic field directly. First, both the plots have a similar magnitude of magnetic deviation in the vicinity of the subsolar area (the region where the angle between the Sun and the local horizontal level is  $90^\circ$ ) is highlighted by a white contour line of 9 nT. Such low accumulation of field lines is because of the thin atmosphere, on which magnetic field draping depends ([Section 1.2.3](#)). The same contour line follows in the nightside of the planet, where the distinctive feature is the total amplitude of  $|B_{dev}|$  in **ND** case. In absence of intrinsic magnetic field, the  $|B_{dev}|$  reaches up to  $\sim 35$  nT as compared to the magnitude

of order  $\sim 20$  nT in **S-IMF** case. The reason for this attribute is the reconnection process. The planetary magnetic field lines in the **S-IMF** case reconnect with the **IMF**, thus releasing the magnetic energy and, therefore, decreasing the total magnetic strength. Whereas, having no chance of reconnection in **ND** case, field lines compressed to an extent such that they can balance the lost plasma pressure in the wake region with their increased magnetic pressure. This results in the two identical regions of magnetic strength (dark red) having field lines of opposite polarity. The cause of this unique trait is further discussed in [Appendix D](#). Apart from these properties, we observe a global asymmetry along with the localized strong  $|B_{dev}|$  in the dayside of **S-IMF** case.

The different magnetic field topology for the magnetized and unmagnetized Mars is presented in [Figure 13c](#) and [Figure 13d](#). The general features starting from the dayside to the nightside magnetotail is the draping of field lines. There are mainly two noticeable differences in the above plots. First is the presence of open field lines in the **S-IMF** case, which we have specifically red-colored for the Sun-facing side of the planet. The other one is the asymmetry in the field configuration for the **S-IMF** case. If we look closely, we will notice that in the magnetotail region, the nodal points of field lines (vertex of "V" shaped lines) are placed above the  $Z=0$  (imaginary) line. The reason for both the factors mentioned above is the mini-magnetosphere. The southern hemisphere located magnetic anomaly produces extra pressure in the  $Z < 0$  plane, resulting in an additional force in  $(0,0,1)$  direction. Unlike [Weber et al. \(2019\)](#), we do not find any closed field loops in the nightside of the planet because the planetary magnetic strength drops below the **IMF** strength.

The last panel of [Figure 13](#) exhibits amplitude of current density in log scale for both the cases in wind-**IMF** (XZ) plane. The magnitude of this electromagnetic variable in each direction is determined by taking the curl of  $B_{dev}$  components. As expected, the regions of a large magnetic gradient produce high current density. We found max. magnitude of  $|J|$  ( $\sim 80$  nA/m<sup>2</sup>) near the dipole's location. Whereas, complementing the [Figure 13a](#) and [Figure 13b](#), diverging strength of current density is observed in the magnetotail region. The plasma and neutral sheet can be explicitly identified in **ND** case. The most interesting features are the white arrows signifying the normalized  $J$ . As explained in [Russell \(2000 A\)](#), current crossing the plasma sheet are normal to wind's direction, and therefore, can accelerate plasma if  $B_z > 0$ . Compared to the symmetric flow of **ND** case, we observe an extending northward flow of plasma particles in **S-IMF** case. Furthermore, far from the planet ( $X \geq 4 R_M$ ), in the regions of maximum current density, the vectors in [Figure 13e](#) are oriented in partially negative X direction as compared to the positive X directed vectors of [Figure 13f](#). From the other definition of  $J = \rho v$ , we may have our first hint that the presence of a mini-magnetosphere is preventing the atmospheric escape from southern hemisphere by diverting the flow to the positive Z direction.

## 4.5 POLAR ANALYSIS

To get a better sense of how the magnetic field is varying and further understand its role in the above two cases, we did a polar analysis of components of magnetic field deviation in the same noon-midnight plane. We took three different elevations, as shown in Figure 14. The x-axis denotes the azimuthal angle in the XZ plane (sliced at  $y=0$ ).  $0^\circ$  stands for mid-night location, and going over the full circle, we covered the North pole ( $90^\circ$ ), Noon ( $1800^\circ$ ), South pole ( $90^\circ$ ) and traveled back to our original destination. For a better comparison, the y-axis range is kept the same for the same altitude, i.e., for each row. The same guidelines of Figure 13 are followed here to understand the underlying physics.

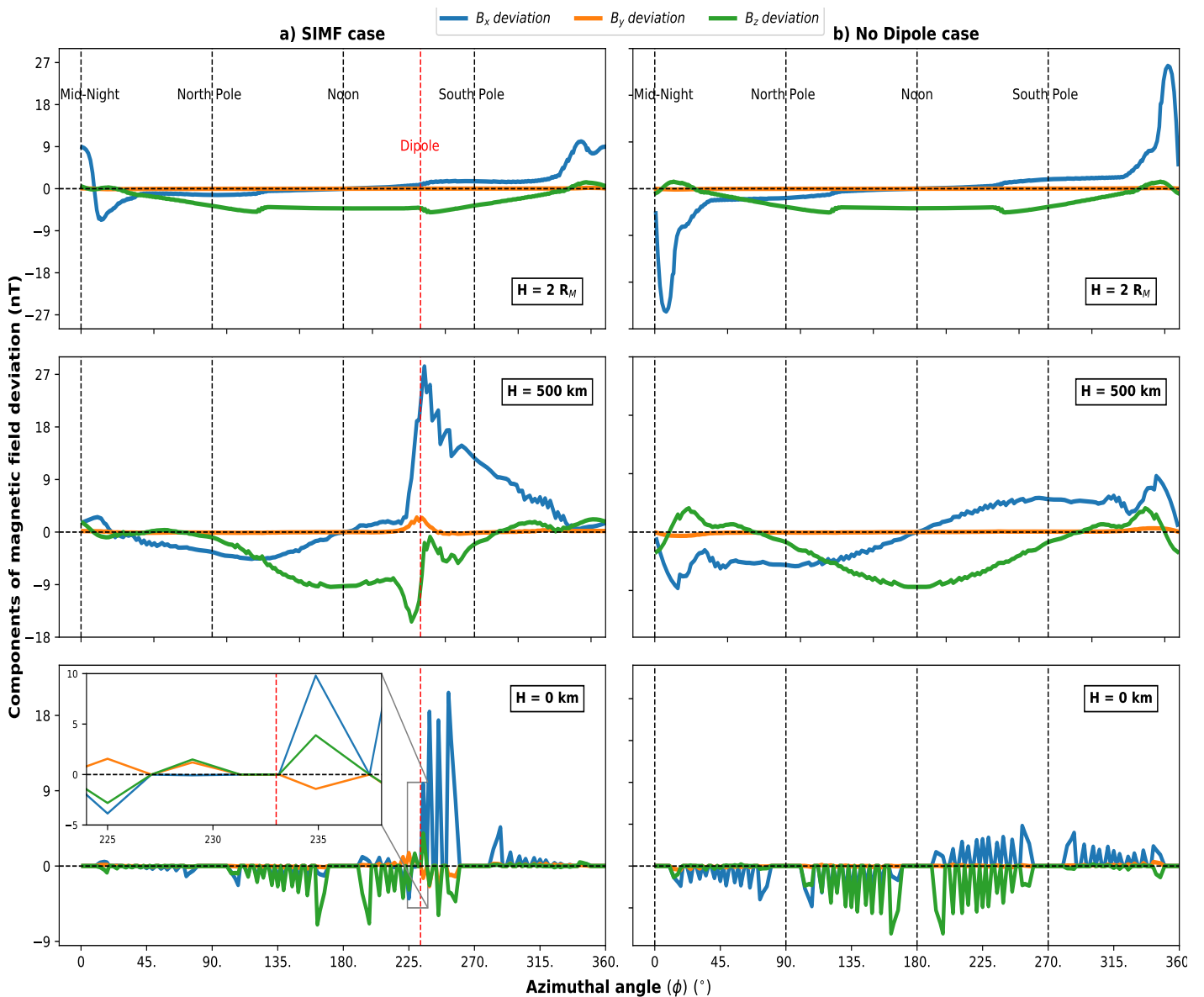


**Figure 14:** Polar analysis of magnetic field deviation components at different elevation in noon-midnight plane. The left and right column represent the data for S-IMF and ND cases respectively.

Let us begin by imagining a spacecraft embedded with a magnetometer such that it can read the magnetic fluctuations of the order of a few nTs. Suppose the spaceship is located at a distance of  $2 R_M$  from the mid-night position of Mars and can only travel in a circular path, which implies that its motion is restricted to 2D geometry. Thus, in the presence of the mini-magnetosphere, the magnetometer will read little fluctuations except in the range of  $\phi \in [300^\circ : 60^\circ]$ . Whereas, in the same region for the **ND** case, the magnetometer will read high fluctuations of about  $\pm 30$  nT due to reversal in sign of  $B_{x,\text{deviation}}$ . This is because of the oppositely directed draped field lines in the wake region. In both, the journeys magnetometer will not sense any significant differences near the dipole region because of the small scale size of the magnetic anomaly.

Moving closer to Mars ( $\sim 500$  km) and positioning our spacecraft again at the mid-night position, the magnetometer will observe an opposite polarity of  $B_{z,\text{deviation}}$  in **S-IMF** and **ND** cases. It is because the magnetic field lines emerging from the planet are oriented roughly in positive Z-direction. Then, from around the  $\phi \sim 120^\circ$ , fluctuations will start increasing in  $B_{x,\text{deviation}}$  and ultimately  $B_{x,\text{deviation}} > 0$  because of draping of field lines in the dayside of the planet. Apart from these variations, sudden increase, and decrease of  $B_{x,\text{deviation}}$  and  $B_{z,\text{deviation}}$  will be recorded near the dipole's location. This unique trait of the **S-IMF** case represents the role of the reconnection. It also implies that the scale of magnetic anomaly  $> 500$  km.

Finally, we have successfully landed our spacecraft on Martian soil. From this point, we will control our rover, which is also implanted with a magnetometer. The rover will walk over the Martian surface in a circular trajectory, initially positioning itself at the mid-night location. In the full course of its journey, the magnetometer will not read any significant fluctuations. However, close to the dipole's location, the magnetometer will register strong variations in the polarity of  $B_{x,\text{deviation}}$  and  $B_{y,\text{deviation}}$  but not of z-component. The reversal of two components of magnetic field deviation and not of the third one (inset plot in the last panel of [Figure 14](#)) is a key signature of magnetic reconnection. The similar signature is observed at real Mars [[Harada et al. \(2017\)](#)] signifying that crustal field reconnects with the **IMF**. From this analysis, we can confidently say that the effects of reconnection are extrapolated to the Martian surface. The exciting consequences of this discovery reside in the current and future Rover missions. Any high fluctuation in the magnetometer data along with the reversal in sign of magnetic field components will indicate the strong crustal field location. Thus, rigorously studying this area along with the changing local atmosphere, might reveal the role of the crustal field on the Martian atmosphere.

# 5

## PLASMA BOUNDARIES

---

The study of magnetized stellar wind interaction with any planet having a thin or thick atmosphere or a small or big scale magnetosphere is incomplete without a discussion of various plasma boundaries that separate various plasma regimes. A *BS* boundary separates the supersonic wind plasma from the subsonic magnetized gas, an *IMB*, or *MPB*, which separates the lighter elements of planetary ionosphere from magnetized plasma, an *Ion composition boundary (ICB)* which isolates heavier elements like CO<sub>2</sub> from close to stagnate plasma wind. Boundaries like magnetopause or mini-magnetopause are formed if a planet are blessed with a magnetic field. In the context of Mars, a good study on the difference between the former boundaries is performed by [Bößwetter et al. \(2004\)](#) and [Matsunaga et al. \(2017\)](#). For the current work, we have investigated the impact of mini-magnetosphere on *BS* and mini-magnetopause.

### 5.1 UNDERLYING PHYSICS OF Bow SHOCK

Bow Shock (*BS*) is the primary shield of the planet against a supersonic stellar wind. It gets its title from bow waves, the bent ridge of water in the face of a fast-moving boat produced by the force of the bow thrusting forward through the water. An interesting fact for a reader: bow waves holds a financial definition as well. However, here, we are going to talk about those discontinues which are present everywhere in space. *BS* was first discovered in the 1980s and 90s when several comets passed our space flying vehicles <sup>1</sup>. Though these *BSs* were broader and more gradual, the same physics was happening there, which occurs in the planetary medium. It is a result of supersonic magnetic stellar wind/cosmic radiation's inability to form a gradient around a solid obstacle. Several authors have explained the cause of *BS*, but we will primarily focus on the physical mechanism dictated by [Russell \(2000 A\)](#) for Earth's bow shock. As said above, the underlying physics is the same and therefore, can be applied to any system.

We take the help of [Figure 15](#) to elucidate the physics of *BS* formation. The pressure of any stellar wind is comprised of two parts: dynamic pressure and static pressure. Dynamic pressure, as the name suggests, is related to the momentum of particles. Mathematically, it is equal to the mass density times the speed squared ( $\sim \rho |v|^2$ ). The static pressure ( $\sim n k_B T$ ) with its misleading name is equal to the sum of thermal and magnetic pressure ( $\propto B^2$ ). The origin of the static pressure resides in the number density, temperature, and magnetic field of gas. When the wind approaches the planetary obstacle with a subsonic speed, its static pressure starts increasing (top panel of [Figure 15](#)). This happens because the compression wave is present in the system, which leads to an increase in

---

<sup>1</sup> [Bow Shock:Wikipedia](#)

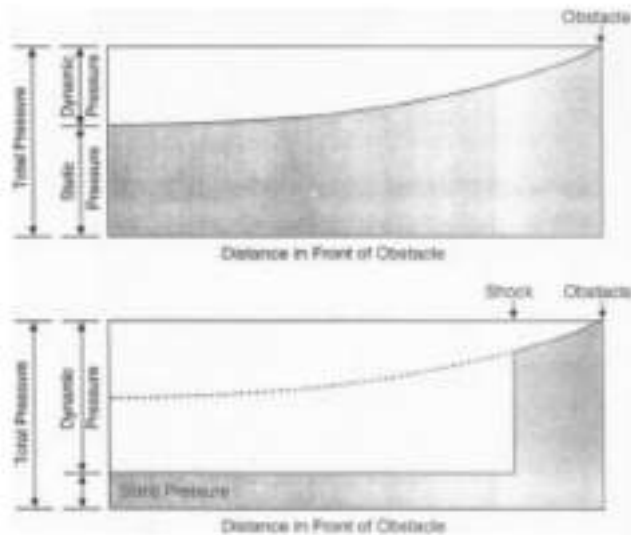


**Figure 15:** A qualitative sketch of pressure gradient leading to the formation of **BS**. In the top row, velocity of stellar wind is fast enough to produce a pressure profile required to do the deflection. In the lower row, pressure wave cannot move upstream and a shock is formed to do the deflection. This image is taken from [Russell \(2000 A\)](#).

temperature and number density around our solid body. As the total pressure remains constant, dynamic pressure starts decreasing. As a result, the wind's velocity decreases, which pilots the formation of a smooth gradient required to divert the flow around the obstacle. Whereas in supersonic flow, dynamic pressure hardly diminishes, as shown in the bottom panel of [Figure 15](#). Due to this, dynamic pressure always exceeds the static pressure, incapable of forming a smooth transition needed to deflect the flow. As a result, a shock front forms which compresses and heats the flow by converting the dynamic pressure into thermal pressure. This collisionless shock front (because the plasma is rarefied and hot) is shaped like a blunt bullet enclosing the planetary body and preventing it from the dangerous stellar wind.

Mathematically, **BS** forms because of [Equation 1](#). The mass-continuity equation takes care of fluid's compressibility by changing the density of plasma with dynamic velocity. Furthermore, from the above discussion, we can say the speed of plasma is the key for shock formation. Scientifically, we express this decisive condition in a physical variable called Mach Number ( $M$ ). This dimensionless parameter is the rate of the speed of the flow to the speed of sound in that medium. For supersonic flow,  $M > 1$ , and therefore, this condition must be met for shock formation. Also, for supersonic and isoentropic flow (where the entropy remains the same), the density of the medium changes faster than velocity by about a factor of  $M^2$ <sup>2</sup>. Apart from that, polytropic index, **IMF** direction, constituents of plasma, and their dynamic pressure affects the structure of **BS**. A good discussion on shocks formation and what factors affect their curvature is given in [[Introduction to Space Physics \(1995\)](#)]

<sup>2</sup> Role of Mach Number in compressible flows

## 5.2 SIMULATION RESULTS: BOW SHOCK

Before presenting the results, let's do a sanity check for [BS](#) requirement. The adiabatic speed of sound in ideal equation of state is given by

$$c_s = \sqrt{\frac{\gamma T}{K_B \mu}} \quad (14)$$

Putting model parameters in above equation, we get  $c_s \sim 16.7$  km/s. For the given  $v_{sw} = 270$  km/s, this speed of sound is negligible i.e  $M \gg 1$ . In solar system, magnetosonic mach number is more relevant as compared to normal mach number. The Magnetosonic Mach number ( $M_s$ ) is defined as

$$M_s = \frac{v_{sw}}{\sqrt{c_s^2 + v_A^2}} \quad (15)$$

where  $v_A$  is alfvénic velocity given by  $(B_{sw}^2 / \sqrt{\rho_{sw} \mu_0})$ . Calculating the alfvénic speed and putting it in above equation, we get  $M_s \sim 6$ . A similar order of magnetosonic mach number is observed at actual Mars [[Halekas et al. \(2017\)](#)]. Thus, from above theoretical calculations we can say that [BS](#) is formed in our study.

[Figure 16](#) presents the [BS](#) structure for [ND](#) case (green colour) in the noon-midnight plane sliced at  $y=0$ . The methodology we used to obtain this tangential discontinuity is  $\nabla \mathbf{v}_x$ . As the solar wind is  $x$ -directed, the transition from

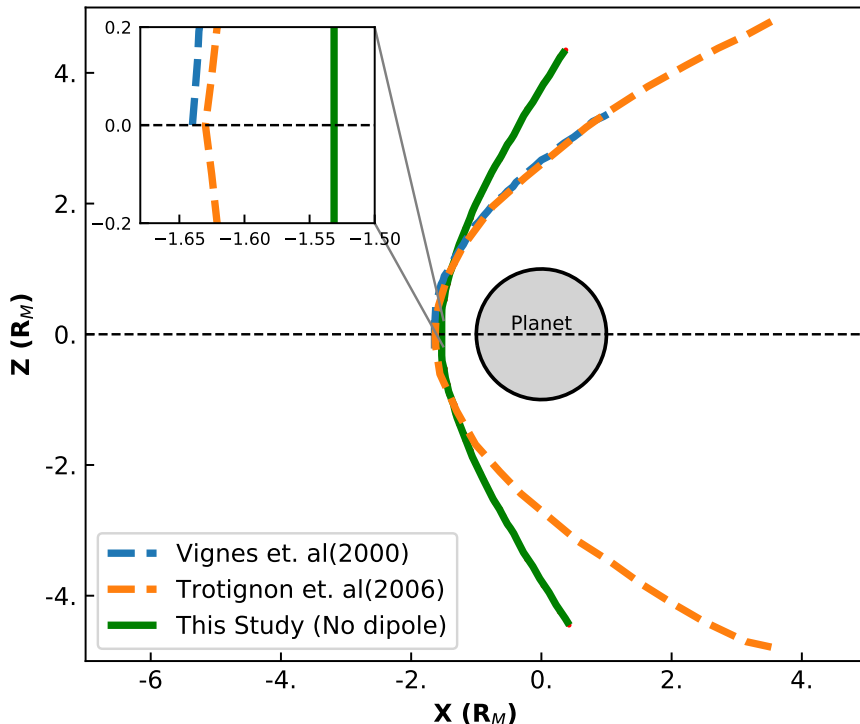


**Figure 16:** A contour line plot of [BS](#) structure in noon-midnight plane (sliced at  $y=0$ ) for the [ND](#) case. The modeled [BS](#) (green) is compared with [Vignes et al. \(2000\)](#)(blue-dashed) and [Trotignon et al. \(2006\)](#)(orange-dashed)

supersonic to subsonic magnetized gas across the **BS** is perfectly captured by a gradient of X component of wind's velocity. As the solar wind is x-directed, the transition from supersonic to subsonic magnetized gas across the **BS** is perfectly captured by a gradient of X component of wind's velocity. The value that we obtained for the subsolar location is  $1.52 R_M$ . This result closely matches with the analysis done by [Vignes et al. \(2000\)](#), who estimated the subsolar location of about  $1.64 R_M$  using the [MGS](#) data. Furthermore, [Trotignon et al. \(2006\)](#) found the similar distance ( $1.63 R_M$ ) by utilizing observations from both Phobos-2 and [MGS](#) mission. However, the plotted structure and terminator distance are quite different from the above two studies. We observed that **BS** is formed at a distance of roughly  $3.8 R_M$  above the North and South pole. Whereas, [Vignes et al. \(2000\)](#) and [Trotignon et al. \(2006\)](#) got the terminator distance of about  $2.62 R_M$  and  $2.63 R_M$ . The primary cause of our large terminator distance and high radius of curvature is [IMF](#) direction. In real Sun-Mars system, [IMF](#) is oriented in x-y plane having a parker spiral of angle  $56^\circ$  [[Halekas et al. \(2017\)](#)]. As a result, a mixture of quasi-perpendicular and quasi-parallel shock formed instead of an exactly perpendicular shock that has formed in our study. Mathematically, our [IMF](#), which is in the z-direction, is purely orthogonal to the shock normal (in the x-direction). Apart from this, the different dynamic pressure of plasma, solar wind contents, variable temperature, and [IMF](#) strength along with model limitations are some several other reasons for the above-mentioned features.

### 5.3 DOES INTRINSIC MAGNETIC FIELD AFFECT BOW SHOCK?

To investigate the effects of the mini-magnetosphere on **BS** structure, we compare the shock front formed in the [S-IMF](#) case with the [ND](#) case, which was described in the previous section. [Figure 17](#) presents the graph for both cases in the noon-midnight plane sliced at  $y=0$ . The dipole's location in the [S-IMF](#) case is sketched as a magenta dot. On a normal look, it seems that both **BSs** are tracing out the same path in the interplanetary medium. They both look identical, and also, the subsolar and terminator distance is the same for both of them. However, on a closer look, we will find there are indeed some differences in the two **BSs**. The two inset plots in [Figure 17](#) represent the same part of the northern and southern hemispheres. From there analysis, we observe that **BS** in [S-IMF](#) case (yellow) is located further away from planet than the **BS** in [ND](#) case (dashed red). Furthermore, this is happening notably and largely in  $Z < 0$  plane, which we have named "Southern hemisphere." It might be possible that the presence of an intrinsic magnetic field in the planetary crust is affecting the **BS** position. Physically this can happen because the mini-magnetosphere increases the size of the obstacle (planetary body) by providing additional magnetic pressure to counter solar wind ions. However, with the small scale-size of our mini-magnetosphere, it is not easy to consume this explanation.

To gain a better insight into the above-mentioned elusive feature, we calculated the difference between the position of **BSs** for each Z value. For example, from

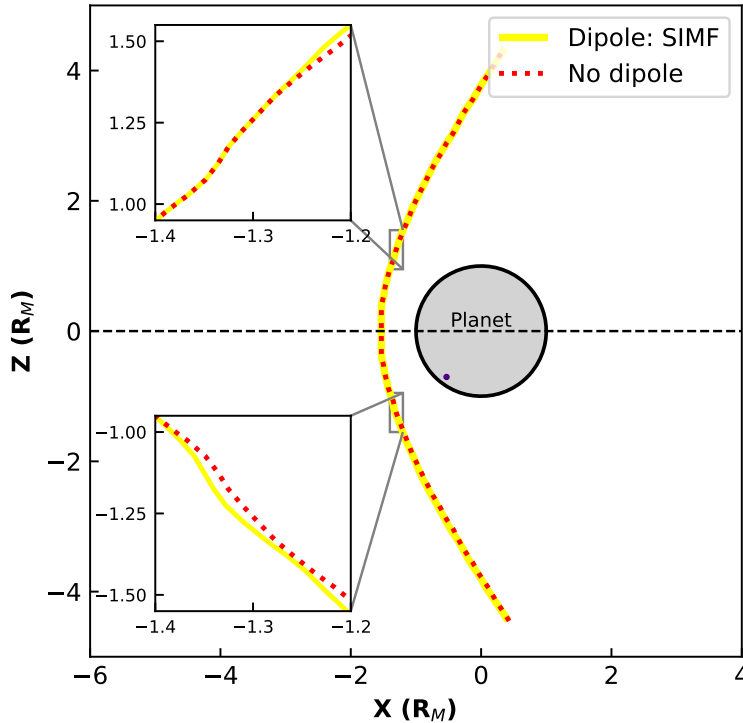


**Figure 17:** A contour line plot of BS structure for S-IMF (yellow) and ND (dashed red) cases respectively. The analysis is done in noon-midnight plane, where two inset plots are giving a closer look in a part of Northern ( $Z > 0$ ) and Southern Hemisphere  $Z < 0$ .

Figure 17, we get the index locations ( $x, y$ , and  $z$ ) for both BSs and then, we calculated their distance from origin at each angular position. Figure 18a provides a qualitative sketch of what difference we are talking about. For each  $z_0$  point, we estimated the difference between  $r_{S-IMF}$  (shown as  $|r_{1,z_0}|$ ) and  $r_{ND}$  (shown as  $|r_{2,z_0}|$ ) and plotted their variation in  $Z$  plane, i.e.  $\Delta r(z) = r_{S-IMF}(z) - r_{S-IMF}(z)$ . A caution point: Figure 18a does not state that no difference is found in the positive  $Z$ -plane. We have only provided that plot for a better qualitative understanding. Continuing from our previous statement, the said deviation is plotted in Figure 18b. The red, black and blue color steps signify  $\Delta r >$ ,  $<$  and  $= 0$  and  $Z >$  and  $< 0$  region is marked as Northern and Southern hemisphere. From the mentioned graph, we can easily notice that  $\Delta r > 0$  for most of the  $Z$ -plane except a few, which represents the BSs location in the nightside (as  $Z > 3.8 R_M$  (terminator distance)). This confirms our statement from the previous paragraph that BS in the presence of an intrinsic magnetic field is averagely located farther away from the shock surface in ND case. In addition, the frequency of non-zero variation is higher in the southern hemisphere than in the northern hemisphere. The maximum difference ( $\sim 0.4 R_M$ ) is found out in  $Z \in [-1.3 R_M : 1.1 R_M]$ , which is position at a similar angular location as the dipole is from the origin. This might suggest that the presence of a magnetic bubble in the Martian crust is the cause of the above dissimilarities. Edberg et al. (2008) examined the whole MGS data set in the pre-mapping mission phase and inferred that BS in the southern hemisphere is certainly pushed further outward by the strong crustal field. Fang et al. (2017) also reached to the same conclusion executed

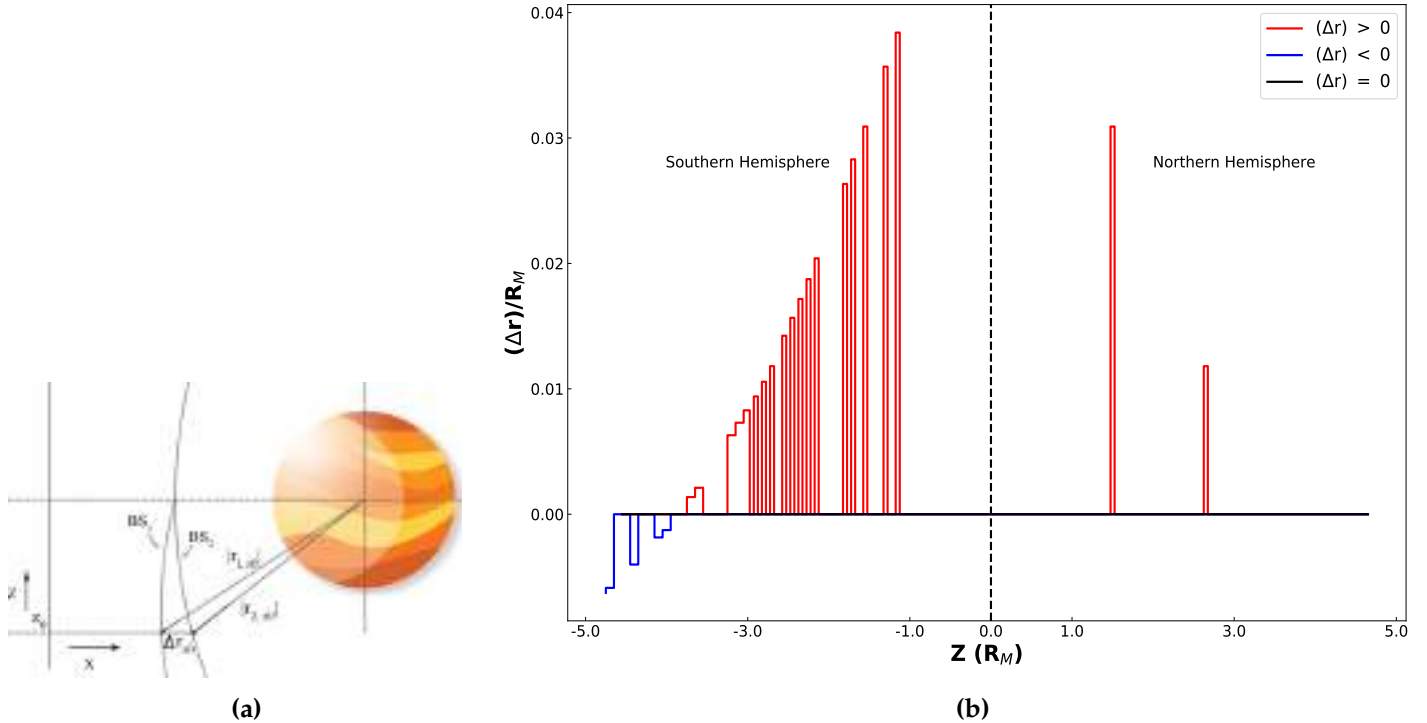


**Figure 18:** a) A qualitative sketch of  $\Delta r$  at point  $z_0$ . The planet is indicated as a solid colour body and the two BSs are drawn as a parabola.  $|r_{1,z_0}|$  and  $|r_{2,z_0}|$  represent their respective distance at point  $z_0$ . The  $\Delta r$  is calculated by subtracting latter from former and is denoted by  $\Delta r_{2,z_0}$ . b) A graphical representation of variation of estimated  $\Delta r/R_M$  with  $Z$  plane. Here, for each  $z$  value,  $\Delta r = r_{S-IMF} - r_{ND}$ . The red, black and blue colour steps signifies  $\Delta r >$ ,  $<$  and  $= 0$ .

numerical MHD simulations and later compared their results with MAVEN data. Li et al. (2020), who took a similar localized dipolar magnetic field like us, also observed an extension in BS location to higher altitudes towards the Sun. This is also favored by analysis that we did for S-IMF and N-IMF case (in Appendix E), in which we found no variation in their respective BSs locations.

However, none of the variations in Figure 18b is greater than  $0.05 R_M$ , which is our finest grid value. This might suggest that the above alterations that we are appreciating are due to computation errors, or the numerical mechanism that we implemented for identifying the BS structure has some faults. Halekas et al. (2017), who did a comprehensive study on structure, dynamics and seasonal variability of Mars-solar wind interaction using the Solar Wind Ion Analyzer (SWIA) on MAVEN spacecraft concluded that crustal field play secondary role in regulating the BS position. Thus, we can safely conclude that the mini-magnetosphere does not cause major distortions in the structure of Bow Shock (BS).

## 5.4 MAGNETIC PILE-UP REGION

The Magnetic Pile-up Region ([MPR](#)) is a region dominated by draped magnetic field lines and planetary ions ([Figure 7](#)). On the Sun-facing side, within the [MPR](#), the solar wind draped around Mars effectively. On the dark side of the planet, [MPR](#) is bounded by the magnetotail stretching far behind the planet. Magnetic Pileup Boundary ([MPB](#)), a thin, sharp discontinuity, separates the [MPR](#) from magnetosheath. In other words, [MPB](#) is a plasma boundary that deflect solar wind protons significantly but not the solar wind electrons nor the wind's magnetic field [[Nagy et al. \(2004\)](#)]. The [MPR](#) and [MPB](#) are also observed at Venus and comets, and empirical evidence suggest that they are common features in solar wind interaction with the atmosphere of unmagnetized (or weakly magnetized) planets.

After various space missions, [MPB](#) was first time undeniably identified by [MGS](#) mission [[Trotignon et al. \(2006\)](#)]. Before that, it was famous with the names of protonopause, planetopause, and Mantle. There are some definite signatures resides in plasma and thermodynamic variable which are exploited to identify its location and its nature. [Bertucci et al. \(2011\)](#) has summarised the characteristics of an inward crossing of [MPB](#) for Venus/Mars:

- Abrupt increase of magnetic field magnitude by a factor of 2-3.
- Strong reduction in magnetic field fluctuations
- Enhancement of magnetic field draping
- Decrease in solar wind ion (not electron) densities
- Decrease in temperature of solar wind electrons.

The above list roughly explains the signatures discovered in [MPB](#). However, in [MHD](#) one takes the help of a pressure balance condition to identify its position. Generally, the theory says that total pressure from the wind side must be balanced by pressure produce by a planet's atmosphere and magnetosphere. For weakly (or un-magnetized) planets, the ionospheric pressure of the planet counters the thermal pressure of wind, which abruptly increasing in the downstream regime of [BS](#). However, in our [ND](#) case, no such permanent boundary is formed. Before explaining the cause of this statement, let's do some needed calculations.

- Upstream solar wind dynamic pressure =  $\rho_{sw} |v_{sw}|^2 \sim 0.5 \text{ nPa}$  (using [Table 3](#))
- Magnetic pressure of planet =  $B_{tot}^2 / 2\mu_0 \sim 0.03 \text{ nPa}$  (using [Figure 13b](#))
- Thermal pressure of planet =  $n_{pl} K_B T \sim 0.01 \text{ nPa}$  ((using [Table 3](#)))

All the above estimations are with respect to the ambient medium. We can see that solar wind dynamic pressure is almost 10 times the sum of the planet's magnetic pressure and thermal pressure. One can argue that wind velocity near the

[MPB](#) is much lesser than the original upstream velocity. It is true, and for that, we observe a reduction factor of around 2.5 in wind's speed. However, after using that reduced magnitude of velocity, solar wind's dynamic pressure is about 1.6 times greater than the total pressure of the planet. It implies that we do not find any pressure balance state in our [ND](#) case. The cause for this misfortune is the planet's thin atmosphere and the constraints present in single-species [MHD](#) modeling. We took a thin atmosphere of about ten-thousandths of the actual atmospheric density due to which very minimal draping of the magnetic field occurs. The single-species does not allow us to separate solar wind plasma from planetary ions, and therefore, we cannot estimate the effect of  $n_{sw}$  near the [MPR](#). And at last, we kept the temperature constant over the complete run resulting in no conversion of wind's dynamic pressure to thermal pressure.

Although [MPB](#) is not present as a permanent member in our simulation, we estimated the subsolar position from where [MPR](#) begins in the dayside region. We accomplished this target by analyzing the characteristic signatures observed in [MPR](#) of the red planet.

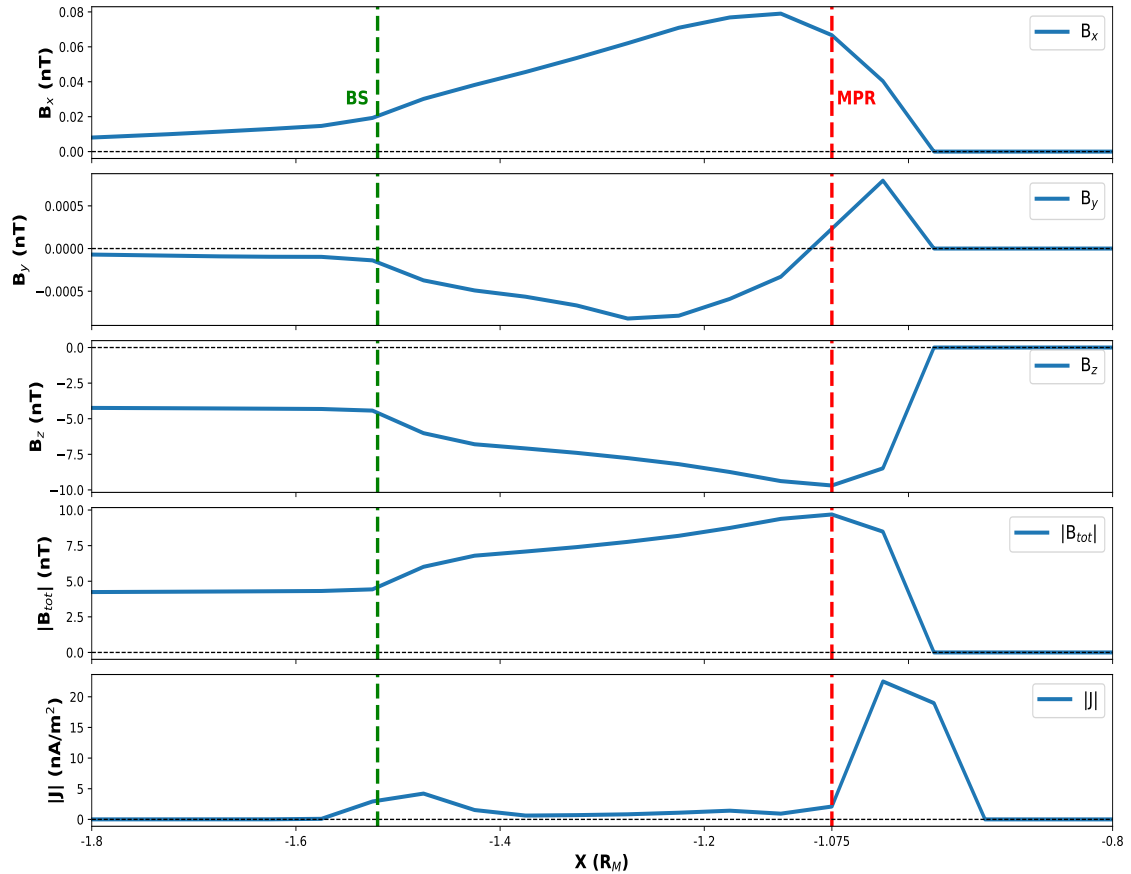


**Figure 19:** Variation of magnitude and orientation of magnetic field components at subsolar line in the top four panels. The last panel describes the fluctuations in magnitude of current density on Sun-Mars line.

The top four panels of [Figure 19](#) show the variation in magnitude and orientation of magnetic field components at the subsolar line for [ND](#) case. The [MPR](#) is marked as the steep decrease in magnetic field magnitude (fourth panel) along with the huge change in  $B_x$  component (first panel). These features are almost coinciding with the Fig 3.3 of [Nagy et al. \(2004\)](#), who presented the magnitude and orientation of magnetic field vectors during the closest third elliptical orbit of Phobos-2. The author took the results of [Riedler et al. \(1989\)](#) and converted the azimuth and elevation of magnetic field in areocentric orbit to three cartesian components of the magnetic field in Mars-centered Solar Orbital ([MSO](#)) coordinate system. For instance, our X, Y, and Z-axis represent -X, Z, and Y-axis of [MSO](#). Thus, if we make an analogy, our first and fourth panel shows similar characteristics with their respective panels. Furthermore, if we take into account the conversion chart of two different coordinate systems, we will find that the sudden increase in  $B_z$  component is also an important feature in tracing [MPR](#). Apart from these similarities, fluctuations in current density (last panel) is also exhibiting the identical traits as of reported by [Nagy et al. \(2004\)](#). The subsolar distance ( $\sim 1.075 R_M$ ) from which magnetic field draping starts is highlighted by red color dashed line. Calling this transition a beginning point of [MPR](#) and not [MPB](#) has a reason. It is true that the above features match with the [MPB](#) signatures. However, not having the pressure balance boundary is stopping us from calling it a [MPB](#).

## 5.5 MINI-MAGNETOPAUSE

The magnetopause is an abrupt plasma boundary commonly found in stellar wind interaction with a magnetosphere of magnetized bodies, like, Earth. Within the dayside, it is observed as a bullet-shaped front ([Figure 2](#)) enclosing and preventing the Earth from the intense solar wind. This boundary, like [BS](#), [MPB](#) are the large-scale signatures of an obstacle to the solar wind flow. They can, therefore, be used to learn about the nature of the obstacle and its sensitivity to variations of the upstream interplanetary plasma and its embedded magnetic field. Thus, determining their structure has become an essential part of [SPI](#).

In order to determine the scale size of the magnetosphere, we need to solve the complex non-linear equations (which is laborious!). However, we can qualitatively determine it by estimating the location of the magnetopause nose. For that, we only need to couple some variables based on a universal law. Conservation of momentum of magnetized plasma gas flowing through a stream tube of varying cross-section ( $S$ ) gives us:

$$(\rho_{sw} u_{sw}^2 + n_{sw} k_B T + B_{sw}^2 / 2\mu_0)S = \text{constant}$$

where the subscript 'sw' stands for stellar wind. For magnetized gas constantly flowing from the Sun, the second and third term in the above equation is negligible as compared to the first term. That is, solar wind's thermal and magnetic pressure can be neglected in comparison to its dynamic pressure because Magnetosonic Mach number  $> 1$  [[Russell \(2000 B\)](#)]. This incoming solar wind pressure

is (not always) countered by pressure originating from the planet's ionosphere and magnetosphere. In the case of magnetized planets, magnetic pressure dominates the ionospheric pressure. However, for weakly magnetized planets (like Mars), both ionospheric and magnetic pressure takes part in stagnating the solar wind flow. Thus, from the above statements, the necessary condition to determine the magnetopause structure is:

$$\begin{aligned} (\rho_{sw} u_{sw}^2 + n_{sw} K_B T + B_{sw}^2 / 2\mu_0) S &= n_{pl} K_B T + B_{pl}^2 / 2\mu_0 S \\ \sim \rho_{sw} u_{sw}^2 &= n_{pl} K_B T + B_{pl}^2 / 2\mu_0 \end{aligned} \quad (16)$$

where  $pl$  stands for the planet. In our study, due to the thin atmosphere, the first term on R.H.S of [Equation 16](#) is negligible as compared to the second term. Thus, roughly the magnetic pressure of the planet is balancing the upstream solar wind's pressure. In [Section 3.5](#), on a theoretical basis, we calculated the minimum strength of the magnetic field needed to stagnate the wind particles. The estimated value was 35 nT and is also shown as a black contour line in pseudocolor plots of total magnetic strength (dipole + deviation) for both **S-IMF** ([Figure 20a](#)) and **N-IMF** cases ([Figure 20b](#)).

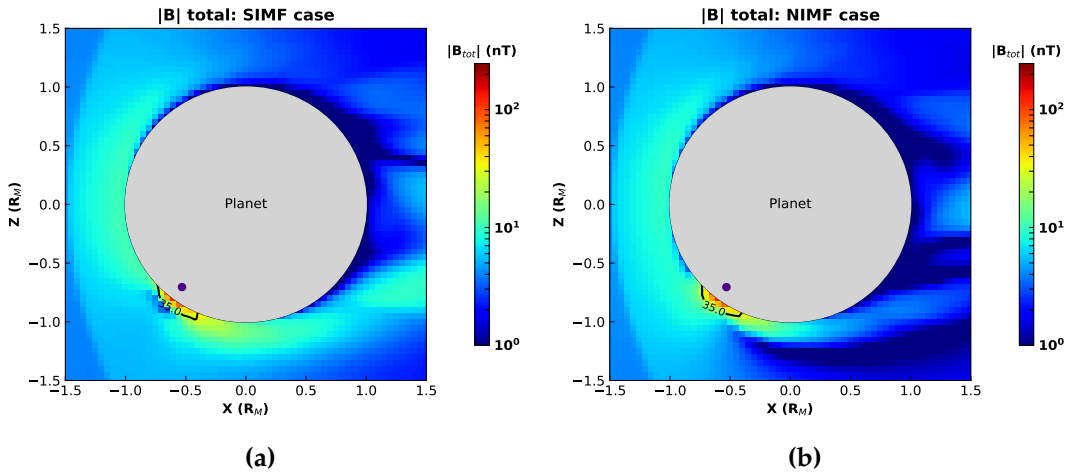


**Figure 20:** A pseudocolor plot of total magnetic strength in noon-midnight plane for a) S-IMF and b) N-IMF case. The magenta dot stands for dipole's position and critical value of magnetic field ( $\sim 35$  nT) is shown as a black contour line.

The 35 nT contour line is very localized and is only stretched to a few Kms above the Martian surface. Also, none of the regions other than the dipolar area have magnetic intensity greater than this value. This implies that the magnetopause that has formed is very restricted, and is extending only up to a few kms above the surface. Hence, the name "mini-magnetopause".

[Figure 21](#) presents the structure of mini-magnetopause for both  $\pm z$  IMF direction. The graph is plotted in the wind-IMF plane (XZ plane) sliced at  $y=0$ . The localized geometry of this pressure boundary for both **S-IMF** and **N-IMF** cases is obtained by equating wind's dynamic pressure and the planet's total pressure (magnetic + ionospheric pressure). Therefore, the red (**S-IMF**) and blue

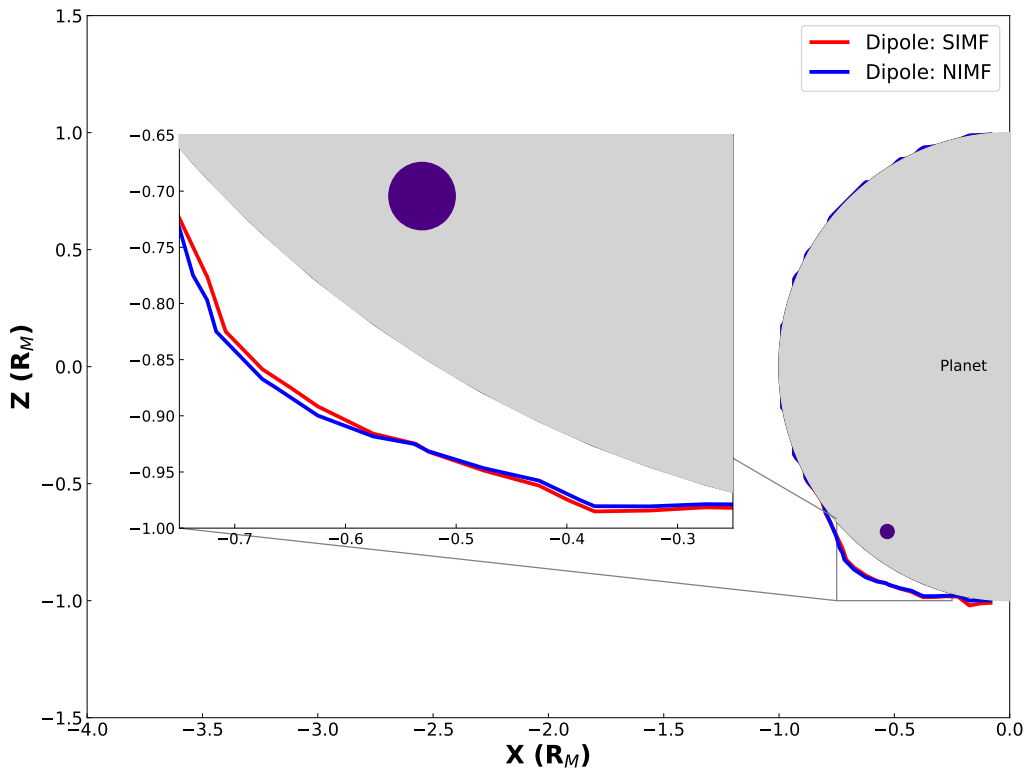


**Figure 21:** A contour plot of mini-magnetopause structure for both **S-IMF** and **N-IMF** studies in wind-IMF plane. Magenta dot denotes the dipole's position and inset plot is included for a detail view.

(**N-IMF**) colour line is a contour of value  $\sigma$ . From a broad perspective, both mini-magnetopauses are formed in the neighborhood of the dipole (magenta dot). They are also lying on top of each other. However, on a closer look, we will find that there is some difference in their trajectory. For instance, the nose of **S-IMF** directed mini-magnetopause is located at  $\sim 1.085 R_M$  above the planetary soil. Whereas, the same nose in the northward directed **IMF** is found at an elevation of  $\sim 1.1 R_M$ . Apart from this, in the vicinity of the angular position of the dipole (i.e., in  $[42^\circ:60^\circ]$  sector), the **N-IMF** directed mini-magnetopause is located farther away than **S-IMF** directed mini-magnetopause. However, in the exterior set of this region (i.e.  $\theta \notin [42^\circ:60^\circ]$ ), table turns and we found that **S-IMF** directed mini-magnetopause is positioned at a larger distance than the mini-magnetopause in **N-IMF** case. The physical reason for this exciting result resides in magnetic reconnection.

As explained in [Chapter 4](#), magnetic reconnection is favored when two field lines are oppositely directed to each other. In our study, the crustal field lines are in  $XZ$  plane where they have a positive  $z$ -component in an angular position of  $[42^\circ:60^\circ]$  ([Figure 9](#)). Thus, southward directed wind's magnetic field lines reconnect easily and efficiently than northward-directed **IMF**. Because of this, more magnetic energy is released from the former case. Furthermore, crustal loops are

pushed down in the interior due to relative solar wind higher pressure. However, outside the sector, as mentioned above, the crustal field lines have a low-value component in the negative Z-axis. We can visualize them as the field lines coming out from the north pole of the magnet ( $-ve$  z component) and going into the south pole of the magnet (again  $-ve$  z component) (Figure 9). Thus due to the reversal of crustal field z-component in these regions, **S-IMF** reconnects less effectively than **N-IMF**. As a result, **S-IMF** directed mini-magnetopause is found at a higher distance than **N-IMF**'s mini-magnetopause. This feature is common in Earth's magnetosphere and is famous with the name of "magnetopause erosion" [Pudovkin, Besser, and Zaitseva (1998)]. It has been witnessed that during the periods of southward-**IMF**, magnetopause displaces toward Earth's surface due to depression of the magnetic field in the magnetosphere. The happening of the same process at Mars implies that similar physical processes must be happening near the Martian crustal field. But, does it also imply that those mechanisms are producing the same effect on plasma and atmospheric environment of Mars?

The formation of mini-magnetopause is also supported by Harnett and Winglee (2003), who observed that structure like a magnetopause is formed in the southern hemisphere instead of **MPB** if strong southern magnetic anomalies are present in the planet's crust. As stated in the Section 2.3, the asymmetry found in **MPB** due to the crustal magnetic field is the same as the formation of mini-magnetopause because both boundaries show similar plasma signatures. Thus, we observed asymmetry in the **MPB** and can certainly say that this plasma boundary pushes to higher altitudes toward the sun. If we consider the starting location of **MPR** as **MPB**, then we can crudely say that **MPB** rises about 100 km above the surface at the location of the strong crustal field. These results qualitatively match with the authors, Li et al. (2020), Edberg et al. (2008), Fang et al. (2017) who found out that **MPB** extends to higher altitudes in the southern hemisphere where strong crustal field is located. However, the extension in our model is small compared to their results. It is because we took a dipolar magnetic field of low strength, which is, if compared, is about one-tenth of observed crustal strength at 100 km altitude (Section 3.5).

# 6

## ATMOSPHERIC EROSION

---

The solar system has great examples of planetary bodies with very different atmospheres, including Mars with a thin CO<sub>2</sub> rich atmosphere, Venus with a thick CO<sub>2</sub> rich atmosphere, or Earth with a N<sub>2</sub>/O<sub>2</sub> atmosphere. These terrestrial planets reserved their atmospheres primarily through accretion of volatile elements during their accretion phase [Gronoff et al. (2020)], and secondarily through volcanic emissions and tectonic activities. During their accretion phase, they acquired their most stable state depending upon their density and gravity, and are now placed in the configuration that we see today. Despite having different distances from their common host star (Sun), a natural question arises. A question of why these rocky planets have a different atmosphere? What are the causes of their distinct atmospheric evolution? If they are formed from the same underlying principle, why do they have dissimilar atmospheric composition? What is their current escape rate, and how is it different from their past atmospheric loss? On an average human timescale, we think of an atmosphere as ineradicable as a planet's rocks. However, over a geological time scale, molecules can leak from the top of an ionosphere and escape to never-ending space. In the last few years, we have recognized how the very existence of an atmosphere depends as much on escape as supply. In particular, the climate on terrestrial planets and on their natural satellites are like the remnants of medieval castles that have been subject to histories of plunder and decay. Atmospheres of small-size planets are more like crude forts, poorly contended, and exposed. For decades scientists have pondered how the tininess of the red planet might be responsible for an atmospheric density only one hundredth as Earth's—but thought of escape makes us curious why Mars has any atmosphere at all. Odd riddles also exist for the nearby terrestrial planet. How did Venus adhere to a thick atmosphere yet entirely lose its water?

### 6.1 ESCAPE PROCESSES

The quest to discover the justifiable, falsifiable answers to the above questions resides in the study of different escape mechanisms. The escape processes are usually classified into thermal and non-thermal processes. For the former, the energy of a host star is primarily absorbed and converted to thermal energy. This may result in the substantial ejection amounts of ions in the upper atmosphere due to an increase in their thermal velocity. Here, we will describe the common escape process observed for the red planet and then briefly state the overall effect of the intrinsic magnetic field on those mechanisms. A cartoon sketch of below-mentioned escape mechanisms is shown in [Figure 22](#)

- **Jeans escape:** The high energy atoms present in the tail of Maxwell velocity distribution can exceed the escape velocity by absorbing solar Extreme Ul-

traviolet (EUV) radiation. The continuously changing martian crustal field can accelerate the ejection through joule heating by producing induce electric currents in the upper ionosphere. *However, the effects of this magnetic field is negligible under nominal solar conditions.* [Lillis et al. (2015)]

- **Photochemical Escape:** The incoming solar wind electrons excite the neutral molecules (like O<sub>2</sub>) at near and above the exobase. This produces a chain of exothermic reactions that provide the ion products needed the energy to escape from the martian gravitation grip. *This dominant non-thermal process is less likely affected by martian intrinsic field* [Gronoff et al. (2020)].

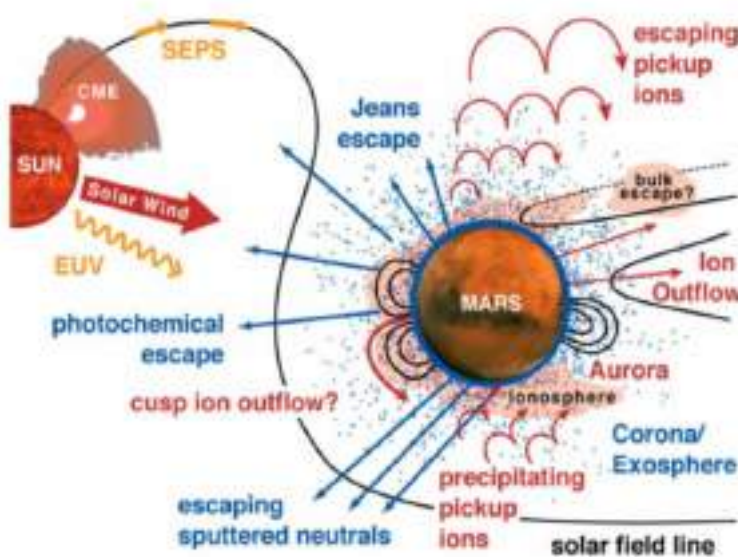


**Figure 22:** A cartoon sketch of different escape mechanisms operating on Martian atmosphere. This image is taken from R. Lillis oral presentation at 52nd eslab symposium.

- **Bulk Ion Escape:** As explained in [Section 1.3](#), it refers to the removal of large amounts of ionospheric plasma through the formation of magnetic flux ropes ([Figure 5](#)). *The martian magnetic bubbles don't exactly inhibit/accelerate this effect as it depends on the extension of crustal field and planetary ionosphere.*
- **Ion pickup and Sputtering escape:** The planetary ions that get trap on [IMF](#) are called pick up ions. If these pick up ions found themselves magnetically connected to solar wind (especially in the regions of high velocity), the  $E = v_{sw} \times B_{sw}$  line of force can accelerate particles away from a planet as well as towards a planet. The planetary ions that are energized towards the planet can deposit their escape energy to cold ions through collision or wave mechanism resulting in a sputtering loss of atmosphere. Whereas, the atmospheric ions that gained momentum in the direction away from the planet are lost in deep space, and we called this process pickup ion escape or plume outflow. *The intrinsic magnetic field overall inhibits both the process by reducing ionization of heavy molecules (O<sub>2</sub>) and by trapping them in their close loops which do not reconnects with IMF.* [Dong et al. (2017)]

- **Ion Outflow:** Similar to bulk ion escape, this process was explained in [Section 1.3](#). The planetary ions on magnetotail are accelerated to escape energy on the virtue of gradient in magnetic field pressure ([Figure 4](#)). *There is no direct evidence that an intrinsic magnetic field acts as a shield. However, it might be possible that they would deteriorate the case by providing momentum and energy to planetary ions.*

## 6.2 CONSEQUENCES OF LOCATION OF MINI-MAGNETOSPHERE

At the end of the previous section, we stated why the role of the magnetic field is not evidently determined in the ion outflow. In addition, the inhomogeneous distribution of the Martian crustal magnetic field makes this study even more difficult. To investigate the effects of the planetary magnetic field on atmospheric loss separately, we need a particular field geometry that only spreads to a minimal region like our mini-magnetosphere. Also, we need to minimize the effects of the ionosphere to understand the underlying physics clearly. For instance, if we take a thick atmosphere, then it is highly possible that [MPB](#) extends even to a larger size than the scale of mini-magnetosphere and, therefore, the effects of a planetary magnetic field are minimized. Thus, we take a thin atmosphere to reduce the influence of planetary ions. We only investigated the ion outflow mechanism in our study where from ion, we mean hydrogen ion. The reason is we kept the Hall MHD term off because of which we were not able to account for the Bulk Ion escape. However, we observe the formation of plasmids (or magnetic flux ropes) near the reconnection site. And also, we employed a single-species model for our work. This means that we cannot exclusively study the effect of the solar wind convection electric field, which is needed to understand the outcomes of the pick-up ion and sputtering process.

We studied the atmospheric mass loss from a localized equal part of the northern and southern hemisphere using the two independent passive scalars described in [Section 3.6.3](#). These colored fluids are initially normalized to unity, and then, they evolved by virtue of inhomogeneous advection equation. In simple words, their flow is governed by solar wind's velocity vectors, subsequently following the path of (more or less) [IMF](#). Thus, we can say that the atmospheric erosion that we have observed is portraying the ion outflow mechanism. [Figure 23a](#) and [Figure 23b](#) shows the temporal evolution of localized mass-loss rate from all three axis for the [S-IMF](#) case. The abbreviations SH and NH stand for Southern and Northern Hemisphere. To evaluate the loss rate first, we take a cube of dimension  $8.0 R_M$  (extending from  $-4.0 R_M$  to  $+4.0 R_M$  in all three directions) with its center coinciding with the origin of grid configuration. The box being greater than  $3 R_M$  on each side encompasses the planet and its atmosphere. Then for each hemisphere, we calculated net flux passing through each surface of the cube using its respective passive scalar. This gave us the localized atmospheric escape from all six faces of the cube for that respective hemisphere. The same methodology is repeated for other hemispheres. The first observation

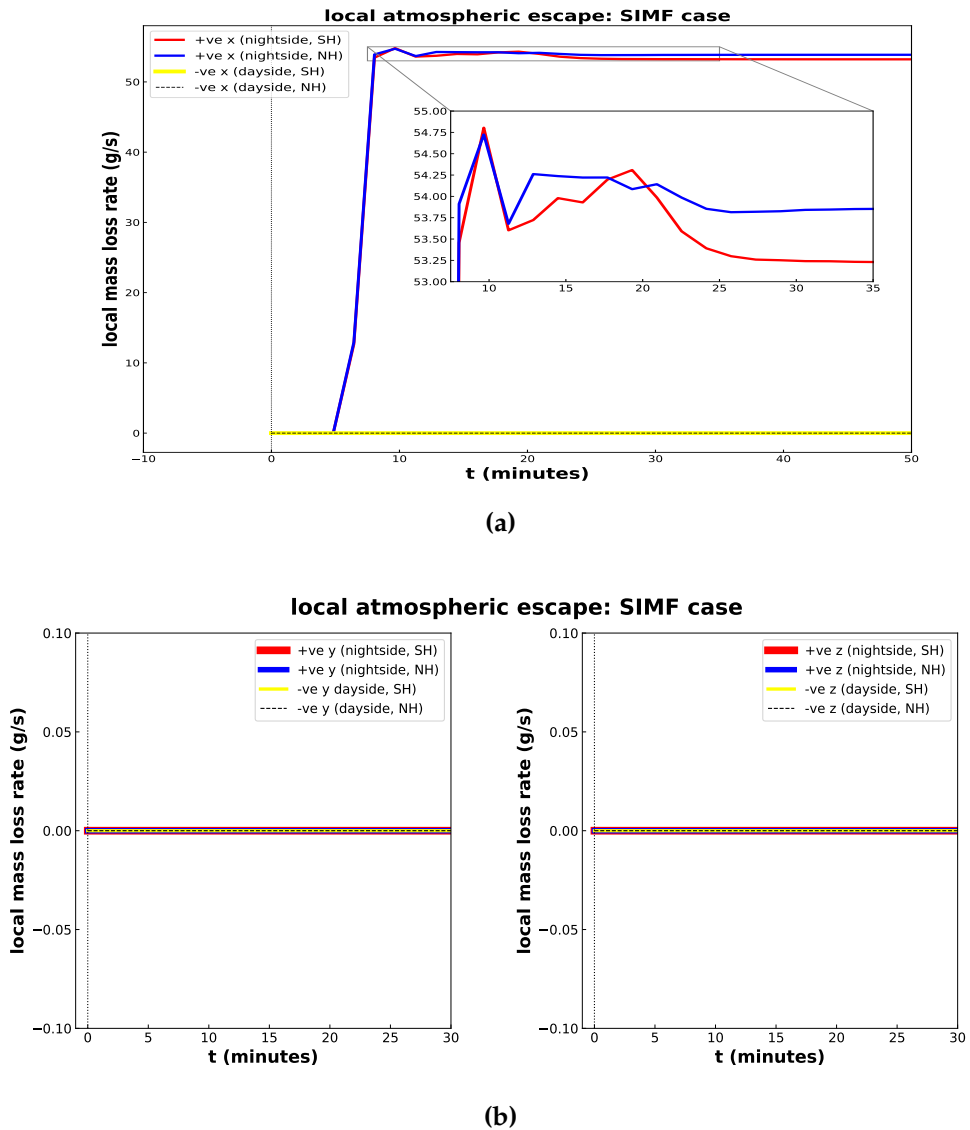


**Figure 23:** a) Local atmospheric mass loss rate from southern hemisphere (SH) and northern hemisphere (NH) in a) x- axis b) y- axis (left) and z- axis (right). A cubic box with length extending from  $-4 R_M$  to  $+ 4 R_M$  in all three directions is considered for the mass-loss rate calculation. The box encompasses the planet and its atmosphere.

is very straightforward, i.e. localized mass-loss rate from the dayside and nightside of y-axis ([Figure 23b \(left\)](#)) and z-axis ([Figure 23b \(right\)](#)) is almost zero. This result was expected because the solar wind is directed in the x-axis, and the planetary ions are escaping through IMF and open field lines, which are roughly perpendicular to YZ plane (i.e.. in x-axis). We could have obtained the loss in XZ plane (sliced at  $y = \pm 4R_M$  or XY plane (sliced at  $z = \pm 4R_M$ ) if we have colored our whole atmosphere or if it is possible to take account of solar wind electric field or Hall MHD. As none of the schemes are present in our current code, thus, we observed no significant atmospheric erosion from the noon-midnight plane and the equatorial plane.

[Figure 23a](#) shows the local mass-loss rate from dayside and nightside of the x-axis (YZ plane sliced at  $x \pm 4 R_M$ ) for both southern (SH) and northern hemisphere (NH). The local characteristics show that atmospheric escape in the magnetotail from both the hemisphere rises sharply around  $t \sim 5$  minutes and reaches their peak around  $t \sim 10$  minutes, where the solar wind takes about 6 minutes to reach the same location. Then, after passing through the transient state, local atmospheric erosion reaches a steady-state value of about 53.25 g/s for SH and 53.85 g/s for NH. Thus, we observed higher atmospheric loss from NH than SH, with a difference in the value of  $\sim 0.6$  g/s. We cannot neglect this value because we only represent a part of the atmosphere, the atmosphere which is very thin as compared to actual observations. These results qualitatively match with [Ramatstod et al. \(2016\)](#), who estimated the escape rate from SH of about  $\sim 46\%$  of total escape rate as compared to our  $\sim 49.5\%$ . However, the error bar is too high in their study. The only reason that is possible for this dissimilarity is the presence of a strong, localized mini-magnetosphere buried in the SH of the planet. There are at least three distinct means to understand this behavior.

- The first way of explaining this phenomenon is the formation of mini-magnetopause in only SH ([Figure 21](#)). Within this framework, we observed that the magnetic anomaly augments total pressure in a part of SH. Therefore, it can stand off the incident solar wind at higher altitudes. As a result, a reduced density of the atmospheric fluid is exposed to the solar wind.
- The second way of explaining this reduce mass-loss from SH is a direct appeal to magnetic connectivity. In [Figure 12](#), we discovered some close field lines loop coming out from the planetary surface in SH. The presence of these magnetic bubbles signifies the reduced magnetic connectivity of atmospheric particles with the solar wind plasma and has favored reduced ion outflow from the southern region.
- In [Figure 13e](#), we noticed that planetary ions from  $-ve$  z-plane is moving towards  $+ve$  z-plane and are mixing with the planetary plasma coming out from the dayside region of NH. Furthermore, the x-component of electric field ( $E = \eta J$ ) has higher value in nightside region of NH, than SH. This implies that a higher density of planetary ions is accelerated in the current sheet of nightside NH than the magnetotail in SH. As a result, 1.1 % of higher atmospheric mass loss is witnessed from the Northern hemisphere.

In summary, the mini-magnetosphere is showing the overall effects of the prevention of atmospheric loss by standing off the solar wind as well as by controlling the trajectories of planetary ions. This also suggests that the presence of an intrinsic magnetic field in planetary volume prevents atmospheric erosion.

To do a sanity check of conservation of mass flux, we calculated the sum of atmospheric mass-loss rate from SH and NH. We plotted their temporal variation for different sizes of boxes. [Figure 24](#) shows the escape rate from a cube with an edge  $8 R_M$  (red line with circles),  $12 R_M$  (blue line with triangles) and  $24 R_M$  (green line with squares). The center of the cube matches with the center of the

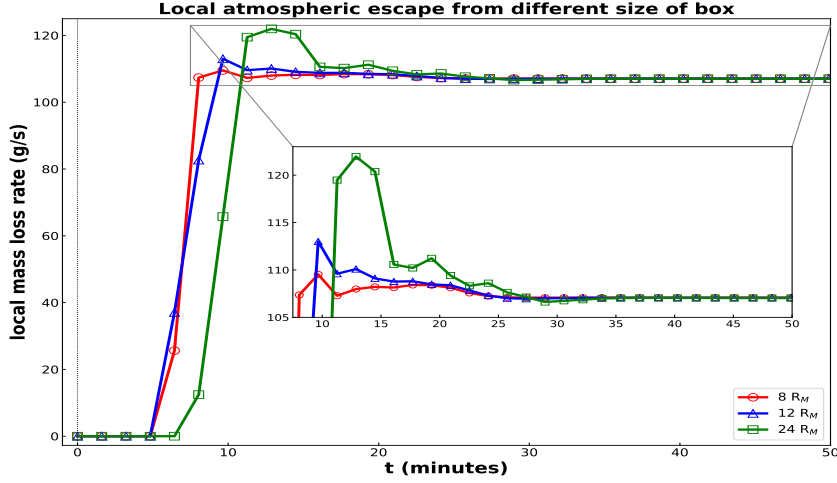


**Figure 24:** Temporal evolution of localized atmospheric mass-loss rate from a cube of edge (a)  $8 R_M$ , (b)  $12 R_M$ , and (c)  $24 R_M$  with its center coinciding with the center of the planet. All three curves are found to converge slowly to a steady-state value with increasing time

planet. For a small box ( $8 R_M$ ), the mass-loss rate peaks initially relative to the boxes of dimension  $12 R_M$  and  $24 R_M$ , but subsequently, all converge to a same steady value. This is because, for a bigger box, it takes a longer time for the lost planetary mass to reach the box faces, but as we approach a steady-state, the amount of the mass-loss rate becomes independent of the box size. They all take a similar duration ( $\sim 25$  mins.) to reach a steady-state value, closely matching the measured times required for this run to attain the steady-state configuration.

### 6.3 EFFECTS OF INTERPLANETARY MAGNETIC FIELD DIRECTION

We modeled two different cases in which the planet is magnetized, but the direction of IMF is either positive z-directed or negative z-directed. So it is customary to analyze and compare the effects of opposite IMF polarities. [Figure 25](#) shows the temporal evolution of localized total mass-loss rate from Southern hemisphere (SH) ([Figure 25a](#)) and Northern hemisphere (NH) ([Figure 25b](#)) for S-IMF and N-IMF cases. The same methodology described in the previous section is applied here, and the box size of  $8 R_M$  is considered here to determine the loss rate. The top panel regarding the mass-loss rate from SH is clearly showing higher atmospheric escape in the S-IMF study than N-IMF. However, the atmospheric erosion from NH (bottom panel) shows a bulge in the mass-loss in the N-IMF case. The bump arises in the transient state and remains above the plot for the S-IMF case, signifying more loss in the N-IMF case during this period (10-30 mins.). Nevertheless, both the curves converges to a constant value and we discovered the higher atmospheric escape is happening in  $(0,0,-1)$  IMF direction ([Figure 25a](#), [Figure 25b](#)). This is because magnetic reconnection is favored in southward-directed IMF, which ushers the erosion of mini-magnetopause as described in [Section 5.5](#). Due to the Marsward displacement of the protective plasma boundary, a larger

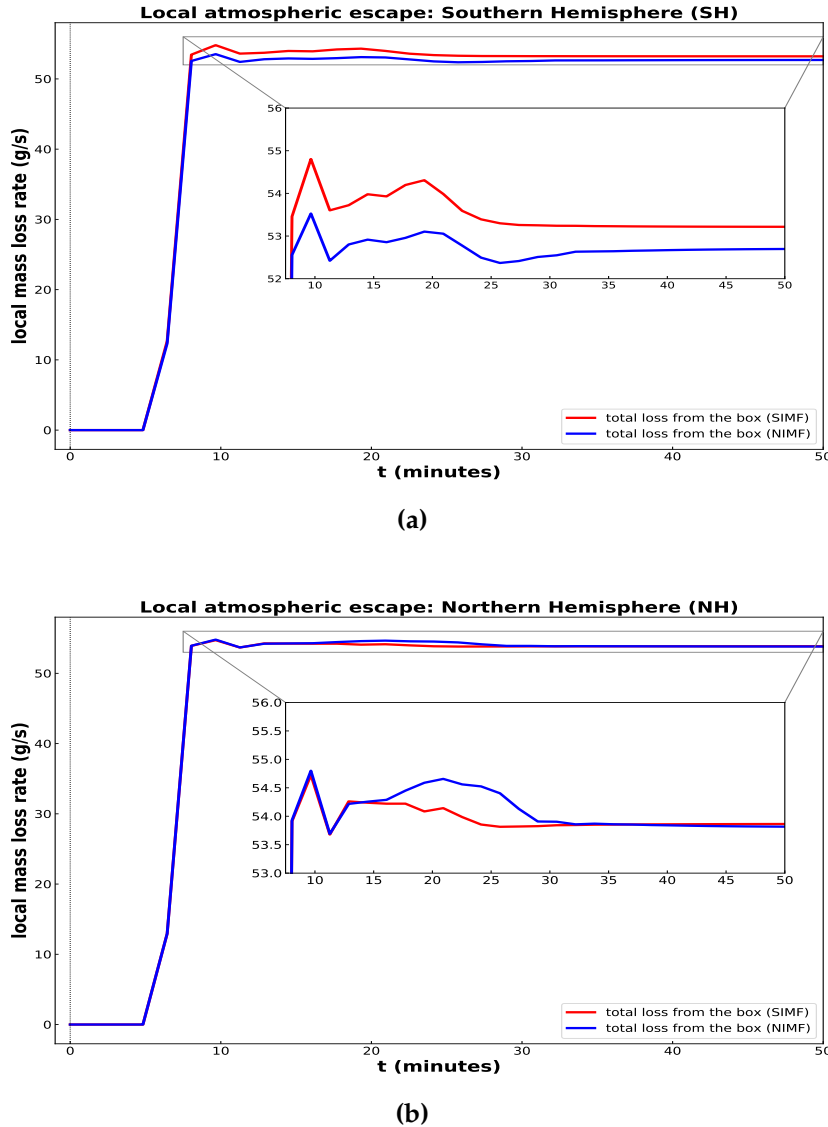


**Figure 25:** Local atmospheric mass loss rate from a) Southern hemisphere (SH) and b) Northern hemisphere (NH) for S-IMF and N-IMF cases. A cubic box with length extending from  $-4 R_M$  to  $+ 4 R_M$  in all three directions is considered for the mass-loss rate calculation. The box encompasses the planet and its atmosphere.

amount of planetary ions find themselves along IMF on which they flow from the dayside to the terminator region and finally get lost in deep space by trailing over the magnetotail. Thus, this shows that magnetic reconnection favors the atmospheric escape by increasing the size of the obstacle and providing necessary escape energy and momentum to planetary ions.

#### 6.4 IMPACTS OF MINI-MAGNETOSPHERE

We finally arrived at the point where we can detect whether the planetary magnetic field is protecting the atmosphere or escalating it by magnetic reconnection. For that, we need to compare the atmospheric escape in no dipole case from the

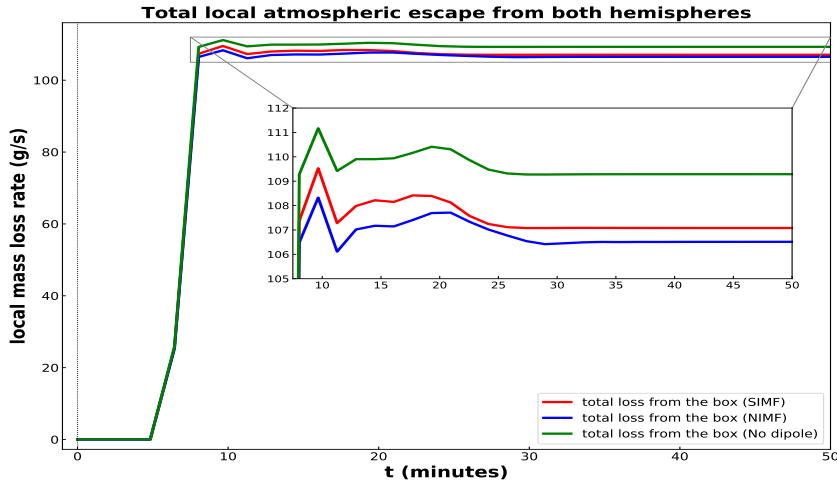


**Figure 26:** Temporal evolution of total localized atmospheric mass loss rate from S-IMF (red), N-IMF (blue) and ND (green). A cubic box with length extending from  $-4 R_M$  to  $+4 R_M$  in all three directions is considered for the mass-loss rate calculation. The box encompasses the planet and its atmosphere.

other two cases. Figure 25 exactly describes the requirement. It shows the temporal evolution of local mass-loss rate for all the three cases (S-IMF, N-IMF and ND). The transient state for ND case is similar to the other two cases. However, a higher amount of atmospheric erosion is discovered when no intrinsic magnetic field is present. Furthermore, in steady-state configuration, the mass-loss rate from ND is about 2% and 3% higher than S-IMF and N-IMF studies. The Figure 26 demonstrates clearly that higher trans-terminator outflow is happening in the absence of the planetary magnetic field. Thus, we can affirmatively conclude that presence of mini-magnetosphere shields the atmosphere of the planet.

The above results qualitatively match with Li et al. (2020) who simulated a multi-fluid MHD model and concluded that ion escape is suppressed in the transition between the sun-mars line and terminator under the impact of a localized dipolar magnetic field. Ma et al. (2002), who concluded that the presence of a crustal magnetic field decreases the escape flux by forming the mini-magnetocylinders in regions of strong magnetic strength is discerned in our simulations. Hara and Lundin et al. (2011) also reached to a similar conclusion however, they presented different reduction rates. An important point to keep in mind here is that we only observed the atmospheric escape from trans-terminator flow and ion outflow mechanism. It might be possible that other escape mechanisms like plume outflow or bulk ion escape exceeds and might produce a different result from ours. For instance, Brain et al. (2010) estimated that the loss from Bulk ion escape can be comparable to the long term ion escape rate and they concluded that this loss could go as high as 5-10 % of total ion loss. Thus, rephrasing our statement, we showed that a strong, localized magnetic anomaly in the planetary crust would protect the atmosphere of the planet from ion outflow and trans-terminator escape processes.

# 7

## CONCLUSION

---

We began with an introductory statement describing how strong, global, dynamo generated magnetic field of Earth is one of the key reasons for our survival. In support, we presented several empirical evidence on why we think of it as an impenetrable shield. However, with the emerging technology, some new observations have been made, which are suggesting otherwise. Several studies have cast pressing doubts on the conventional idea and, perhaps, to a degree, where the absolute requirement of an intrinsic magnetic field in the context of a planet's habitability is in question? Thus, being moved by the question, we modeled and studied the interactions between a Sun-like star and a Mars-like planet. The red planet, having an inhomogeneous, strong, localized crustal magnetic field combined with a thin atmosphere and weak gravity, makes it a perfect natural laboratory to study those interactions. Furthermore, these concentrated magnetic anomalies are practically extending to only a few places on the planet, thus, making Mars a weakly magnetized planet, appropriately suitable to understand the underlying physics of planetary magnetic field in Star-Planet Interactions ([SPI](#)).

In our attempt to address the big picture, we presented a set of questions before the reader in the [Section 2.3](#). To a fair extent, we have explored the first three questions thoroughly. In doing so, we used the freely available 3D magnetohydrodynamic code PLUTO where we cast the star-planet system. The planet's density and atmosphere were derived using a continuous 1D radial function, and a mini-magnetosphere is implanted in the southern hemisphere to mimic the strong crustal field observed on Mars. We exploited the ideal dipolar field equations to model our mini-magnetosphere, where a dimensionless factor 'f' is emerged to represent magnetic strength at the surface equivalent of dipole's location. Below provided are the answers to those questions:

- **How does a planet having a small-scale spatially located magnetic field interacts with the magnetized stellar wind?**

This question was, in general, is to check the robustness of the model. We observed some certain MHD structures like Bow Shock ([BS](#)), Magnetic Pile-up Region ([MPR](#)), magnetotail, plasma sheet and neutral sheet. The exciting result is the presence of mini-magnetocylinders at the strong magnetic field location which was also detected in [MGS](#) data [[Ma et al. \(2002\)](#)]. Overall, the interactions are between the Sun-Earth and Sun-Venus system, where the higher overlap is with planet Venus. This is because of the small-scale of mini-magnetosphere, which undoubtedly promoted the interactions between the solar wind and the planet's atmosphere.

- **What differences arise in the magnetic topology due to the strong magnetic anomalies?**

The presence of the mini-magnetosphere gave rise to a hybrid magnetic topology where all fundamental magnetic configurations are recognized in the simulations. The open field lines were detected in both the dayside and nightside of the planet due to magnetic reconnection. Draped field lines are perceived wrapping around Mars, where closed field lines are only discovered in the vicinity of the dipole. This is again because of the small-scale size of the mini-magnetosphere. Apart from magnetic topology, we found the decreased (and increased) magnitude of magnetic deviation pressure in the nightside (and dayside) of the magnetosphere when the planet is blessed with the intrinsic magnetic field. This happens because reconnection releases a stored amount of magnetic energy and, therefore, decreases the magnetic pressure on the nightside. One of the significant consequences of this phenomenon is the lower trapping of solar wind ions in the planet's wake compared to when no intrinsic magnetic is present. Since current density is obtained from the gradient of magnetic field deviation, we observed a similar trait in it, where we found the lower diamagnetic current (plasma & neutral sheet) in the mini-magnetosphere case than no dipole study. Excitingly, we found that the magnetic anomaly is decelerating the magnetized gas in the downstream regime by channelizing the flow from southern to northern hemisphere. This effect is directly correlated with ion outflow and is also appreciated in the analysis of atmospheric erosion. Lastly, from the polar analysis of magnetic field deviation components, we established that the signatures of magnetic reconnection are extrapolated to the planetary surface, specifically around the location where the crustal magnetic field is buried.

- **Does the presence of this intrinsic magnetic field affects the plasma boundaries like BS and MPB? and if yes, then how?**

If we would like to answer this question in one line, then it would be Yes and No. Within the framework of our model, we observed some dissimilarities in the Bow Shock ([BS](#)) structure when the intrinsic magnetic field is present. The [BS](#) is located at higher altitudes in the southern hemisphere, where we placed the mini-magnetosphere. This might be due to the extra magnetic pressure from the spatial located magnetic field. However, the extension was smaller than the allowed precision, and hence, we can cautiously say that no major distortions are discovered in the [BS](#) structure. In respect of Magnetic Pileup Boundary ([MPB](#)), we do not find any solid, permanent thin plasma boundary in our simulation. However, we found a subsolar location of a region having similar signatures of [MPB](#). It is estimated to be at a distance of  $1.075 R_M$  from the origin. Our simulation is a perfect example to understand the effects of the planet's atmosphere. In the presence of strong magnetic bubbles, we observed the formation of mini-magnetopause located in the neighborhood of planetary dipole. This pressure balance boundary is estimated to be positioned at  $1.09 R_M$  and  $1.1 R_M$  in [S-IMF](#) and [N-IMF](#) studies. Thus, [MPB](#) is certainly pushed outward in the southern hemisphere due to a strong crustal field. Apart from these

effects, we discover the case of magnetopause erosion in our simulation, which is common in magnetized planets like Earth.

- **What are the impacts of a mini-magnetosphere on the "local" atmospheric escape?**

In order to address this question, we divide our analysis into three parts. First, where we consider the case of only southward directed Interplanetary Magnetic Field ([IMF](#)) and compare the local mass-loss rate from the northern and southern hemispheres. Within this framework, we found approximately a 0.5% higher mass-loss rate in the Northern hemisphere than the southern hemisphere. This implies that the mini-magnetosphere is protecting the planet's environment by trapping and channelizing the planetary ions and solar wind plasma. In the second part, we studied the effects of [IMF](#) polarity. We compared the local mass-loss rate for [S-IMF](#) and [N-IMF](#) study, and because of magnetic reconnections, the higher mass-loss rate from both hemispheres is estimated in Southward-Interplanetary Magnetic Field ([S-IMF](#)). Now, to finally answer the above question, we did our last analysis. We calculated the sum of the local mass-loss rate of both hemispheres and compared the temporal evolution of the said mass-loss rate for all three cases i.e., [S-IMF](#), [acsN-IMF](#), and No dipole ([ND](#)). The mass-loss rate in [ND](#) study is determined to be 2% and 3% higher than [S-IMF](#) and [N-IMF](#) cases. This indicates clearly that the mini-magnetosphere prevents the atmosphere of the planet and, therefore, is crucial for the habitability of a planet.

To sum up, we think that our study has made an important stride in studying how the presence of small-scale spatially located intrinsic magnetic field affects the interaction of the planet's atmosphere with the solar wind. From the quantitative and qualitative results of our study we have drawn vital inferences about the impacts it might have on the potential habitability of a planet.

We believe that a new avenue of exciting problems can now be studied using the results of our study and the star-planet interaction module that we have introduced into PLUTO. Advancements in this study surely hold promising results not only in studying star-planet interactions but also in the field of planetary habitability.



# A

## DENSITY AND PRESSURE OF ATMOSPHERE

---

We used the same numerical scheme developed by [Das et al. \(2019\)](#) to determine the density and pressure profile for our modeled planet. Within the planetary volume, we maintained a constant density profile ( $\rho_{pl}$ ), which is 20 times the ambient medium density ( $\rho_{amb}$ ):

$$\rho_{pl}(r) = 20\rho_{amb} \text{ for } r \leq r_{pl}, \quad (17)$$

where  $r_{pl}$  is the radius of planet (3389.5 km). Beyond the planetary surface, we extends the atmosphere up to  $r = 3r_{pl}$ . Between these two regions, the density profile is governed by a hyperbolic tan function:

$$\rho_{atm}(r) = \rho_{pl} + \frac{(\rho_{amb} - \rho_{pl})}{2} [\tanh\theta(r/r_{pl} - 2) + 1] \text{ for } r_{pl} \leq r \leq 3r_{pl}, \quad (18)$$

where  $\rho_{pl}$  and  $\rho_{amb}$  are the densities of planet and the ambient medium. The hyperbolic tangent function is chosen to ensure a smooth transition between the density values at the boundaries  $r_{pl} \leq r \leq 3r_{pl}$ . The graphical representation of above mathematical equations is showed in [Figure 8](#) (left).

To have a gravitational stratified atmosphere, the gradient of atmospheric pressure must be equal to the atmospheric density times the gravitational field of planet. We considered the newtonian potential for our study as the whole system is non-relativistic. The gravitational field is set up in whole computational domain and is produced by the virtue of total mass of the planet ( $M_{Mars}$ ) which is assumed to be a point mass kept at the center of the planet (at origin). below equation describes the mathematical expression of considered gravitational field:

$$g(r) = -\frac{GM_{pl}}{r^2}, \text{ for } r > 0 \quad (19)$$

where  $G$  is gravitational constant and  $M_{pl}$  is equal to mass of red planet. To achieve hydrostatic equilibrium, the pressure distribution in the atmosphere is found by numerical integration of below-mentioned equation:

$$\frac{dP}{dr} = -\rho_{atm}(r)g(r) \text{ for } r_{pl} \leq r \leq 3r_{pl}, \quad (20)$$

where  $\rho_{atm}$  is given by [Equation 18](#). The pressure inside the planet is evaluated by extrapolating the value of pressure at the planet-atmosphere boundary as found from the numerical integration. The mathematical expression for the said statement is:

$$P(r) = P(r_{pl}) - \left[ \frac{dP}{dr} \right]_{r=r_{pl}} (r_{pl} - r) \text{ for } r \leq r_{pl}, \quad (21)$$

The pressure in the ambient medium is determined by considering the adiabatic process for an ideal gas:

$$P(r) = \frac{\rho_{amb} c_s^2}{\gamma} \text{ for } r \geq 3r_{pl}, \quad (22)$$

where  $c_s$  is the speed of sound given by [Equation 14](#) and  $\gamma$  is the polytropic index. The overall pressure profile is described in [Figure 8](#) (right).

# B

## MAGNETIC DIPOLE FIELD EQUATIONS

---

The primary purpose of this chapter is to explain the emergence of factor 'f' in [Equation 5 - Equation 7](#). In this context, we first consider a magnetic dipole placed at origin. The major results are taken from [Jackson \(1998\)](#) and a reader is requested to go through the book for the detailed physical explanations.

The vector potential of a point dipole having a magnetic moment of 'm' at a distance of 'r' can be expressed as:

$$\mathbf{A}(\mathbf{r}) = \frac{\mu_0}{4\pi} \left( \frac{\mathbf{m} \times \mathbf{r}}{|\mathbf{r}|^3} \right) \quad (23)$$

where  $\mu_0$  is magnetic permeability of free space and the bold font represent vector notation. The magnetic induction (field) is derived by taking the curl of above equation and is given by

$$\mathbf{B}(\mathbf{r}) = \frac{\mu_0}{4\pi|\mathbf{r}|^3} (3(\mathbf{m} \cdot \mathbf{r})\hat{r} - \mathbf{m}) \quad (24)$$

where in derivation we neglected the higher order terms. The above equation works only outside the current distribution. Now, let's assume that magnetic moment is oriented in z-direction i.e..  $\mathbf{m} = |m|\hat{z}$ . From here, we can represent the magnetic dipole field in spherical coordinates  $(r,\theta,\phi)$  by taking the dot product of [Equation 24](#) with independent basis of spherical geometry,

$$\begin{aligned} (3(\mathbf{m} \cdot \mathbf{r})\hat{r} - \mathbf{m}) \cdot \hat{r} &= 2|m|\cos\theta \\ (3(\mathbf{m} \cdot \mathbf{r})\hat{r} - \mathbf{m}) \cdot \hat{\theta} &= |m|\sin\theta \\ (3(\mathbf{m} \cdot \mathbf{r})\hat{r} - \mathbf{m}) \cdot \hat{\phi} &= 0 \end{aligned} \quad (25)$$

where  $\theta$  is known as colatitude. From above results, magnetic field components in  $(r,\theta,\phi)$  plane are:

$$\begin{aligned} \mathbf{B}_r(\theta, r) &= \frac{\mu_0}{4\pi|\mathbf{r}|^3} (2|m|\cos\theta) \hat{r} \\ \mathbf{B}_\theta(\theta, r) &= \frac{\mu_0}{4\pi|\mathbf{r}|^3} (|m|\sin\theta) \hat{\theta} \\ \mathbf{B}_\phi(\theta, r) &= 0. \end{aligned} \quad (26)$$

Now, consider that we don't know the magnetic moment of dipole but, we know how much magnetic strength it is producing at a point which makes an angle of  $\theta_L$  with equatorial line. [Figure 27](#) describes the picture where magnetic dipole moment ( $\mathbf{m}$ ) is in z-direction. We only know the magnetic intensity produce by this dipole at an angular location of  $\theta_L$  as denoted by  $B_0$  in the given figure.

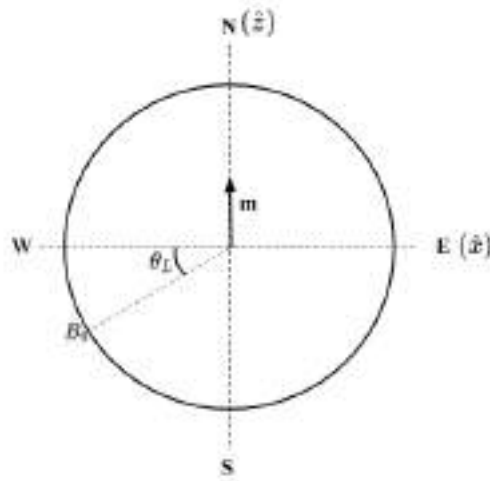


**Figure 27:** A qualitative sketch of magnetic dipole ('m') placed at origin and producing magnetic strength of value  $B_0$  at an angular location of value  $\theta_L$ . The schematics are in  $r\text{-}\theta$  plane. N,E,W and S are abbreviations of North, East, West and South.

Now our strategy from here will be to calculate the magnetic strength at said location and equate it with known magnetic strength ( $B_0$ ). The angle which the known magnetic location makes with the z-axis is  $\theta = 90^\circ + \theta_L$ . However, a symmetry exists about the equator line, and therefore we can write  $\theta = 90^\circ - |\theta_L|$ . Putting the value of  $\theta$  in [Equation 26](#) and calculating the magnitude of magnetic field,

$$|B(\theta_L)| = \frac{\mu_0|m|}{4\pi|R_{pl}|^3} \left( \sqrt{4\cos(90^\circ - |\theta_L|)^2 + \sin(90^\circ - |\theta_L|)^2} \right) \quad (27)$$

where  $R_{pl}$  is the radius of planet and we used the simple vector law i.e.  $|\mathbf{B}(\mathbf{r})| = (B_r^2 + B_\theta^2 + B_\phi^2)^{1/2}$  to determine the magnitude. Taking the result of above equation and equating it with  $B_0$  gives us,

$$\frac{\mu_0|m|}{4\pi} = B_0|R_{pl}|^3 \cdot \frac{1}{\left( \sqrt{4\cos(90^\circ - |\theta_L|)^2 + \sin(90^\circ - |\theta_L|)^2} \right)} \quad (28)$$

where we replaced  $|B(\theta_L)|$  with  $B_0$ . The consequences of above equation is that, first, we can now replace the unknown magnetic moment with the R.H.S of above equation. Also, the dimensionless factor 'f' can be easily perceived as the term in denominator and is expressed below for the sake of completion.

$$f = \left( \sqrt{4\cos(90^\circ - |\theta_L|)^2 + \sin(90^\circ - |\theta_L|)^2} \right) \quad (29)$$

To determine the credibility of above equation let's perform a sanity check. Assume that the planet is our dear Earth and its equatorial surface magnetic field is given. This means that  $B_0 = 31000$  nT and  $\theta_L = 0$ . Putting these values in [Equation 30](#), we get,

$$\frac{\mu_0|m|}{4\pi} = 31000|R_E|^3 \quad (30)$$

which is the commonly used equation for planet Earth. To represent the magnetic field components  $(r, \theta, \phi)$  in known variables, we interchange terms in [Equation 30](#) and [Equation 26](#) and therefore, we get

$$\begin{aligned}\mathbf{B}_r(\theta, r) &= \frac{B_0|R_{pl}|^3}{f \cdot |r|^3} (2\cos\theta) \hat{r} \\ \mathbf{B}_\theta(\theta, r) &= \frac{B_0|R_{pl}|^3}{f \cdot |r|^3} (\sin\theta) \hat{\theta} \\ \mathbf{B}_\phi(\theta, r) &= 0.\end{aligned}\tag{31}$$

The above equations can be easily transformed in cartesian coordinates by representing the basis vectors of spherical geometry in the unit vectors of cartesian coordinates. We left this calculation for the reader and have provided the transformed result below:

$$\begin{aligned}\mathbf{B}_x(r) &= \frac{3B_0|R_{pl}|^3(xz)}{f \cdot |r|^5} \\ \mathbf{B}_y(r) &= \frac{3B_0|R_{pl}|^3(yz)}{f \cdot |r|^5} \\ \mathbf{B}_z(r) &= \frac{B_0|R_{pl}|^3(3z^2 - r^2)}{f \cdot |r|^5}\end{aligned}\tag{32}$$

In the context of our model, the dipole is placed at an arbitrary location,  $r_0 = (x_0, y_0, z_0)$  with a dipole tilt of  $\theta_{pl} = 53^\circ$ . Also, the position vector of dipole makes an angle of  $53^\circ$  ( $= \theta_L$ ) with the equatorial line. These characteristics have introduced some necessary changes in the above equation. First, the factor  $f$  takes account of the angular position of dipole. Secondly, we did the coordinate transformation to represent the above equation in the frame of magnetic dipole. This changed  $x, y, z$  and  $r \rightarrow (x-x_0), (y-y_0), (z-z_0)$  and  $(r-r_0)$ , where  $r_0$  is the euclidean distance of dipole from origin (= center of planet). Also, the  $R_{pl}$  got exchange with  $R_{pl} - r_0$  making the volume,  $V = (R_{pl} - r_0)^3$ . Now, the left characteristic called dipole tilt is introduced by rotating the magnetic field components about  $y$ -axis. This brings the terms like  $\cos\theta_{pl}$  and  $\sin\theta_{pl}$  in the respective magnetic field components. The final expression of the cartesian components is given in [Equation 5](#), [Equation 6](#) and [Equation 7](#)



# C

## RANKINE-HUGONIOT JUMP CONDITIONS

---

In order to capture the shock physics, we shall derive the MHD Rankine-Hugoniot relations and determine the conditions on plasma parameters required to sustain a shock. We primarily follow the Galtier (2016, Ch. 6); and *Introduction to Space Physics* (1995, Ch. 5) for the detailed instruction of this condition and its derivation. First, we shall change our frame of reference to shock frame, such that we can consider the shock as a stationary discontinuity. Our next step is to use the Gauss's law of magnetism ( $\nabla \cdot \mathbf{B} = 0$ ) along with the governing set of MHD equations whose mathematical representations are given in [Equation 1](#)-[Equation 4](#). Applying the Stokes theorem on induction equation ([Equation 4](#)) and Gauss divergence theorem on [Equation 1](#)-[Equation 3](#) combined with Gauss law of magnetism, we get,

$$\mathbf{t} \cdot [\mathbf{v} \times \mathbf{B}]_1^2 = 0 \quad (33)$$

$$\mathbf{n} \cdot [\rho \mathbf{v}]_1^2 = 0 \quad (34)$$

$$\mathbf{n} \cdot [\rho \mathbf{v} \mathbf{v}]_1^2 + \mathbf{n} \cdot \left[ p^2 + \frac{\mathbf{B}^2}{8\pi} \right]_1^2 - \frac{1}{4\pi} \mathbf{n} \cdot [\mathbf{B} \mathbf{B}]_1^2 = 0 \quad (35)$$

$$\mathbf{n} \cdot \left[ \left( \frac{\rho v^2}{2} + p + \frac{\mathbf{B}^2}{4\pi} + \rho e \right) \mathbf{v} - \frac{1}{4\pi} (\mathbf{v} \cdot \mathbf{B}) \mathbf{B} \right]_1^2 = 0 \quad (36)$$

$$\mathbf{n} \cdot [\mathbf{B}]_1^2 = 0 \quad (37)$$

In the above equations, notation  $[\Omega]_1^2$  represent the difference of the enclosed quantity in the sides 1 (upstream shock) and 2 (downstream shock). The  $\mathbf{n}$ · and  $\mathbf{t}$ · refers to the normal and tangential component of the enclosed difference and as these components are vanishing at shock boundary, we shall omit super- and sub-script. So,  $[\Omega]_1^2 \approx [\Omega]$  from here on. The above conditional expressions describes a general set of number of MHD discontinuities. The formation of a shock structure from these discontinuities depend on the the relation of plasma parameters in the downstream region with the upstream region. As we know that in Bow Shock (BS) plasma pressure and field change but static pressure remains constant. This implies a construction of tangential discontinuity which is satisfied by vanishing the normal component of magnetic field ([Equation 37](#)) across the shock boundary, i.e.

$$[\mathbf{B}]_n = 0 \quad (38)$$

Similarly, [Equation 34](#) describes the conservation of normal component of momentum:

$$[\rho v_n] = 0 \quad (39)$$

Using the above two constraints in [Equation 33](#), [Equation 35](#) and [Equation 36](#), we get

$$[B_n v_t] = [v_n B_t] \quad (40)$$

$$[\rho v_n^2] = - \left[ p + \frac{B^2}{8\pi} \right] \quad (41)$$

$$[\rho v_n v_t] = \frac{1}{4\pi} [B_n B_t] \quad (42)$$

These expressions along with above-mentioned two constraints are collectively called Rankine Hugoniot Jump conditions. To define the generalized law for all classes of discontinuities, we require to define following identities The average of a quantity (denoted by  $\mathcal{T}$ ) on both sides are:

$$\langle \mathcal{T} \rangle = \frac{1}{2} (\mathcal{T}_1 + \mathcal{T}_2) \quad (43)$$

The jump in the produce of same quantity is,

$$[\mathcal{T} \cdot \mathcal{T}] = [\mathcal{T}] \cdot \langle \mathcal{T} \rangle + \langle \mathcal{T} \rangle \cdot [\mathcal{T}] \quad (44)$$

Using the above identities and representing mass-flux as  $\mathcal{F}=\rho v_n$  and  $\rho = \frac{1}{\gamma}$ , we obtained the modified version of jump conditions:

$$\mathcal{F}[\mathcal{V}] - [v_n] = 0 \quad (45)$$

$$\mathcal{F}[\mathbf{v}] + \mathbf{n}[p] + \frac{1}{4\pi} \mathbf{n} (\langle \mathbf{B} \rangle \cdot [\mathbf{B}]) \frac{1}{4\pi} B_n [\mathbf{B}] = 0 \quad (46)$$

$$\mathcal{F} \langle \mathcal{V} \rangle [\mathbf{B}] + \langle \mathbf{B} \rangle [v_n] - B_n [\mathbf{v}] = 0 \quad (47)$$

$$[B_n] = 0 \quad (48)$$

$$\mathcal{F} \left( [e] + \langle P \rangle [\mathcal{V}] + \frac{1}{16\pi^2} [B_t^2 [\mathcal{V}]] \right) \quad (49)$$

Given the various class of discontinuities, we choose the zero mass-flux condition ( $\mathcal{F} \approx 0$ ) to satisfy mass conservation theorem. using this constraint and above modified form of Rankine Hugoniot conditions, we found the following set of equations:

$$\begin{aligned}[v_n] &= 0 \\ [v_t] &= 0 \\ [B_n] &= 0 \\ [B_t] &= 0 \\ [p] &= 0\end{aligned}\tag{50}$$

and from these equations, we reached to the continuity of total pressure:

$$[p + \frac{B^2}{8\pi}] = 0\tag{51}$$

In particular, for the purpose of our simulations, we make use of [Equation 50](#) to determine the relation of plasma parameters values in upstream and downstream regime of shock front.



# D

## CONSEQUENCES OF THIN ATMOSPHERE

---

The constituents of an atmosphere of a planet profoundly affect its interaction with the solar wind. The formation of MPB, BS, depends on whether the planet has a sufficient atmosphere to deflect or sometimes stagnate the magnetized gas. We observed in [Chapter 5](#) that no MPB forms because our hypothetical Mars-like planet has a thin atmosphere. Well, this is not the only consequence. The simulations show that our interactions are a hybrid mixture of Sun-Earth, Sun-Venus, and Sun-Moon system. We observed a formation of rarefaction region along with an area that shows signatures similar to of lunar wake.

Due to the thin atmosphere, solar wind speed does not reduce much in the post BS regime, which results in the neutralization of planetary plasma in the planet's dayside. This neutralization creates a plasma void in the magnetotail, and thus an expanding rarefaction region forms continuously refilling the plasma in void [[Fatemi et al. \(2013\)](#)]. Magnetic field lines start compressing in the wake until the magnetic pressure compensates for the lost plasma pressure. This is the physical phenomenon that we observed in [Figure 13b](#). The compression of the field lines produces a diamagnetic current sheet across the void boundary, as shown in [Figure 13f](#). However, [Fatemi et al. \(2013\)](#) suggested that when IMF is orthogonal to solar wind, more refilling of plasma occurs. As a result, less magnetic enhancement is found in the void region than when IMF is in the direction of wind flow.

This chapter's central motto is to prove the occurrence of lunar-like interactions by showing the signatures mentioned above. In particular, we follow the [Fatemi et al. \(2013\)](#) study, where they exhibit some particular traits in current and magnetic field magnitude in the regions of interest. Explicitly, the data represented by figure 2 holds more relevance to us. This is because it describes the case when the flow of wind is perpendicular to IMF direction, just like our case. We request our reader to read that article for a better understanding of the below-given plots.

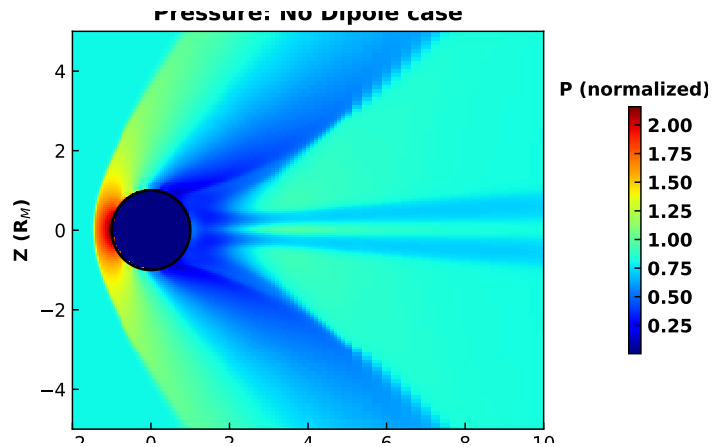


**Figure 28:** Pressure plot normalized to ambient pressure in noon-midnight plane. Two expanding blue regions describes the refraction regions.

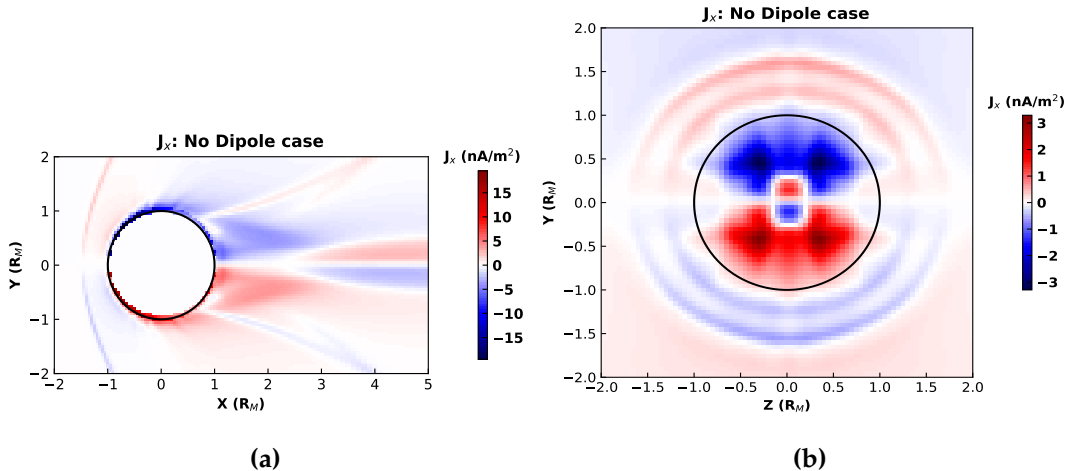


**Figure 29:** A pseudocolor plot of x-component of current density ( $J_x$ ) in a)equatorial plane (sliced at  $y = 0$ ) and b) dawn dusk plane (sliced at  $x = 3 R_M$ )

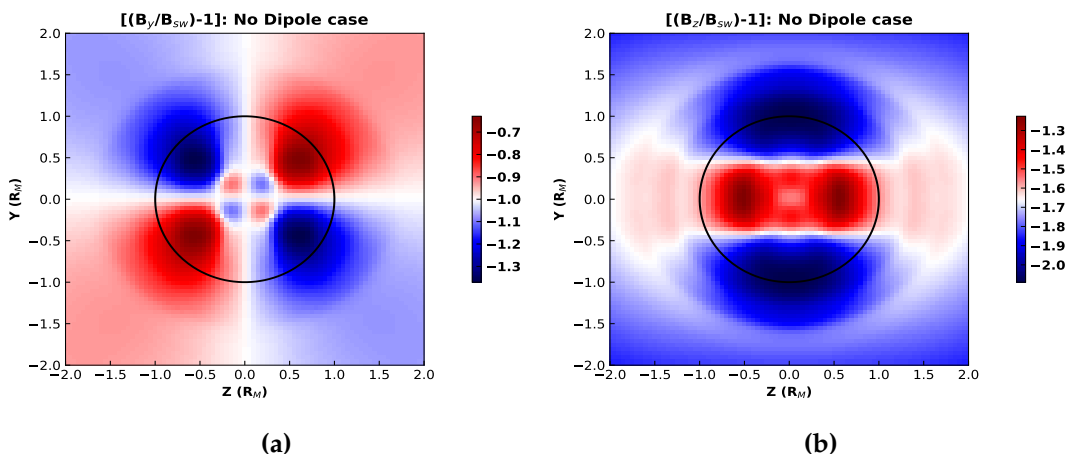


**Figure 30:** A pseudocolor plot of a)  $[(B_y/B_{sw}) - 1]$  and (b)  $[(B_z/B_{sw}) - 1]$  in dawn-dusk plane sliced at  $x = 3 R_M$ .

## REMAINING RESULTS OF NIMF STUDY

---

In this chapter, we have shown the remaining plots of Northward-Interplanetary Magnetic Field (N-IMF) study. Please refer to the captions and the earlier chapters to make sense of them.

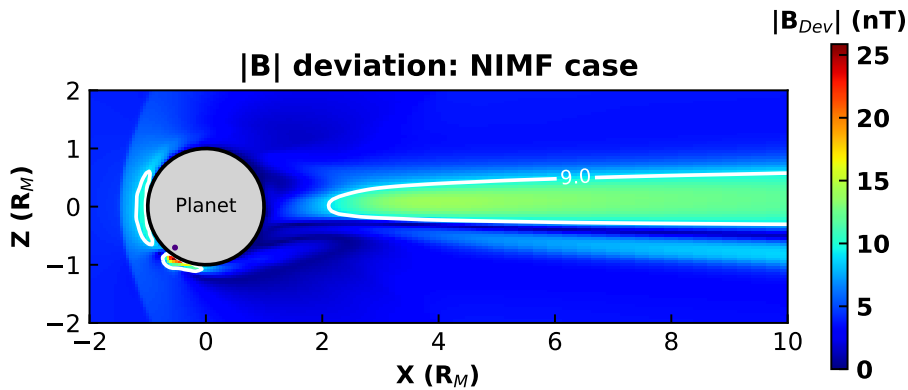


**Figure 31:** Pseudocolor plots of magnetic field deviation for N-IMF study in noon-midnight plane sliced at  $y = 0$ . The magenta dot represent dipole's location.

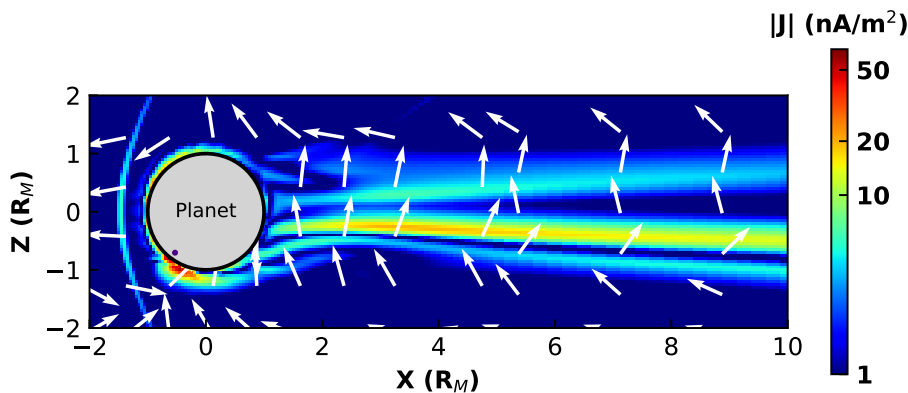


**Figure 32:** Pseudocolor plots of current density for N-IMF study in noon-midnight plane sliced at  $y = 0$ . The colorbar is in log scale and magenta dot represent dipole's location. The arrows are normalized and depicts the flow of current density vectors.

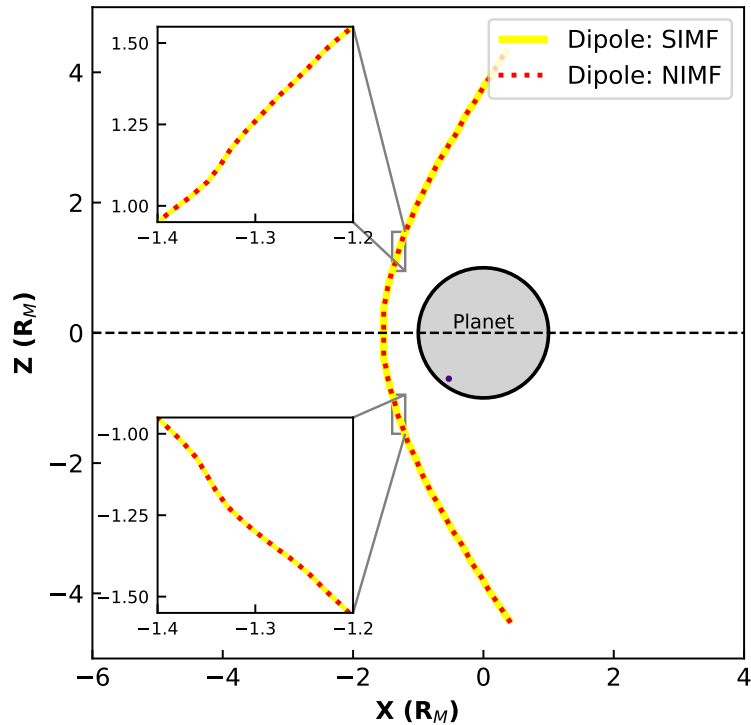


**Figure 33:** A contour line plot of BS structure for S-IMF (yellow) and N-IMF (dashed red) cases respectively. The analysis is done in noon-midnight plane, where two inset plots are giving a closer look in a part of Northern ( $Z > 0$ ) and Southern Hemisphere  $Z < 0$ .

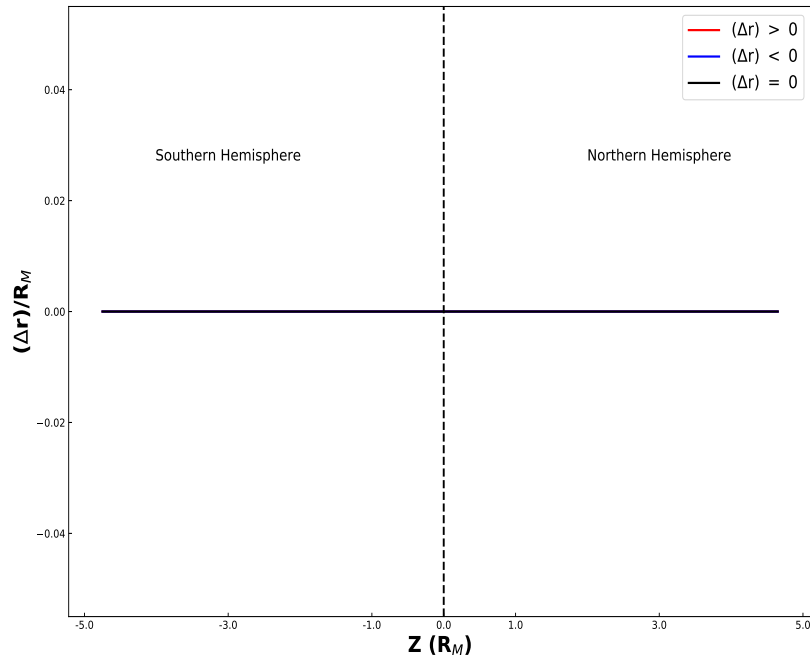


**Figure 34:** A graphical representation of variation of estimated  $\Delta r / R_M$  with  $Z$  plane.  $\Delta r$  for each  $z$  is equal to  $r_{S-IMF} - r_{N-IMF}$  at the respective  $z$  value. The red, black and blue colour steps signifies  $\Delta r >$ ,  $<$  and  $= 0$ .

## BIBLIOGRAPHY

---

- ALFVÉN, H. (1942). "Existence of Electromagnetic-Hydrodynamic Waves." In: *Nature* 150.3805, pp. 405–406. doi: [10.1038/150405d0](https://doi.org/10.1038/150405d0).
- Acuña, M. H. et al. (1998). "Magnetic Field and Plasma Observations at Mars: Initial Results of the Mars Global Surveyor Mission." In: *Science* 279.5357, pp. 1676–1680. doi: [10.1126/science.279.5357.1676](https://doi.org/10.1126/science.279.5357.1676).
- Acuña, M. H. et al. (1999). "Global Distribution of Crustal Magnetization Discovered by the Mars Global Surveyor MAG/ER Experiment." In: *Science* 284.5415, pp. 790–793. doi: [10.1126/science.284.5415.790](https://doi.org/10.1126/science.284.5415.790).
- Arkani-Hamed, Jafar (2001). "A 50-degree spherical harmonic model of the magnetic field of Mars." In: *Journal of Geophysical Research: Planets* 106.E10, pp. 23197–23208. doi: [10.1029/2000JE001365](https://doi.org/10.1029/2000JE001365).
- Barabash, Stas (May 2010). "Venus, Earth, Mars: Comparative Ion Escape Rates." In: *EGU General Assembly Conference Abstracts*. EGU General Assembly Conference Abstracts, p. 5308.
- Bertucci, C. et al. (Dec. 2011). "The Induced Magnetospheres of Mars, Venus, and Titan." In: 162.1-4, pp. 113–171. doi: [10.1007/s11214-011-9845-1](https://doi.org/10.1007/s11214-011-9845-1).
- Blackman, Eric G and John A Tarduno (Oct. 2018). "Mass, energy, and momentum capture from stellar winds by magnetized and unmagnetized planets: implications for atmospheric erosion and habitability." In: *Monthly Notices of the Royal Astronomical Society* 481.4, pp. 5146–5155. doi: [10.1093/mnras/sty2640](https://doi.org/10.1093/mnras/sty2640).
- Bößwetter, A. et al. (2004). "Plasma boundaries at Mars: a 3-D simulation study." In: *Annales Geophysicae* 22.12, pp. 4363–4379. doi: [10.5194/angeo-22-4363-2004](https://doi.org/10.5194/angeo-22-4363-2004).
- Brain, D. A. (2006). "Mars Global Surveyor Measurements of the Martian Solar Wind Interaction." In: *Space Science Reviews* 126.1, pp. 77–112. doi: [10.1007/s11214-006-9122-x](https://doi.org/10.1007/s11214-006-9122-x).
- Brain, D. A. et al. (2003). "Martian magnetic morphology: Contributions from the solar wind and crust." In: *Journal of Geophysical Research: Space Physics* 108.A12. doi: [10.1029/2002JA009482](https://doi.org/10.1029/2002JA009482).
- Brain, D. A. et al. (2007). "Electron pitch angle distributions as indicators of magnetic field topology near Mars." In: *Journal of Geophysical Research: Space Physics* 112.A9. doi: [10.1029/2007JA012435](https://doi.org/10.1029/2007JA012435).
- Brain, D. A. et al. (2010). "Episodic detachment of Martian crustal magnetic fields leading to bulk atmospheric plasma escape." In: *Geophysical Research Letters* 37.14. doi: [10.1029/2010GL043916](https://doi.org/10.1029/2010GL043916).
- Busse, FH (1978). "Magnetohydrodynamics of the Earth's dynamo." In: *Annual Review of Fluid Mechanics* 10.1, pp. 435–462.
- Choudhuri, Arnab Rai (1998). *The Physics of Fluids and Plasmas: An Introduction for Astrophysicists*. Cambridge University Press. doi: [10.1017/CBO9781139171069](https://doi.org/10.1017/CBO9781139171069).
- Connerney, J. E. P. et al. (1999). "Magnetic Lineations in the Ancient Crust of Mars." In: *Science* 284.5415, pp. 794–798. doi: [10.1126/science.284.5415.794](https://doi.org/10.1126/science.284.5415.794).

- Das, Srijan Bharati et al. (2019). "Modeling Star–Planet Interactions in Far-out Planetary and Exoplanetary Systems." In: *The Astrophysical Journal* 877.2, p. 80. doi: [10.3847/1538-4357/ab18ad](https://doi.org/10.3847/1538-4357/ab18ad).
- DiBraccio, Gina A. and Daniel J. Gershman (2019). "Voyager 2 constraints on plasmoid-based transport at Uranus." In: *Geophysical Research Letters* 46.19, pp. 10710–10718. doi: [10.1029/2019GL083909](https://doi.org/10.1029/2019GL083909).
- Dong, Chuanfei et al. (2015). "Multifluid MHD study of the solar wind interaction with Mars' upper atmosphere during the 2015 March 8th ICME event." In: *Geophysical Research Letters* 42.21, pp. 9103–9112. doi: [10.1002/2015GL065944](https://doi.org/10.1002/2015GL065944).
- Dong, Y. et al. (2017). "Seasonal variability of Martian ion escape through the plume and tail from MAVEN observations." In: *Journal of Geophysical Research: Space Physics* 122.4, pp. 4009–4022. doi: [10.1002/2016JA023517](https://doi.org/10.1002/2016JA023517).
- Dryer, Murray and Gary R. Heckman (1967). "Application of the hypersonic analog to the standing shock of Mars." In: *Solar Physics* 2.1, pp. 112–124. doi: [10.1007/BF00155897](https://doi.org/10.1007/BF00155897).
- Dungey, J. W. (1961). "Interplanetary Magnetic Field and the Auroral Zones." In: *Phys. Rev. Lett.* 6 (2), pp. 47–48. doi: [10.1103/PhysRevLett.6.47](https://doi.org/10.1103/PhysRevLett.6.47).
- Edberg, N. J. T. et al. (2008). "Statistical analysis of the location of the Martian magnetic pileup boundary and bow shock and the influence of crustal magnetic fields." In: *Journal of Geophysical Research: Space Physics* 113.A8. doi: [10.1029/2008JA013096](https://doi.org/10.1029/2008JA013096).
- Egan, Hilary et al. (July 2019). "Planetary magnetic field control of ion escape from weakly magnetized planets." In: *Monthly Notices of the Royal Astronomical Society* 488.2, pp. 2108–2120. doi: [10.1093/mnras/stz1819](https://doi.org/10.1093/mnras/stz1819).
- Fang, Xiaohua et al. (2017). "The Mars crustal magnetic field control of plasma boundary locations and atmospheric loss: MHD prediction and comparison with MAVEN." In: *Journal of Geophysical Research: Space Physics* 122.4, pp. 4117–4137. doi: [10.1002/2016JA023509](https://doi.org/10.1002/2016JA023509).
- Fatemi, S. et al. (2013). "The lunar wake current systems." In: *Geophysical Research Letters* 40.1, pp. 17–21. doi: [10.1029/2012GL054635](https://doi.org/10.1029/2012GL054635).
- Galtier, Sébastien (2016). *Introduction to Modern Magnetohydrodynamics*.
- Genestreti, Kevin et al. (May 2012). "The role and dynamics of oxygen of ionospheric origin in magnetopause reconnection." PhD thesis. doi: [10.13140/2.1.4788.2882](https://doi.org/10.13140/2.1.4788.2882).
- Giovanelli, R. G. (1946). "A Theory of Chromospheric Flares." In: *Nature* 158.4003, pp. 81–82. doi: [10.1038/158081a0](https://doi.org/10.1038/158081a0).
- Gold, T. (1959). "Motions in the magnetosphere of the Earth." In: *Journal of Geophysical Research (1896-1977)* 64.9, pp. 1219–1224. doi: [10.1029/JZ064i009p01219](https://doi.org/10.1029/JZ064i009p01219).
- Gronoff, Guillaume et al. (2020). *Atmospheric Escape Processes and Planetary Atmospheric Evolution*.
- Guedel, M. et al. (July 2014). "Astrophysical Conditions for Planetary Habitability." In: doi: [10.2458/azu\\_uapress\\_9780816531240-ch038](https://doi.org/10.2458/azu_uapress_9780816531240-ch038).
- Gunell, Herbert et al. (2018). "Why an intrinsic magnetic field does not protect a planet against atmospheric escape." In: *A&A* 614, p. L3. doi: [10.1051/0004-6361/201832934](https://doi.org/10.1051/0004-6361/201832934).

- Halekas, J. S. et al. (2015). "MAVEN observations of solar wind hydrogen deposition in the atmosphere of Mars." In: *Geophysical Research Letters* 42.21, pp. 8901–8909. doi: [10.1002/2015GL064693](https://doi.org/10.1002/2015GL064693).
- Halekas, J. S. et al. (2017). "Structure, dynamics, and seasonal variability of the Mars-solar wind interaction: MAVEN Solar Wind Ion Analyzer in-flight performance and science results." In: *Journal of Geophysical Research: Space Physics* 122.1, pp. 547–578. doi: [10.1002/2016JA023167](https://doi.org/10.1002/2016JA023167).
- Hara, Takuya et al. (2018). "Evidence for Crustal Magnetic Field Control of Ions Precipitating Into the Upper Atmosphere of Mars." In: *Journal of Geophysical Research: Space Physics* 123.10, pp. 8572–8586. doi: [10.1029/2017JA024798](https://doi.org/10.1029/2017JA024798).
- Harada, Y. et al. (2017). "Survey of magnetic reconnection signatures in the Martian magnetotail with MAVEN." In: *Journal of Geophysical Research: Space Physics* 122.5, pp. 5114–5131. doi: [10.1002/2017JA023952](https://doi.org/10.1002/2017JA023952).
- Harnett, E. M. and R. M. Winglee (2003). "The influence of a mini-magnetopause on the magnetic pileup boundary at Mars." In: *Geophysical Research Letters* 30.20. doi: [10.1029/2003GL017852](https://doi.org/10.1029/2003GL017852).
- Hood, L. L. and A. Zakharian (2001). "Mapping and modeling of magnetic anomalies in the northern polar region of Mars." In: *Journal of Geophysical Research: Planets* 106.E7, pp. 14601–14619. doi: [10.1029/2000JE001304](https://doi.org/10.1029/2000JE001304).
- Huang, Su-Shu (1960). "LIFE-SUPPORTING REGIONS IN THE VICINITY OF BINARY SYSTEMS." In: *Publications of the Astronomical Society of the Pacific* 72.425, pp. 106–114.
- Introduction to Space Physics* (1995). Cambridge University Press. doi: [10.1017/9781139878296](https://doi.org/10.1017/9781139878296).
- Jackson, John David (1998). *Classical Electrodynamics*. Wiley.
- Johnson Catherine L., Mittelholz Anna et al. (2020). "Crustal and time-varying magnetic fields at the InSight landing site on Mars." In: *Nature Geoscience* 13.3, pp. 199–204. doi: [10.1038/s41561-020-0537-x](https://doi.org/10.1038/s41561-020-0537-x).
- Langlais, Benoit et al. (2019). "A New Model of the Crustal Magnetic Field of Mars Using MGS and MAVEN." In: *Journal of Geophysical Research: Planets* 124.6, pp. 1542–1569. doi: [10.1029/2018JE005854](https://doi.org/10.1029/2018JE005854).
- Lazio, J. et al. (2018). *Magnetic Fields of Extrasolar Planets: Planetary Interiors and Habitability*.
- Li, ShiBang et al. (2020). "Effects of a dipole-like crustal field on solar wind interaction with Mars." In: *Earth and Planetary Physics* 4.1, pp. 23–31. doi: [10.26464/epp2020005](https://doi.org/10.26464/epp2020005).
- Lillis, R. J. et al. (2015). "Characterizing Atmospheric Escape from Mars Today and Through Time, with MAVEN." In: *Space Science Reviews* 195.1, pp. 357–422. doi: [10.1007/s11214-015-0165-8](https://doi.org/10.1007/s11214-015-0165-8).
- Lillis, Robert J. et al. (2013). "Time history of the Martian dynamo from crater magnetic field analysis." In: *Journal of Geophysical Research: Planets* 118.7, pp. 1488–1511. doi: [10.1002/jgre.20105](https://doi.org/10.1002/jgre.20105).
- Lue, Charles (2015). "Solar Wind Proton Interactions with Lunar Magnetic Anomalies and Regolith." PhD thesis. Umeå universitet.

- Lundin, R. et al. (2011). "On the relation between plasma escape and the Martian crustal magnetic field." In: *Geophysical Research Letters* 38.2. doi: [10.1029/2010GL046019](https://doi.org/10.1029/2010GL046019).
- Ma, Yingjuan et al. (2002). "Three-dimensional multispecies MHD studies of the solar wind interaction with Mars in the presence of crustal fields." In: *Journal of Geophysical Research: Space Physics* 107.A10, SMP 6–1–SMP 6–7. doi: [10.1029/2002JA009293](https://doi.org/10.1029/2002JA009293).
- Marquette, Melissa L. et al. (2018). "Autocorrelation Study of Solar Wind Plasma and IMF Properties as Measured by the MAVEN Spacecraft." In: *Journal of Geophysical Research: Space Physics* 123.4, pp. 2493–2512. doi: [10.1002/2018JA025209](https://doi.org/10.1002/2018JA025209).
- Matsunaga, Kazunari et al. (2017). "Statistical Study of Relations Between the Induced Magnetosphere, Ion Composition, and Pressure Balance Boundaries Around Mars Based On MAVEN Observations." In: *Journal of Geophysical Research: Space Physics* 122.9, pp. 9723–9737. doi: [10.1002/2017JA024217](https://doi.org/10.1002/2017JA024217).
- Meadows, Victoria S. and Rory K. Barnes (2018). "Factors Affecting Exoplanet Habitability." In: *Handbook of Exoplanets*. Ed. by Hans J. Deeg and Juan Antonio Belmonte. Cham: Springer International Publishing, pp. 1–24. doi: [10.1007/978-3-319-30648-3\\_57-1](https://doi.org/10.1007/978-3-319-30648-3_57-1).
- Meyer-Vernet, Nicole (1999). "How does the solar wind blow? A simple kinetic model." In: *European Journal of Physics* 20.3, pp. 167–176. doi: [10.1088/0143-0807/20/3/006](https://doi.org/10.1088/0143-0807/20/3/006).
- Mignone, A. et al. (May 2007). "PLUTO: A Numerical Code for Computational Astrophysics." In: 170.1, pp. 228–242. doi: [10.1086/513316](https://doi.org/10.1086/513316).
- Mitchell, D. L. et al. (2001). "Probing Mars' crustal magnetic field and ionosphere with the MGS Electron Reflectometer." In: *Journal of Geophysical Research: Planets* 106.E10, pp. 23419–23427. doi: [10.1029/2000JE001435](https://doi.org/10.1029/2000JE001435).
- Morschhauser, A. et al. (2014). "A spherical harmonic model of the lithospheric magnetic field of Mars." In: *Journal of Geophysical Research: Planets* 119.6, pp. 1162–1188. doi: [10.1002/2013JE004555](https://doi.org/10.1002/2013JE004555).
- Nagy, AF et al. (2004). "The plasma environment of Mars." In: *Space Science Reviews* 111.1-2, pp. 33–114.
- Obridko, V. N. and O. L. Vaisberg (2017). "On the history of the solar wind discovery." In: *Solar System Research* 51.2, pp. 165–169. doi: [10.1134/S0038094617020058](https://doi.org/10.1134/S0038094617020058).
- Ojha, Lujendra et al. (2015). "Spectral evidence for hydrated salts in recurring slope lineae on Mars." In: *Nature Geoscience* 8.11, pp. 829–832. doi: [10.1038/ngeo2546](https://doi.org/10.1038/ngeo2546).
- Parker, E. N. (1957). "Sweet's mechanism for merging magnetic fields in conducting fluids." In: *Journal of Geophysical Research (1896-1977)* 62.4, pp. 509–520. doi: [10.1029/JZ062i004p00509](https://doi.org/10.1029/JZ062i004p00509).
- Parker, E. N. (Nov. 1958). "Dynamics of the Interplanetary Gas and Magnetic Fields." In: 128, p. 664. doi: [10.1086/146579](https://doi.org/10.1086/146579).
- Parker, E. N. (1965). "Dynamical theory of the solar wind." In: *Space Science Reviews* 4.5, pp. 666–708. doi: [10.1007/BF00216273](https://doi.org/10.1007/BF00216273).
- Parker, Eugene N. (Sept. 1955). "Hydromagnetic Dynamo Models." In: 122, p. 293. doi: [10.1086/146087](https://doi.org/10.1086/146087).

- Petrinec, S. M. and C. T. Russell (1997). "HYDRODYNAMIC AND MHD EQUATIONS ACROSS THE BOW SHOCK AND ALONG THE SURFACES OF PLANETARY OBSTACLES." In: *Space Science Reviews* 79.3, pp. 757–791. DOI: [10.1023/A:1004938724300](https://doi.org/10.1023/A:1004938724300).
- Piqueux, Sylvain et al. (2019). "Widespread Shallow Water Ice on Mars at High Latitudes and Midlatitudes." In: *Geophysical Research Letters* 46.24, pp. 14290–14298. DOI: [10.1029/2019GL083947](https://doi.org/10.1029/2019GL083947).
- Pudovkin, M. I. et al. (1998). "Magnetopause stand-off distance in dependence on the magnetosheath and solar wind parameters." In: *Annales Geophysicae* 16.4, pp. 388–396. DOI: [10.1007/s00585-998-0388-z](https://doi.org/10.1007/s00585-998-0388-z).
- Rahmati, A. et al. (2017). "MAVEN measured oxygen and hydrogen pickup ions: Probing the Martian exosphere and neutral escape." In: *Journal of Geophysical Research: Space Physics* 122.3, pp. 3689–3706. DOI: [10.1002/2016JA023371](https://doi.org/10.1002/2016JA023371).
- Ramstad, Robin et al. (2016). "Effects of the crustal magnetic fields on the Martian atmospheric ion escape rate." In: *Geophysical Research Letters* 43.20, pp. 10,574–10,579. DOI: [10.1002/2016GL070135](https://doi.org/10.1002/2016GL070135).
- Riedler, W. et al. (1989). "Magnetic fields near Mars: first results." In: *Nature* 341.6243, pp. 604–607. DOI: [10.1038/341604a0](https://doi.org/10.1038/341604a0).
- Riedler, W. et al. (1991). "Interaction of the solar wind with the planet Mars: Phobos 2 magnetic field observations." In: *Planetary and Space Science* 39.1, pp. 75–81. DOI: [https://doi.org/10.1016/0032-0633\(91\)90129-X](https://doi.org/10.1016/0032-0633(91)90129-X).
- Russell, C. T. (1978). "The magnetic field of Mars: Mars 3 evidence reexamined." In: *Geophysical Research Letters* 5.1, pp. 81–84. DOI: [10.1029/GL005i001p00081](https://doi.org/10.1029/GL005i001p00081).
- Russell, C. T. (2000 A). "The solar wind interaction with the Earth's magnetosphere: a tutorial." In: *IEEE Transactions on Plasma Science* 28.6, pp. 1818–1830.
- Russell, C.T (2000 B). "The polar cusp." In: *Advances in Space Research* 25.7. Proceedings of the DO.1 Symposium of COSPAR Scientific Commission D, pp. 1413–1424. DOI: [https://doi.org/10.1016/S0273-1177\(99\)00653-5](https://doi.org/10.1016/S0273-1177(99)00653-5).
- Russell, Christopher T. (1974). "The Solar Wind and Magnetospheric Dynamics." In: *Correlated Interplanetary and Magnetospheric Observations*. Ed. by D. Edgar Page. Dordrecht: Springer Netherlands, pp. 3–47.
- Sakai, Shotaro et al. (2018). "Effects of a Weak Intrinsic Magnetic Field on Atmospheric Escape From Mars." In: *Geophysical Research Letters* 45.18, pp. 9336–9343. DOI: [10.1029/2018GL079972](https://doi.org/10.1029/2018GL079972).
- Sakata, R. et al. (2020). "Effects of an Intrinsic Magnetic Field on Ion Loss From Ancient Mars Based on Multispecies MHD Simulations." In: *Journal of Geophysical Research: Space Physics* 125.2. e2019JA026945 2019JA026945, e2019JA026945. DOI: [10.1029/2019JA026945](https://doi.org/10.1029/2019JA026945).
- Smith, Edward J. et al. (1965). "Magnetic Field Measurements near Mars." In: *Science* 149.3689, pp. 1241–1242. DOI: [10.1126/science.149.3689.1241](https://doi.org/10.1126/science.149.3689.1241).
- Strangeway, R. J. et al. (Dec. 2010). "Does a Planetary-Scale Magnetic Field Enhance or Inhibit Ionospheric Plasma Outflows?" In: *AGU Fall Meeting Abstracts*. Vol. 2010, SM33B–1893.
- (Dec. 2017). "Does an Intrinsic Magnetic Field Inhibit or Enhance Planetary Ionosphere Outflow and Loss?" In: *AGU Fall Meeting Abstracts*. Vol. 2017, P11B–2506.

- Trotignon, J.G. et al. (2006). "Martian shock and magnetic pile-up boundary positions and shapes determined from the Phobos 2 and Mars Global Surveyor data sets." In: *Planetary and Space Science* 54.4, pp. 357–369. doi: <https://doi.org/10.1016/j.pss.2006.01.003>.
- Vignes, D. et al. (2000). "The solar wind interaction with Mars: Locations and shapes of the bow shock and the magnetic pile-up boundary from the observations of the MAG/ER Experiment onboard Mars Global Surveyor." In: *Geophysical Research Letters* 27.1, pp. 49–52. doi: [10.1029/1999GL010703](https://doi.org/10.1029/1999GL010703).
- Vogel, Gretchen (1999). "Expanding the Habitable Zone." In: *Science* 286.5437, pp. 70–71. doi: [10.1126/science.286.5437.70](https://doi.org/10.1126/science.286.5437.70).
- Weber, Tristan et al. (2019). "The Influence of Solar Wind Pressure on Martian Crustal Magnetic Field Topology." In: *Geophysical Research Letters* 46.5, pp. 2347–2354. doi: [10.1029/2019GL081913](https://doi.org/10.1029/2019GL081913).
- Westall, Frances et al. (2015). "Biosignatures on Mars: What, Where, and How? Implications for the Search for Martian Life." In: *Astrobiology* 15.11. PMID: 26575218, pp. 998–1029. doi: [10.1089/ast.2015.1374](https://doi.org/10.1089/ast.2015.1374).
- Xu, Shaosui et al. (2020). "Characterizing Mars's Magnetotail Topology With Respect to the Upstream Interplanetary Magnetic Fields." In: *Journal of Geophysical Research: Space Physics* 125.3. e2019JA027755 10.1029/2019JA027755, e2019JA027755. doi: [10.1029/2019JA027755](https://doi.org/10.1029/2019JA027755).